

AD 740887

AFML-TR-71-69

①

STUDY OF DEFORMATION AND DEFECTS OCCURRENCE IN ADVANCED FORGING TECHNIQUE

SHIRO KOBAYASHI

S. SOHRABPOUR

M. M. SEIGAL

MECHANICAL DESIGN
UNIVERSITY OF CALIFORNIA
BERKELEY, CALIFORNIA

TECHNICAL REPORT AFML-TR-71-69

SEPTEMBER 1971

Reproduced by
NATIONAL TECHNICAL
INFORMATION SERVICE
Springfield, Va. 22151

Approved for public release, distribution unlimited.

AIR FORCE MATERIALS LABORATORY
AIR FORCE SYSTEMS COMMAND
WRIGHT-PATTERSON AIR FORCE BASE, OHIO

D D C
RECEIVED
MAY 1 1972
REGULATED
A

113

NOTICE

When Government drawings, specifications, or other data are used for any purpose other than in connection with a definitely related Government procurement operation, the United States Government thereby incurs no responsibility nor any obligation whatsoever; and the fact that the government may have formulated, furnished, or in any way supplied the said drawings, specifications, or other data, is not to be regarded by implication or otherwise as in any manner licensing the holder or any other person or corporation, or conveying any rights or permission to manufacture, use, or sell any patented invention that may in any way be related thereto.

CLASSIFICATION	
IC/ST	WHITE SECTION <input checked="" type="checkbox"/>
SEC	BUFF SECTION <input type="checkbox"/>
RESOURCES	<input type="checkbox"/>
CLASSIFICATION	<input type="checkbox"/>
ORIGINATOR/AVAILABILITY CODE	
LIST	AVAIL. CODE/IN. SPEC.
A	

Copies of this report should not be returned unless return is required by security considerations, contractual obligations, or notice on a specific document,

AIR FORCE: 2-11-71/700

Security Classification

DOCUMENT CONTROL DATA - R & D

(Security classification of title, body of abstract and indexing annotation must be entered when the overall report is classified)

1. ORIGINATING ACTIVITY (Corporate author) University of California Berkeley, California 94720		2a. REPORT SECURITY CLASSIFICATION Unclassified	
		2b. GROUP	
3. REPORT TITLE Study of Deformation and Defects Occurrence in Advanced Forging Technique			
4. DESCRIPTIVE NOTES (Type of report and inclusive dates) February 1970 - December 1970			
5. AUTHOR(S) (First name, middle initial, last name) Kobayashi, S.; Sohrabpour, S.; Sehgal, M. M.			
6. REPORT DATE April 1971		7a. TOTAL NO. OF PAGES	7b. NO. OF REFS
2a. CONTRACT OR GRANT NO F33615-70-C-1320 NEW		9a. ORIGINATOR'S REPORT NUMBER(S) None	
b. PROJECT NO		9b. OTHER REPORT NO(S) (Any other numbers that may be assigned this report) AFML - TR - 71 - 69	
c.			
d.			
10. DISTRIBUTION STATEMENT Approval for public release; distribution unlimited			
11. SUPPLEMENTARY NOTES		12. SPONSORING MILITARY ACTIVITY Air Force Materials Laboratory Wright-Patterson Air Force Base, Ohio 45433	
13. ABSTRACT A two-part investigation was performed to study the relationship between defects formation and deformation characteristics in plane-strain side-pressing and axisymmetric plastic indentation. In the first part, the investigation was undertaken to examine the detailed deformation characteristics involved in axisymmetric plastic indentation. Circular punches with flat and hemispherical ends were indented into specimens prepared from SAE 1215 steels under as-received and annealed conditions. In the second part, the detailed mechanics of the side-pressing of circular cylinders under plane-strain conditions were obtained, based on the observed flow patterns of commercially pure aluminum and copper specimens. Slip-line fields and corresponding hodographs were constructed, and stress calculations were made, taking into account the actual material properties.			

DD FORM 1473
1 NOV 55

Security Classification

Security Classification

14 KEY WORDS	LINK A		LINK B		LINK C	
	ROLE	WT	ROLE	WT	ROLE	WT
Plastic indentation						
Side-pressing of cylinders						
Slip-line method						
Work-hardening						

**STUDY OF DEFORMATION AND DEFECTS
OCCURRENCE IN ADVANCED FORGING TECHNIQUE**

SHIRO KOBAYASHI

S. SOHRABPOUR

M. M. SEHGAL

MECHANICAL DESIGN

UNIVERSITY OF CALIFORNIA

BERKELEY, CALIFORNIA

Approved for public release; distribution unlimited.


FOREWORD

This report was prepared by the University of California, Mechanical Design, Berkeley, California, under USAF Contract F33615-70-C-1320. The contract was initiated under Project No. 7351, "Metallic Materials," Task No. 731508, "Processing of Metals," and administered under the direction of the Air Force Materials Laboratory, Wright-Patterson Air Force Base, Ohio with Mr. Sidney O. Davis as Air Force Project Engineer.

This report, published in two parts, describes the results of research conducted during the period from February 1970 to December 1970. The manuscript was released by the authors in February 1971 for publication as a technical report.

The authors wish to thank Professor E. G. Thomsen, Department of Mechanical Engineering, University of California, Berkeley, for his supervision of the project from March to June 1971, and for his significant contributions to the results of this investigation.

This technical report has been reviewed and approved.


THOMAS D. COOPER
Chief, Processing and Nondestructive
Testing Branch
Metals and Ceramics Division
Air Force Materials Laboratory

ABSTRACT

The aim of the present investigation is to study the mechanics of plastic deformation and to find the relationship between defects formation and deformation characteristics in typical forging processes; namely plane-strain side-pressing and axisymmetric plastic indentation.

This report consists of two parts. In the first part, the investigation was undertaken to examine the detailed deformation characteristics involved in axisymmetric plastic indentation. Circular punches with flat and hemispherical ends were indented into specimens prepared from SAE 1215 steels under as-received and annealed conditions. The load-displacement curves were recorded, and measurements were made of the geometrical changes of the workpieces and of the strain distributions for various punch-workpiece dimensions. Furthermore, the mode of deformation was examined by revealing the flow lines, and fracturing of the workpiece was also observed.

In the second part, the detailed mechanics of the side-pressing of circular cylinders under plane-strain conditions were obtained, based on the observed flow patterns of commercially pure aluminum and copper specimens. Slip-line fields and corresponding hodographs were constructed, and stress calculations were made, taking into account the actual material properties. The effects on the deformation characteristics of friction at the interface, material properties, and initial geometry were examined in terms of flow lines and strain and strain-rate distributions.

TABLE OF CONTENTS

	<u>Page</u>
SECTION I. INVESTIGATION OF THE DEFORMATION CHARACTERISTICS OF AXISYMMETRIC PLASTIC INDENTATION	
1. INTRODUCTION	1
2. EXPERIMENTAL PROCEDURES AND MEASUREMENTS	3
3. RESULTS AND DISCUSSION	5
4. YIELD POINT LOAD AND LIMITING WORKPIECE DIMENSIONS	15
5. CONCLUSIONS	17
6. REFERENCES	18
SECTION II. DEVELOPMENT OF THE MECHANICS OF PLANE STRAIN SIDE-PRESSING OF CIRCULAR CYLINDERS	
1. INTRODUCTION	52
2. METHOD OF ANALYSIS	54
3. EXPERIMENTS AND CALCULATION PROCEDURES	58
4. DETAILED MECHANICS OF SIDE-PRESSING CIRCULAR CYLINDERS OF COPPER	61
5. EFFECTS OF SPECIMEN GEOMETRY AND MATERIAL PROPERTIES	67
6. SUMMARY	70
7. REFERENCES	72

LIST OF ILLUSTRATIONS

SECTION 1

<u>Figure</u>		<u>Page</u>
1	Stress-strain curves for SAE 1213 steels: as-received and annealed conditions	21
2	Experimental setup	22
3	Measurement of workpiece geometry	23
	Typical load-displacement curves for punches with flat and hemispherical ends. Conditions CD and CDS	24
5	Pressure-displacement curves for a flat punch of 0.41 in. diameter for various workpiece thicknesses	25
6	Effect of flat punch diameter on pressure- displacement curves for a workpiece of (a) 0.44 in. thickness	26
	(b) 0.875 in. thickness	27
7	Pressure-displacement curves for a hemispherical punch of 0.41 in. diameter for various workpiece thicknesses	28
8	Effect of hemispherical punch diameter on pressure-displacement curves for a workpiece of 0.875 in. thickness	29
9	Effect of workpiece thickness on the surface geometry for flat punch indentation. $D_o/d_o = 4.00$, and (a) $H_o/d_o = 0.487$ (BA); (b) $H_o/d_o = 1.00$ (BR)	30
	(c) $H_o/d_o = 2.00$ (BC); (d) $H_o/d_o = 4.00$ (BD)	31
10	Effect of flat punch diameter on the surface geometry for a workpiece of 0.44 in. thickness. (a) $D_o/d_o = 2.34$; (b) $D_o/d_o = 6.00$	32
11	Effect of flat punch diameter on the surface geometry for a workpiece of 0.875 in. thickness. (a) $D_o/d_o = 2.34$; (b) $D_o/d_o = 6.00$	33
12	Effect of workpiece thickness on the surface geometry for a hemispherical punch. (a) $H_o/d_o = 0.487$; (b) $H_o/d_o = 1.00$	34
	(c) $H_o/d_o = 2.00$	35
	(d) $H_o/d_o = 4.00$	36

<u>Figure</u>		<u>Page</u>
13	Effect of workpiece thickness on strain distributions for flat punches	37
14	Effect of flat punch diameter on strain distributions for $H_o/D_o = 0.250$	38
15	Effect of flat punch diameter on strain distributions for $H_o/D_o = 0.500$	39
16	Strain distributions for the punch with a hemispherical end	40
17	Load-displacement curves for a flat punch of $D_o/d_o = 4.00$	41
18	Load-displacement curves for a hemispherical punch of $D_o/d_o = 4.00$	42
19	Surface geometry in flat punch indentation for annealed steel. (a) $H_o/d_o = 1.00$. . .	43
	(b) $H_o/d_o = 2.00$; (c) $H_o/d_o = 4.00$. . .	44
20	Surface geometry in hemispherical punch indentation for annealed steel.	
	(a) $H_o/d_o = 1.00$	45
	(b) $H_o/d_o = 3.00$	46
	(c) $H_o/d_o = 4.00$	47
21	Flow lines for flat punch indentation	48
22	Flow lines for hemispherical punch indentation	49
23	Localized distortions along the punch surface	50
24	Types of cracks occurring in the indentation process	51

LIST OF ILLUSTRATIONS

SECTION II

<u>Figure</u>		<u>Page</u>
1	Stress-strain curves of aluminum 1100-F and commercially pure hard copper	74
2	Experimental setup for plane-strain side-pressing	75
3	Grid-distortions for the calculation of incremental strains	76
4	Grid patterns in side-pressing of circular cylinders of copper at various stages of deformation	77
5	Boundaries of the plastically deforming zone: copper specimen, smooth dies	78
6	Comparison of flow lines in pressing at reductions in height up to 40 percent with smooth and rough dies	79
7	Sliding displacement distributions at the die-workpiece interface for smooth and rough dies	80
8	Strain distributions along the x-axis at various reductions in height: smooth and rough dies	81
9	Strain distributions along the y-axis at various reductions in height: smooth and rough dies. . .	82
10	Constant effective strain contours for smooth (solid curves) and rough (dashed curves) dies at various reductions in height: (a) 10 percent, (b) 20 percent, (c) 30 percent, (d) 40 percent. .	83
11	Slip-line fields and corresponding hodographs for smooth dies at various reductions in height:	
	(a) 10 percent	84
	(b) 20 percent	85
	(c) 30 percent	86
	(d) 40 percent	87
12	Distributions of stress σ_x along the x-axis at various reductions in height	88

<u>Figure</u>		<u>Page</u>
13	Distributions of stress σ_y along the x-axis at various reductions in height	89
14	Distributions of stress σ_x along the y-axis and a comparison with those for rigid, perfectly plastic materials at various reductions in height	90
15	Distributions of stress σ_y along the y-axis and a comparison with those for rigid, perfectly plastic materials at various reductions in height	91
16	Constant stress σ_z contours at various reductions in height (unit: psi).	92
17	Contact pressure distributions along the die-workpiece interface	93
18	Variations of stress components at the center of the specimen as functions of the width-height ratio	94
19	Constant strain-rate contours at the width-height ratio $W/H = 1.22$ for specimens of various initial flats. (a) $2W_0 = 0.125$ in. ($2W = 0.852$ in.), (b) $2W_0 = 0.692$ in. ($2W = 0.828$ in.), (c) $2W_0 = 0.722$ in. ($2W = 0.788$ in.)	95
20	Constant strain-rate contours at the width-height ratio $W/H = 1.80$ for specimens of various initial flats. (a) $2W_0 = 0.125$ in. ($2W = 1.070$ in.), (b) $2W_0 = 0.692$ in. ($2W = 1.039$ in.), (c) $2W_0 = 0.722$ in. ($2W = 1.000$ in.)	96
21	Strain distributions along the x-axis at the same height-width ratios for three specimens of various initial flats	97
22	Strain distributions along the y-axis at the same height-width ratios for three specimens of various initial flats	98
23	Effective strain variations at the center of the specimens	99
24	Comparison of flow lines for aluminum and copper with smooth and rough dies (solid lines, copper; dashed lines, aluminum)	100
25	Effective strain variations at the center of the specimens of aluminum and copper ($2W_0 = 0.125$ in.)	101

SECTION I. INVESTIGATION OF THE DEFORMATION CHARACTERISTICS OF AXISYMMETRIC PLASTIC INDENTATION

by

M. M. Sehgal* and Shiro Kobayashi**

1. INTRODUCTION

The process of indentation has been the subject of research in metal deformation by many investigators for almost half a century. Using the slip-line method extensively for theoretical analyses, the investigators obtained solutions of the deformation mechanics occurring at the yield point for the plane-strain [1-4][†] and axisymmetric [5] flat punch indentations of rigid-plastic materials with no work-hardening. A number of publications can also be found in the literature on theoretical and experimental investigations of indentation by wedges, balls, and cones [6-14]. Since these investigations are concerned mainly with problems related to hardness testing, the vicinity of indenters is the principal area of interest. Problems of flat punch indentation into specimens of finite dimensions under plane-strain as well as axisymmetric conditions were treated by Lee and Kobayashi [15]. They obtained the detailed mechanics of indentation beyond the yield point, taking into account the actual material's property. However, the range of punch penetration considered in the investigation was such that the overall geometrical change of the

* Senior Engineering Aide, presently, Assistant Engineer,
Kaiser Engineers, Oakland, California.

**Professor of Mechanical Engineering.

† Numbers in brackets refer to references at the end of Part I.

workpiece was insignificant.

In recent years the process of indentation has attracted special attention as one of the basic operations involved in incremental forging. Incremental forging is the shaping of a workpiece by the repeated application of a punch whose contact area is considerably smaller than the projected area of the desired forging. The pattern of metal flow during the relatively deep penetration of the punch is a primary interest in incremental forging. For this range of indentation, the geometry of a workpiece of finite dimensions continuously changes, and the load-penetration relationships may depend on the specimen size and the pattern of metal flow. In this regard most of the previous investigations failed to provide direct information on metal flow during the forging operation, and only a few dealt with the problem of deep indentation.

Takahashi [16,17] investigated the deformation patterns in deep indentation by measuring the strain distributions along the workpiece surfaces with strain gages. Copper specimens having various values of work-hardening coefficients were indented by a flat cylindrical punch, and the dependency of the deformation patterns on the work-hardening coefficient of the workpiece material was observed. To test the validity of simulating the hot forging of aerospace materials, Abramowitz and Schey [18] examined the mode of deformation for plasticine, lead, and commercial aluminum during axial upsetting-piercing between punches with a workpiece overhang. The nature of deformation was characterized by various dimensions of deformed specimens, and the effects of workpiece geometry and punch radius on the deformation were evaluated quantitatively. Realizing that there was a dearth of

information on incremental forging, Male [19] attempted to determine basic information on the plastic indentation of metals with simple punches. His investigation was concerned with the effect of the major process variables on the punch pressure, and on shape control of workpiece during the indentation of circular blocks of aluminum. The principal variables for the study were the punch diameter-workpiece diameter ratio, the punch diameter-workpiece thickness ratio, the punch nose profile, and the lubrication.

The present investigation was undertaken to examine the detailed deformation characteristics involved in axisymmetric plastic indentation. Circular punches with flat and hemispherical ends were indented into specimens prepared from SAE 1215 steel under as-received and annealed conditions. The load-displacement curves were recorded, and the geometrical changes of the workpieces and the strain distributions were measured for various combinations of punch-workpiece dimensions. Furthermore, the mode of deformation was examined by revealing the flow lines, and fracturing of the workpiece was also observed.

2. EXPERIMENTAL PROCEDURES AND MEASUREMENTS

The experiments consisted of a series of tests involving the indentation of circular punches into a cylindrical workpiece of SAE 1215 steel. Solid cylindrical specimens were prepared with a diameter of 1.75 in. and with thicknesses of 0.214, 0.440, 0.875, and 1.75 in. The workpiece under the as-received condition was machined from 2-in.-diameter extruded bar stock. For the annealed condition the workpiece was machined to size and heated to 1600°F for 4 hours, followed by cooling in the furnace. The stress-strain curves for the steels under

the two conditions are given in Fig. 1. Circular punches with flat and hemispherical ends and flat dies were made from Graph-Mo and heat-treated to a hardness of Rockwell C 55. These punches and dies were then ground and lapped to a 7 ~ 10 μ in. surface finish. The diameters of the punches were 0.293, 0.440, and 0.750 in., and the flat punches each had a corner radius of 0.05 in. The values of the workpiece diameter-punch diameter ratio (D_o/d_o) and workpiece thickness-punch diameter ratio (H_o/d_o) are summarized in Table 1.

TABLE 1. PUNCH AND WORKPIECE DIMENSIONS AND THEIR RATIOS

Punch Diameter d_o , in.	Workpiece Thickness H_o , in.	A	B	C	D	
		H_o/D_o	0.122	0.250	0.500	1.00
	D_o/d_o	H_o/d_o				
A	0.75	2.34	0.285	0.587	1.17	2.34
B	0.440	4.00	0.487	1.00	2.00	4.00
C	0.293	6.00	0.730	1.50	3.00	6.00

D_o : workpiece diameter (= 1.75 in.)

d_o : punch diameter; H_o : workpiece thickness

Tests were conducted for all conditions of the workpieces made from as-received steel, but only punches of 0.440 in. diameter were used for tests on annealed steel specimens.

An apparatus consisting of a punch and die set, including a specimen-centering device, was constructed. With this apparatus,

shown in Fig. 2, indentation was performed by a 160,000 lb. Tinius Olson Testing Machine at the slow speed of 0.05 in/min. The workpiece, punch, and die were lubricated with Punch-Oil for all the tests. The displacement of the punch was measured by a deflectometer, and the load-displacement curves were obtained on a recorder attached to the testing machine. The specimens were indented to depths ranging from 0.15 in. to 0.25 in., and the surface geometry was measured at various stages of punch displacement. The strain distributions along the workpiece surfaces were computed from measurements of the distortion of grid patterns printed on the end surfaces of the specimens. The grid distortions were measured by a toolmaker's microscope, and the surface profile was determined by a dial indicator arrangement, shown in Fig. 3, to an accuracy of 0.001 in. The flow lines were revealed by etching at various configurations, and the location of the critical deformation for fracturing was determined from observations of crack formation. For identification of test conditions, the following symbols were used:

- AB - A indenter; B specimen; flat punch; as-received steel
- AB-A - A indenter; B specimen; flat punch; annealed steel
- ABS - A indenter; B specimen; hemispherical punch; as-received
- ABS-A - A indenter; B specimen; hemispherical punch; annealed

Symbols for the indenter and specimen are shown in Table 1.

3. RESULTS AND DISCUSSION

The results are presented first in detail with regard to the load-displacement relationships, the geometrical changes of the workpiece, and the strain distributions for a workpiece material of steel

under the as-received condition. Then the effect of the materials' properties on deformation characteristics is shown, by comparing as-received and annealed steels. Results of the studies of flow lines and crack formation are also given.

a. Load (Pressure)-Displacement Relationships: Typical load-displacement curves for the punches having flat and hemispherical ends are shown in Fig. 4. When an elastic-plastic material is continuously loaded from a stress-free state, the plastic and elastic components of distortion are at first comparable. As the loads are increased, the plastic zone expands to a size where large strains become possible, and the overall distortion increases at a rate controlled by the changing shape of the workpiece. The load-distortion curve changes its slope at the load under which large distortion begins. This point is described as the yield-point of the body. The bend of the curve is much more gradual for a punch with a hemispherical end than for a flat punch because of the continually increasing contact surface present in a hemispherical punch.

The relationships between the indentation pressure and punch displacement with a flat punch are shown in Fig. 5 for various workpiece thicknesses. The effect of the punch diameter on the pressure-displacement curve is given in Fig. 6. The punch pressures given in Figs. 5 and 6 were computed from the recorded loads based on the cross-sectional areas of the punch. As seen in Fig. 5, during the initial increase of punch pressure the curves for different workpiece thicknesses have more or less the same slope. For thinner specimens ($H_0/d_0 = 0.487$ and 1.00) the deformation extends throughout the direction of thickness at small punch displacements; this results in edge-

lifting and the pressure-displacement curves begin to deviate from each other. For thicker specimens ($H_0/d_0 = 2.00$ and 4.00), however, the deformation does not extend to the bottom surfaces of the workpiece, and the pressure-displacement curves are identical. The same observations were made for punches with diameters other than 0.440 in. With respect to the effect of the punch diameter on the pressure-displacement relationships shown for two workpiece thicknesses, it is observed that, regardless of the mode of deformation, the pressure is higher for punches having smaller diameters. Even the initial rate of pressure increase becomes dependent on the size of the punch when a workpiece is short and edge-lifting occurs (Fig. 6a). Within the range of investigation, no limiting value of the workpiece diameter-punch diameter ratio was found beyond which the effect of the punch diameter diminishes.

Although it is difficult to determine the yield-point load accurately for the scale of punch displacement used in the present study, the punch pressure at the yield point appears to be unchanged when the workpiece thickness is greater than twice the punch diameter and the ratio of the workpiece diameter and the punch diameter exceeds a value of 4. The yield-point pressure and the initial yield stress for as-received steel are approximately 210,000 psi and 68,000 psi, respectively, giving P/Y equal to 3.1. These results are in general, in agreement with Male's findings [19] for the plastic indentation of aluminum.

The pressure displacement relationships for punches with a hemispherical end are shown in Figs. 7 and 8. The exact contact area and

its variation during the penetration of the punch are not known. Therefore, the nominal punch pressure given in Figs. 7 and 8 was calculated based on the projected contact area, assuming that the depth of the contact surface is equal to the punch displacement. It is again seen in Fig. 7 that the effect of the workpiece thickness on the nominal punch pressure vanishes for thicknesses greater than twice the punch diameter. The effect of the punch diameter on the pressure-displacement curves is given in Fig. 8. A comparison of Fig. 8 with Fig. 6b shows that conclusions drawn for the flat punches are also applicable to punches with hemispherical ends. Also, the yield-point pressures for both types of punches are approximately of the same magnitude.

b. Change of Surface Geometry: The behavior of the load (pressure)-displacement curves for various workpiece dimensions and punch shapes is determined by the mode of deformation. Changes in the deformation mode after the yield point has been reached can be revealed to some extent by measuring the surface geometry of the workpiece at various stages of indentation. Figure 9 gives the results for workpieces of various thicknesses with a flat punch of $D_0/d_0 = 4.00$. The corresponding load-displacement curves are shown in Fig. 4. In shorter specimens (Fig. 9a, b), the plastic zone spreads throughout the direction of thickness first, and the workpiece edges are raised (edge-lifting) at an early stage of punch penetration. With increasing thickness of the workpiece, the degree of edge-lifting decreases (Fig. 9b). Relatively smooth top-free surfaces indicate that local large strains do not occur and the volume change due to punch penetration is accommodated by the bulk deformation of edge-lifting. When

the thickness of the workpiece further increases (Fig. 9c, d), large strains become possible locally, and a pile-up of the edge forms a so-called "coronet." As the punch penetrates, the distortion extends to the radial direction as well as to the direction of thickness.

The changes in workpiece geometry corresponding to the pressure-displacement relationships given in Figs. 6a, b are shown in Figs. 10 and 11, respectively. Figure 10 shows that edge-lifting occurs in a workpiece 0.440 in. thick, and the initial pile-up of the edge tends to take place as the value of H_0/d_0 increases (Fig. 10b). In a workpiece 0.875 in. thick, no coronet is formed when a punch of large diameter is used (Fig. 11a), but a pile-up of the material is observed with a punch of small diameter. A pile-up of the material near the punch edge was observed for conditions of $H_0/d_0 \geq 4.00$. It may be of interest to note that the range of the ratios for coronet formation coincides with the range where the yield-point pressure remains constant. In order for the initial mode of bulk deformation to take the form of edge-lifting, the workpiece thickness-workpiece diameter ratio (H_0/D_0) must be less than 0.5. For a workpiece of H_0/D_0 that is equal to or larger than 0.5, a different initial mode of bulk deformation occurs. When the punch penetration becomes sufficiently large, however, edge-lifting will eventually result. Figure 12 shows the changes in the surface geometry of the workpiece for punches having hemispherical ends. It is observed that a pile-up of the material due to a local large distortion occurred for all the conditions. The condition required for edge-lifting to appear as the initial mode of bulk deformation, however, was the same as that for flat punches, namely, $H_0/D_0 < 0.5$. A comparison of Fig. 12 with Fig. 9 shows the differences

in surface geometry for the flat punch and the hemispherical punch.

c. Strain Distributions: The strains (circumferential) were measured along the surface of the workpiece at various steps of punch penetration, and the strain distributions were obtained in relation to changes in the surface geometry of the workpiece. Figure 13 shows the effect of workpiece dimensions on the strain distributions corresponding to the surface geometry given in Fig. 9. For short specimens in which edge-lifting occurred, free surface strains are compressive and tend to increase toward the punch. As the penetration is increased, the strains along the free surface decrease further, and the strains along the punch-workpiece interface increase (Fig. 13a). When the thickness of the workpiece is increased, the strains along the free surface increase and then begin to become tensile, as seen in Fig. 13b. These variations of strain distribution reflect the bulk deformation of edge-lifting which occurred for these specimens. On the other hand, the trend is reversed for thicker specimens (Fig. 13c, d). Strains along the free surface are tensile, but they become compressive under the punch. Large strains near the edge of the punch are, of course, due to a local large deformation of the coronet type. The compressive strains under the punch, though small in magnitude, result from the flow pattern that causes the coronet formation.

While the material adjacent to the punch-workpiece interface undergoes a slight deformation, a severe deformation occurs at some distance beneath the contact surface. This mode of deformation continues as the punch penetrates, producing decreased strains at the interface, while strains along the free surface continue to increase. The strains along the lifted bottom surfaces are tensile, as expected,

and the distribution decreases toward the outer edge of the workpiece. The effect of the punch diameter on the strain distributions is given in Figs. 14 and 15 for two workpiece thicknesses. Figures 14 and 13b give the results for three punch diameters with workpiece thicknesses of $H_0/D_0 = 0.250$. The discussions regarding the mode of deformation given for Fig. 13 are also applicable to these results. In general, the strains are tensile, increase toward the punch, and become compressive along the punch-workpiece interface. The strains decrease with increased penetration of the punch. For a workpiece of $H_0/D_0 = 0.500$, however, Figs. 15 and 13c reveal that the strains increase with larger punch penetrations.

Examples of strain distributions for punches with hemispherical ends are shown in Fig. 16. The distributions shown in Fig. 16 can be compared with those for the flat punch in Fig. 13. The general shape of the distribution curve along the free surface is the same for both punches, but along the contact surface no compressive strains were found for spherical indenters. As the punch penetrates, the continued edge-lifting can be realized by the decrease in strain along the free surface, and the increased piling-up results in increased strain near the contact surface, as seen in Fig. 16a. Where no edge-lifting was observed, Fig. 16b, the strains increase over the entire surface, and no compressive strains were recorded again along the interface.

d. Effect of the Materials' Properties: With the use of identical punches and workpiece geometries, the load-displacement curves, surface geometries, and strain distributions were measured for indentations of annealed steel. The behavior of the annealed and as-received materials are compared. Figure 17 shows the effect of workpiece

dimensions on the load-displacement curve for annealed steel and compares the load-displacement relationship for the two states of the steel. For annealed materials, the indentation pressure is higher when the workpiece is thicker, but it becomes identical for specimens of $H_0/d_0 \geq 4.00$. This is true also for as-received steels. The load-displacement curves for the two states of material are also compared for $H_0/d_0 = 6.00$ in the figure. It may be of interest to observe that the load-displacement curves reflect exactly the characteristics of the stress-strain curves shown in Fig. 1: the variation of the indentation pressure for the annealed material is more rounded than that for as-received material, and the slope of initial pressure increase depends on the stress-strain property of the material.

Conclusions reached for the flat punch (Fig. 17) are also true for hemispherical punches regarding the load-displacement relationships, as shown in Fig. 18. It can also be seen in Fig. 18 that the load-displacement curves for the two states of materials converge when the deformation involved becomes large. Not only are the load-displacement relationships for the two materials different, but the flow behaviors differ also. Examples of the surface geometries for annealed steel are shown in Figs. 19 and 20 for flat and hemispherical punches, respectively. The test conditions for Fig. 19a, b, and c for annealed steel are the same as those for Fig. 9b, c, and d for as-received specimens. When edge-lifting occurs (Fig. 19a), the surface configurations do not differ qualitatively for the two states of materials. However, a difference in the deformation mode is evident when Fig. 19b and Fig. 9c are compared. For as-received material, it is clear that a piling-up occurs near the edge of the punch, but this

does not happen for annealed material. Furthermore, at the same degree of punch penetration, larger strains prevail throughout the annealed specimen, and the bulk deformation is such that edge-lifting occurs. Similar differences between annealed and as-received steels can be seen by comparing Fig. 19c and Fig. 9d.

In Fig. 20 it is interesting to observe the coronet formation at relatively large punch penetrations. It has not been determined conclusively whether the coronet is formed at the yield point of the body. However, from the observations reported in the literature, it appears that a "sinking-in" mode of deformation occurs at the yield point, and piling-up takes place after the yield point has been reached, when penetration of the punch continues. Nevertheless, a comparison of Fig. 20 with Fig. 12 shows that the piling-up is less pronounced and more rounded for annealed material than it is for as-received material.

e. Flow Lines and Fracturing: The 0.44 in. and 1.75 in. thick workpieces which were indented with punches having flat and hemispherical ends were sectioned along a meridian plane and then polished and etched to reveal the flow lines. Flow lines resulting from a flat punch indentation are shown in Fig. 21. When the flow lines for the two states of material are compared, it becomes clear that (1) severe distortions are present beneath the flat punch surface, (2) the distortion is more pronounced for a larger penetration of the punch, and (3) the degree of distortion is less for annealed material than for as-received material for the same punch displacement. Also evident are the "piling-up" and "sinking-in" characteristics of the deformation for the two materials.

This different behavior of cold-worked and annealed metals has been well explained by Hill [2]. He states that when the work-hardening is slight (cold-worked metals), a flow out to the surface with severe and localized distortion takes place before the elastic resistance of the bulk can be overcome: when the work-hardening is heavy the load which would be needed to effect a flow out to the surface is so great that an inward displacement accommodated by the resilience of the whole specimen occurs first.

A close examination of Fig. 21 reveals further that for as-received material a conical zone under the punch where the deformation is small remains approximately the same size, while for annealed material this zone becomes definitive only for a short specimen.

Figure 22 shows the flow lines resulting from the use of a hemispherical punch. Under the punch surface, more distortion can be observed for as-received steel than for annealed material, and the "piling-up" and "sinking-in" deformations for the two materials are again clearly shown. With the hemispherical punch, however, the formation of severe distortion is quite different from that for flat punch indentation, and there is a lesser degree of distortion for the hemispherical punch indentation. Details of the localized distortions along the flat punch and the hemispherical punch are given in Fig. 23.

Fracturing occurred both in the as-received material and the annealed material. No analytical study was possible regarding the effect of process variables on fracturing. The location of the critical state for fracturing, however, was found to be in the material around the edge of the punch where the distortions are expected to be largest. The types of cracks that occurred are shown in Fig. 24. As

far as the surface strains are concerned, they are smaller for annealed materials because of the mode of deformation, and their workability may well be influenced by the deformation characteristic in the process involved.

4. YIELD-POINT LOAD AND LIMITING WORKPIECE DIMENSIONS

In many problems the yield-point load is the quantity of greatest interest, and the main object of theoretical and experimental analyses has been to obtain this quantity. In the problem of indentation the yield-point load varies with the workpiece dimensions and becomes constant when the workpiece dimensions are large enough in comparison with the punch dimension. Another important problem is that of determining the limiting workpiece dimensions beyond which the yield-point load is constant and the workpiece can be considered as a semi-infinite body. Because of the general interest in these two problems, additional discussion concerning them is given here.

For the flat punch indentation of as-received SAE 1215 steel, it was found that the yield-point pressure remained unchanged for $H_0/d_0 \geq 2.00$ and $D_0/d_0 \geq 4.00$, and the yield-point value was given by $P/Y = 3.1$, where Y is the yield stress. For a punch having a hemispherical end, the same conclusion was found with regard to the values of the yield-point punch pressure and the limiting workpiece dimensions.

Shield [5] obtained an exact solution for axisymmetric indentation by a flat circular punch. Using the slip-line method based on the Tresca yield and potential functions, he found the value of the average pressure over the smooth punch to be $5.69k$ ($2.84Y$). Shield further

showed that the complete stress field can be obtained by extending the slip-line field into the rigid region within the specimen dimensions given by $H_o/d_o = 1.68$ and $D_o/d_o = 3.20$.

Levin [20] applied the upper-bound method to the indentation of a smooth, flat, rigid punch into a perfectly plastic material which obeys Tresca's yield criterion. He found that $5.84k$ ($2.92Y$) is an upper bound on the indentation pressure.

Chen [21] recently applied the bounding method to the problem of indentation on a block of finite dimensions. He obtained upper and lower bounds of the limiting punch pressure during indentation of a square punch on a square block and a circular punch on a circular cylinder for a rigid-plastic material which obeys the Tresca yield condition and the associated flow rule. Chen found that for a circular cylinder for which D_o/d_o is larger than 3.59 (rough punch) or 3.20 (smooth punch), the average indentation pressure becomes equal to that of a circular punch on the surface of a semi-infinite solid. The indentation pressure and the limiting workpiece dimensions found in the present experiment are in surprisingly good agreement with those obtained theoretically.

For a spherical indenter, Ishlinsky [22] has determined analytically the pressure between the indenter and the indentation at the yield point. Using the slip-line method based on the Harr-Karman hypothesis, he found the value of the pressure (load divided by the projected area of the indentation) to be $2.66Y$.

The specimens in the Brinell hardness test should be large enough to ensure that all the plastic flow occurs within a region considerably smaller than the specimen itself. Tabor [6] suggested as a working

standard the use of a specimen with a thickness at least 10 times the depth of the indentation for hard metals and at least 15 times the depth for softer metals. He also recommended that the specimen be about 4 times wider than the diameter of the impression. For a usual impression whose diameter is approximately half that of the indenter, the limiting workpiece dimensions become $H_o/d_o = 1$ and $D_o/d_o = 2$.

The limiting workpiece dimensions in the hardness test depends on the degree of the deformation involved in the test. However, if the impression is made near the yield point, more conservative values for the limiting workpiece dimensions seem to be appropriate.

With further penetration of the punch beyond the yield point, the mode of bulk deformation becomes significant. In spite of the importance of the deformation in this range, no theoretical analysis has been attempted for deep indentation except the work of Johnson and Kudo [23] who used an upper-bound approach for plane-strain deep indentation.

5. CONCLUSIONS

- (1) For the flat punch indentation of SAE 1215 steel, as-received, the yield point pressure remained unchanged for the range of specimen dimensions of $H_o/d_o \geq 2.00$ and $D_o/d_o \geq 4.00$, and the yield point value was $p = 3.1Y$.
- (2) In the range of punch displacement investigated, the pressure-displacement curves become identical for $H_o/d_o \geq 2.00$ for the same punch diameter, but no limiting value was found for $D_o/d_o \leq 6.00$.
- (3) The same conclusions are reached as in (1) and (2) above for the indentation of SAE 1215 steel as-received, with the punch

having a hemispherical end.

- (4) The deformation behavior of the two states of SAE 1215 steel near the yield point is characterized by "piling-up" and "sinking-in" for as-received and annealed materials, respectively.
- (5) Edge-lifting, as an initial mode of bulk deformation, occurred for the workpiece dimensions of $H_0/D_0 < 0.5$ with both types of punches.
- (6) Flow lines revealed the differences in the deformation behavior, depending on the punch shape, workpiece dimensions, and the material's properties; the location of the critical state for fracturing was found to be in the material around the edge of the punch.

6. REFERENCES

- [1] L. Prandtl, "Über die Härte Plastischer Körper," Nachrichten der Akademie der Wissenschaften, Göttingen, Mathematisch-Physikalische Klasse, 1920, p. 74.
- [2] R. Hill, The Mathematical Theory of Plasticity, Clarendon Press, Oxford, 1950.
- [3] R. Hill, E. H. Lee, and S. J. Tupper, "A Method of Numerical Analysis of Plastic Flow in Plane Strain and Its Application to the Compression of a Ductile Material between Rough Plates," Trans. ASME, J. Appl. Mech., vol. 18, 1951, p. 46.
- [4] A. P. Green, "A Theoretical Investigation of the Compression of a Ductile Material between Smooth Flat Dies," Philosophical Magazine, vol. 42, 1951, p. 400.
- [5] R. T. Shield, "On the Plastic Flow of Metals under Conditions of Axial Symmetry," Proc. Roy. Soc., A233, 1955, p. 267.
- [6] D. Tabor, The Hardness of Metals, Oxford University Press, 1951.
- [7] D. S. Dugdale, "Wedge Indentation Experiments with Cold-Worked Metals," Journal of the Mechanics and Physics of Solids, vol. 2, 1953, pp. 14-26.
- [8] D. S. Dugdale, "Cone Indentation Experiments," Journal of the Mechanics and Physics of Solids, vol. 2, 1954, pp. 265-277.
- [9] L. E. Samuels and T. O. Mulhearn, "An Experimental Investigation of the Deformed Zone Associated with Indentation Hardness Impressions," Journal of the Mechanics and Physics of Solids, vol. 5, 1957, pp. 125-134.
- [10] T. O. Mulhearn, "The Deformation of Metals by Vickers-Type Pyramidal Indenters," Journal of the Mechanics and Physics of Solids, vol. 7, 1959, pp. 85-96.
- [11] J. B. Haddow and W. Johnson, "Indenting with Pyramids - I. Theory," International Journal of Mechanical Sciences, vol. 3, 1961, pp. 229-238.
- [12] J. B. Haddow and W. Johnson, "Indenting with Pyramids - II. Experimental," International Journal of Mechanical Sciences, vol. 4, 1962, pp. 1-13.
- [13] F. J. Lockett, "Indentation of a Rigid/Plastic Material by a Conical Indenter," Journal of the Mechanics and Physics of Solids, vol. 11, 1963, pp. 345-355.

- [14] A. G. Atkins and D. Tabor, "Plastic Indentation in Metals with Cones," *Journal of the Mechanics and Physics of Solids*, vol. 13, 1965, pp. 149-164.
- [15] C. H. Lee and Shiro Kobayashi, "Elastoplastic Analysis of Plane-Strain and Axisymmetric Flat Punch Indentation by the Finite-Element Method," *International Journal of Mechanical Sciences*, vol. 12, 1970, pp. 349-370.
- [16] S. Takahashi, "Strain Distribution on the Surface of the Blank in Cold Hobbing. Part 1," *Journal of Japan Society for Technology of Plasticity*, vol. 9, No. 94, 1968, pp. 803-813.
- [17] S. Takahashi, "Strain Distribution on the Surface of the Blank in Cold Hobbing. Part 2," *Journal of Japan Society for Technology of Plasticity*, vol. 11, No. 110, 1970, pp. 184-191.
- [18] P. H. Abramowitz and J. A. Schey, "Principles of Incremental Forging," Final Report to the Navy, Naval Air Systems Command, July 1970.
- [19] A. T. Male, "Incremental Forging. Part I: The Plastic Indentation of Aluminum with Circular Punches," Technical Report No. AFML-TR-69-109, Part 1, April 1969.
- [20] E. Levin, "Indentation Pressure of a Smooth Circular Punch," *Quarterly of Applied Mathematics*, vol. 13, 1955, pp. 133-137.
- [21] W. F. Chen, "Plastic Indentation of Metal Blocks by Flat Punch," *Journal of Engineering Mechanics Division, Proceedings of the ASCE*, June 1970, pp. 353-360.
- [22] A. Iu Ishlinsky, "The Problem of Plasticity with Axial Symmetry and Brinell's Test," *Journal of Applied Math. and Mech. (USSR)*, vol. 8, 1944, pp. 201-224.
- [23] W. Johnson and H. Kudo, "Plane-Strain Deep Indentation," *Proc. 5th Int. Machine Tool Design and Research Conference*, Sept. 1964, pp. 441-447.

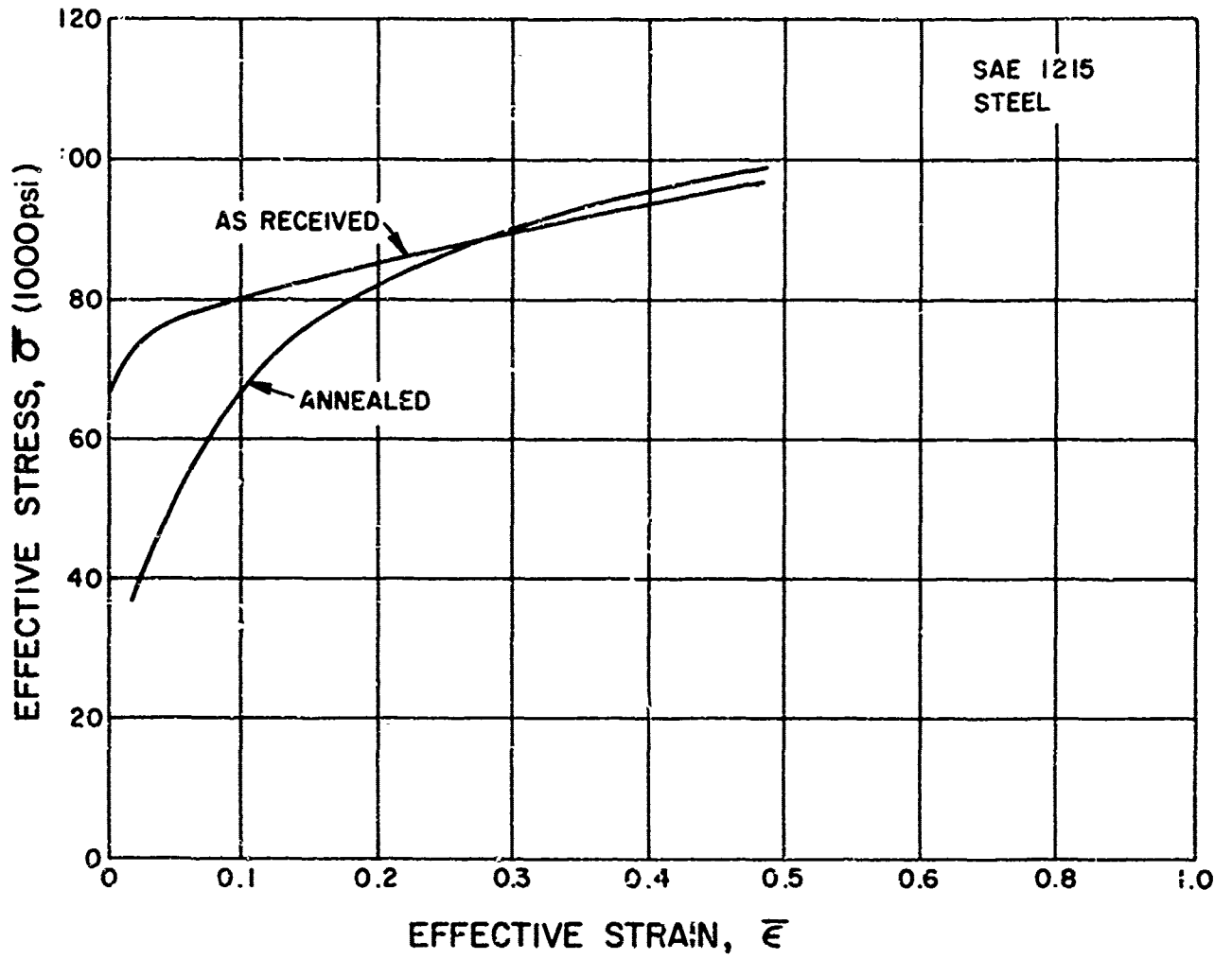


Fig. 1 Stress-strain curves for SAE 1215 steels: as-received and annealed conditions.

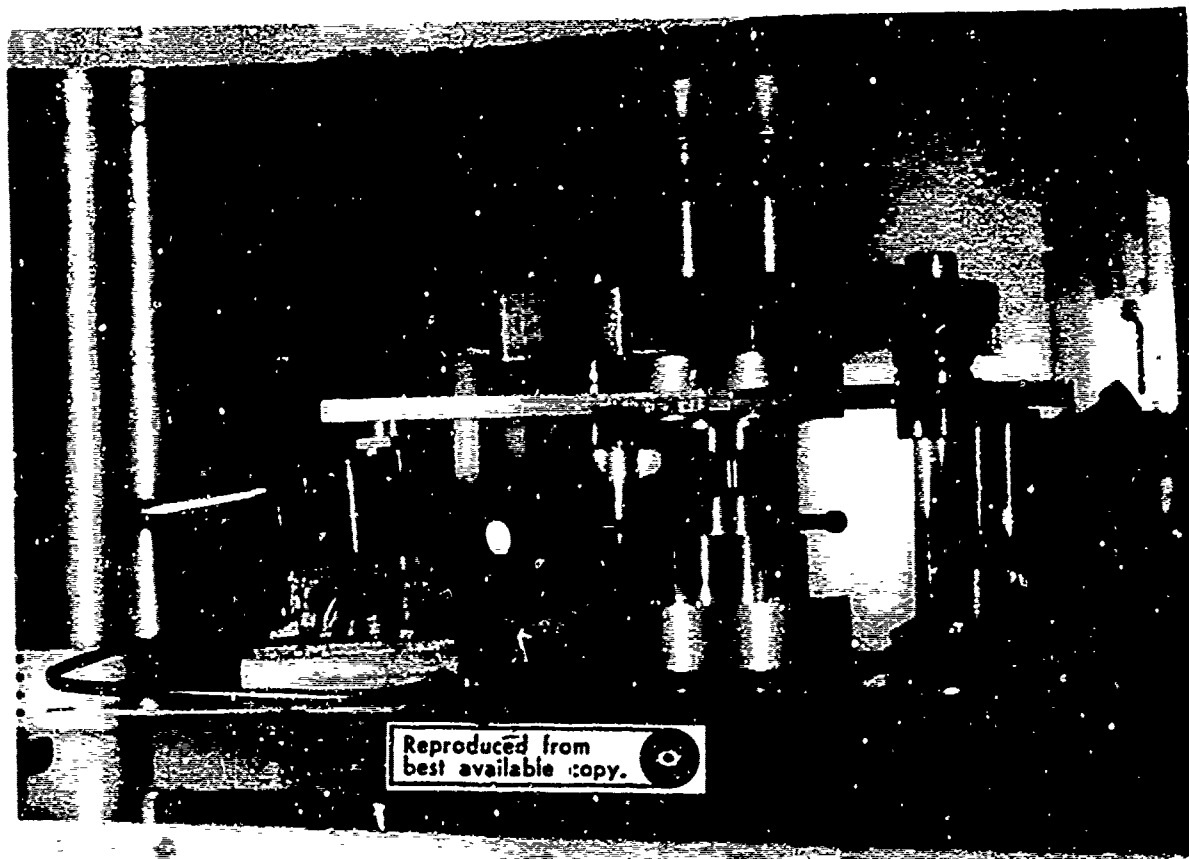


Fig. 2 Experimental setup.

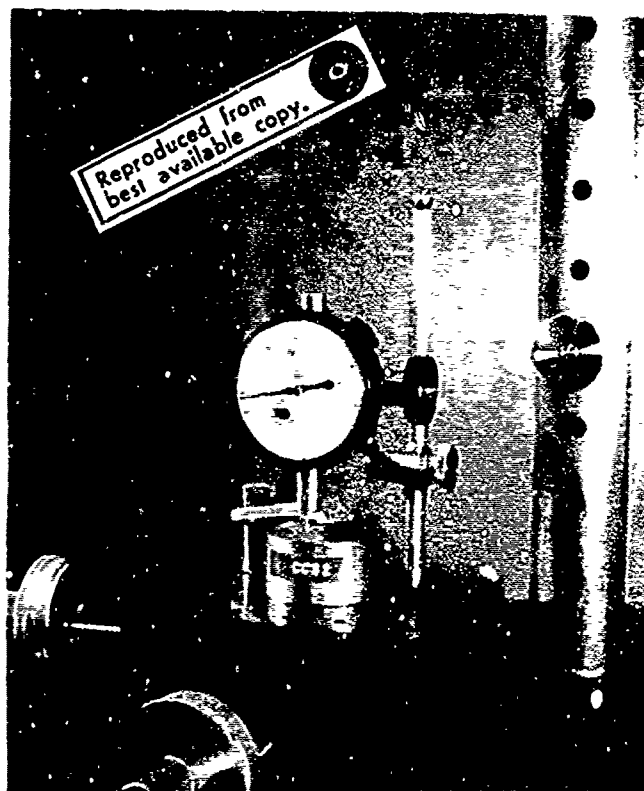


Fig. 3 Measurement of workpiece geometry.

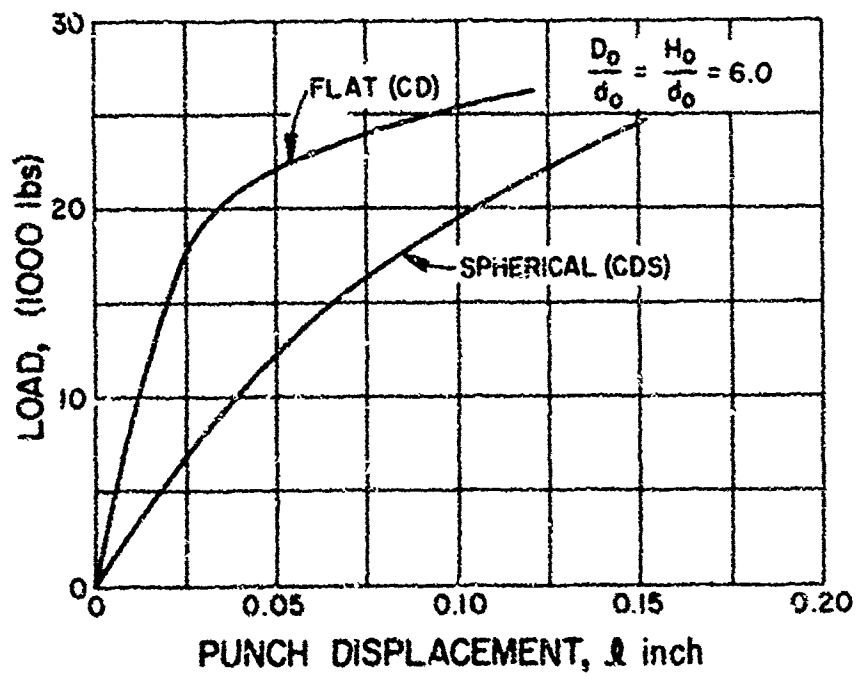


Fig. 4 Typical load-displacement curves for punches with flat and hemispherical ends. Conditions: CD and CDS.

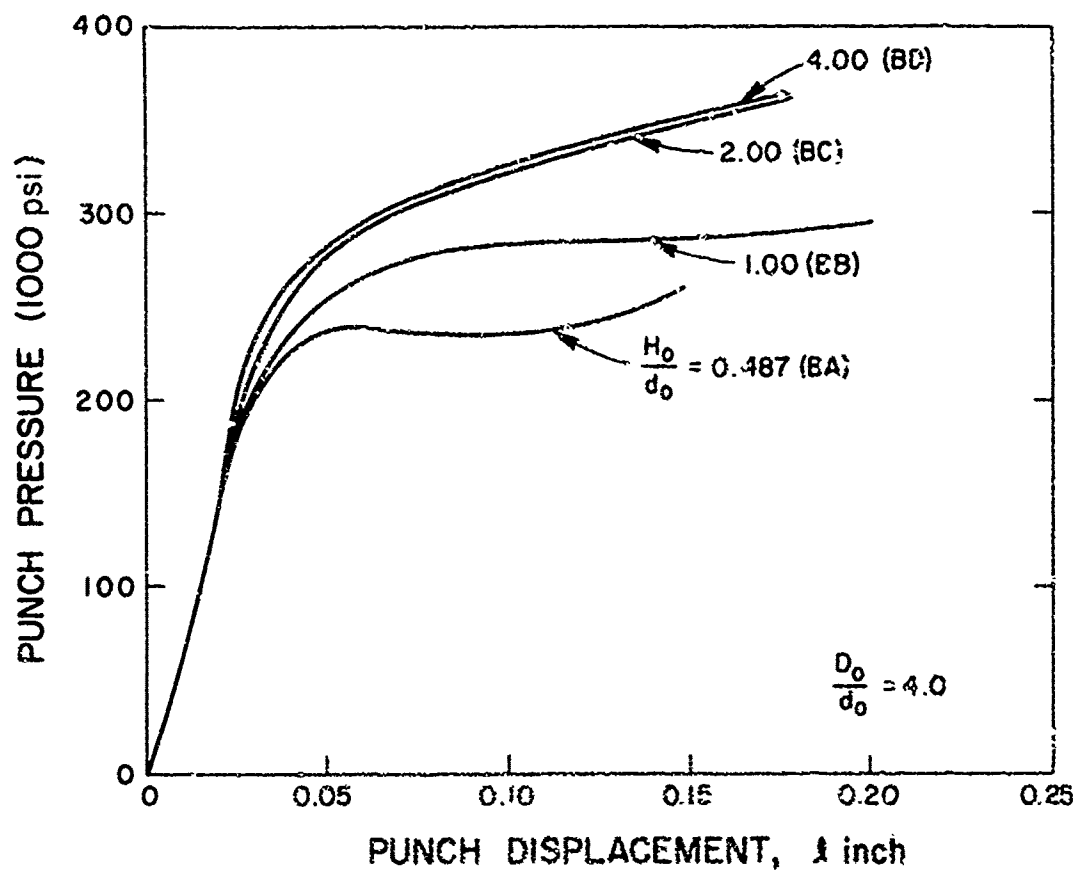


Fig. 5 Pressure-displacement curves for a flat punch of 0.44 in. diameter for various workpiece thicknesses.

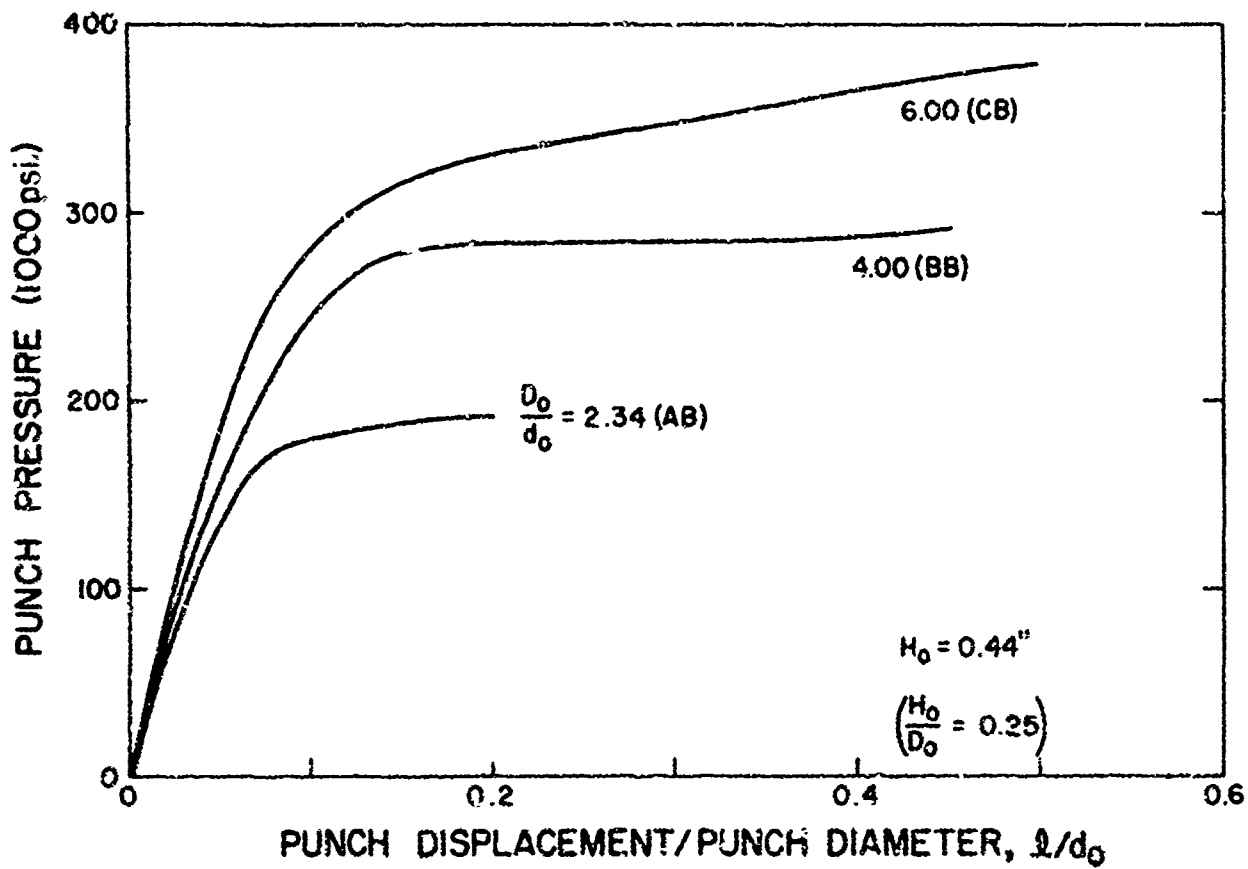


Fig. 6a Effect of flat punch diameter on pressure-displacement curves for a workpiece of 0.44 in. thickness.

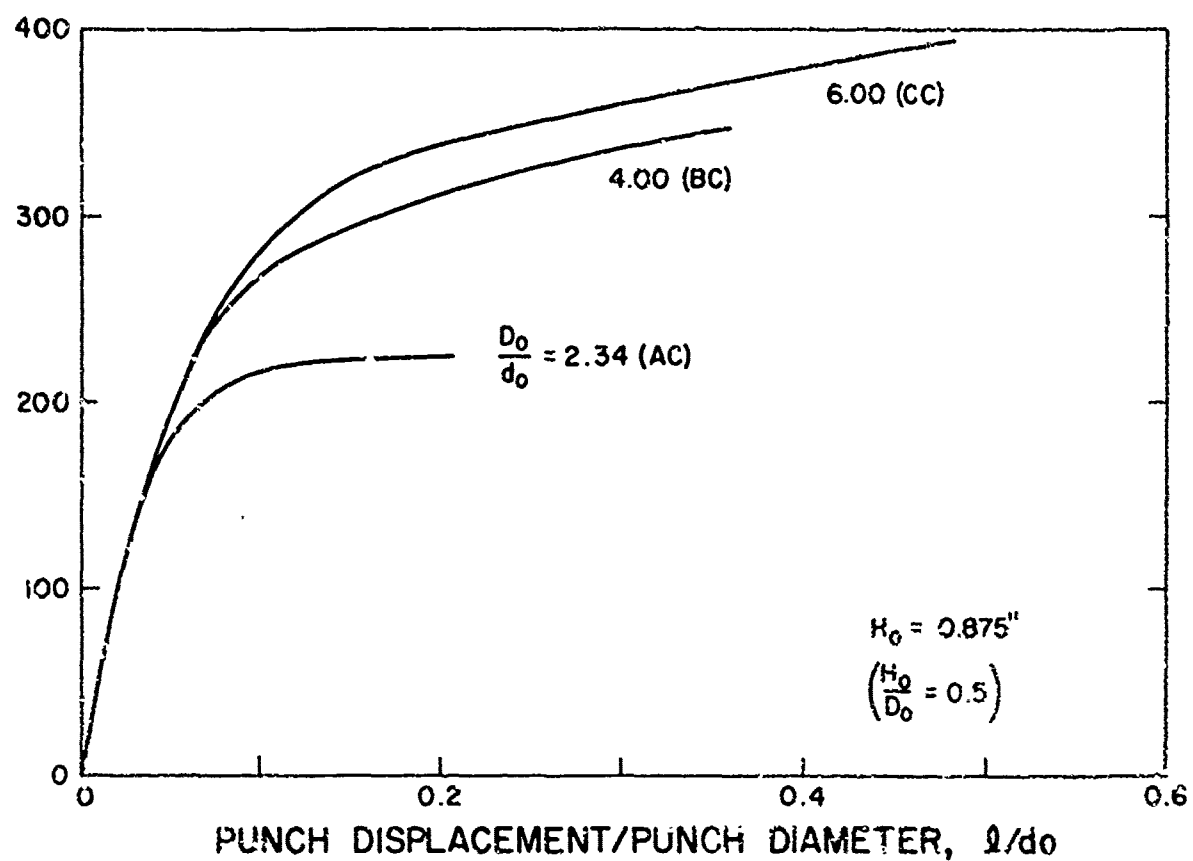


Fig. 6b Effect of flat punch diameter on pressure-displacement curves for a workpiece of 0.875 in. thickness.

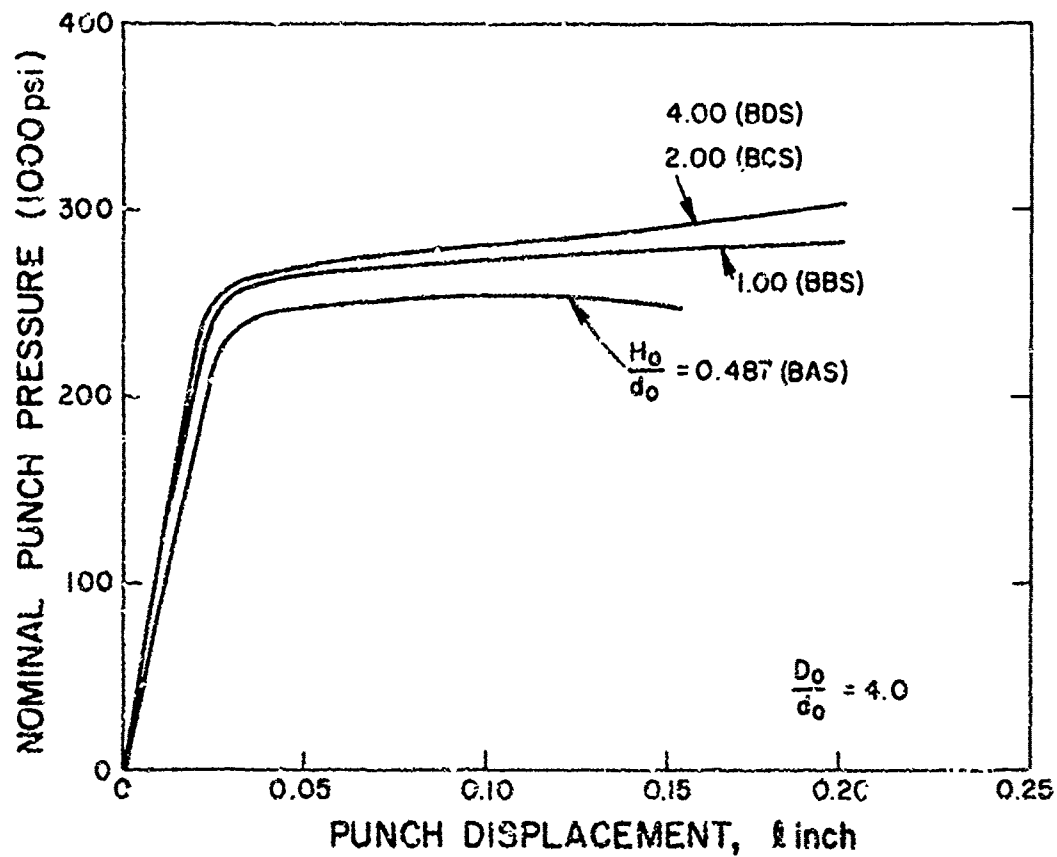


Fig. 7 Pressure-displacement curves for a hemispherical punch of 0.14 in. diameter for various work-piece thicknesses.

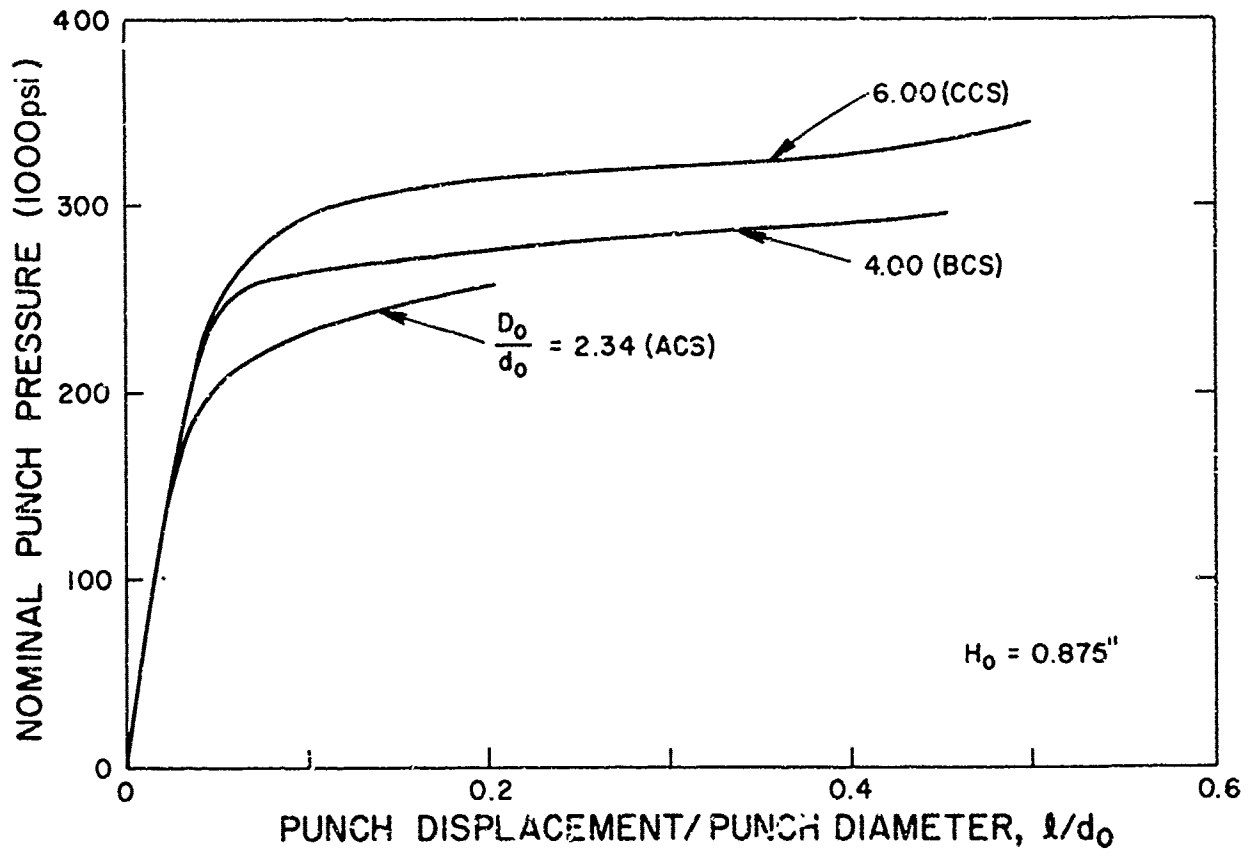
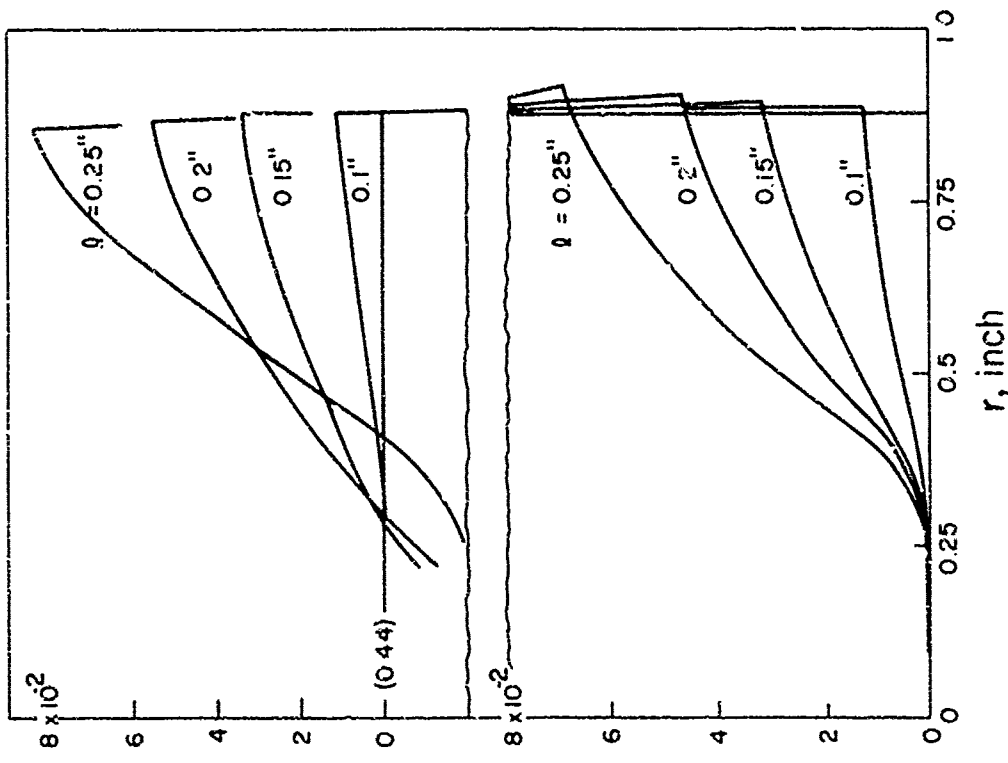
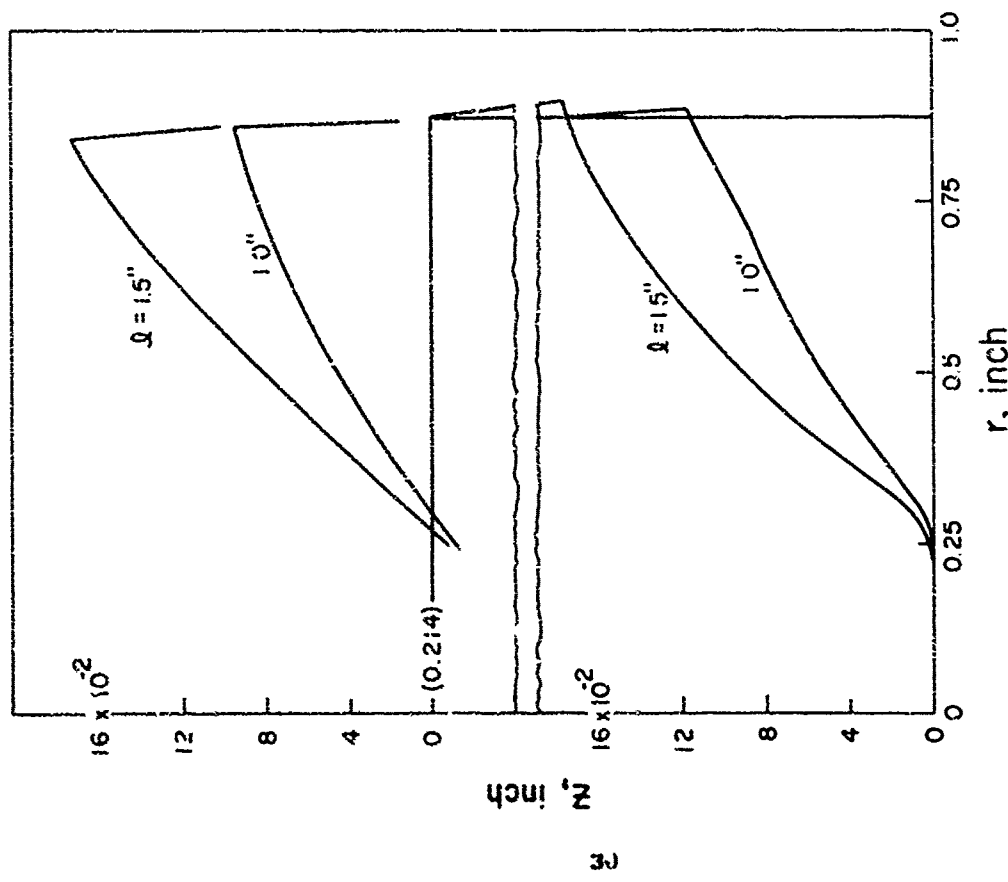


Fig. 8 Effect of hemispherical punch diameter on pressure-displacement curves for a workpiece of 0.875 in. thickness.



(a) BA: $\frac{D_0}{d_0} = 4.0$
 $\frac{H_0}{d_0} = 0.487$



(b) BB: $\frac{D_0}{d_0} = 4.00$
 $\frac{H_0}{d_0} = 1.00$

Fig. 9a, b Effect of workpiece thickness on the surface geometry for flat punch indentation. $D_0/d_0 = 4.00$, and (a) $H_0/d_0 = 0.487$ (BA); (b) $H_0/d_0 = 1.00$ (BB);

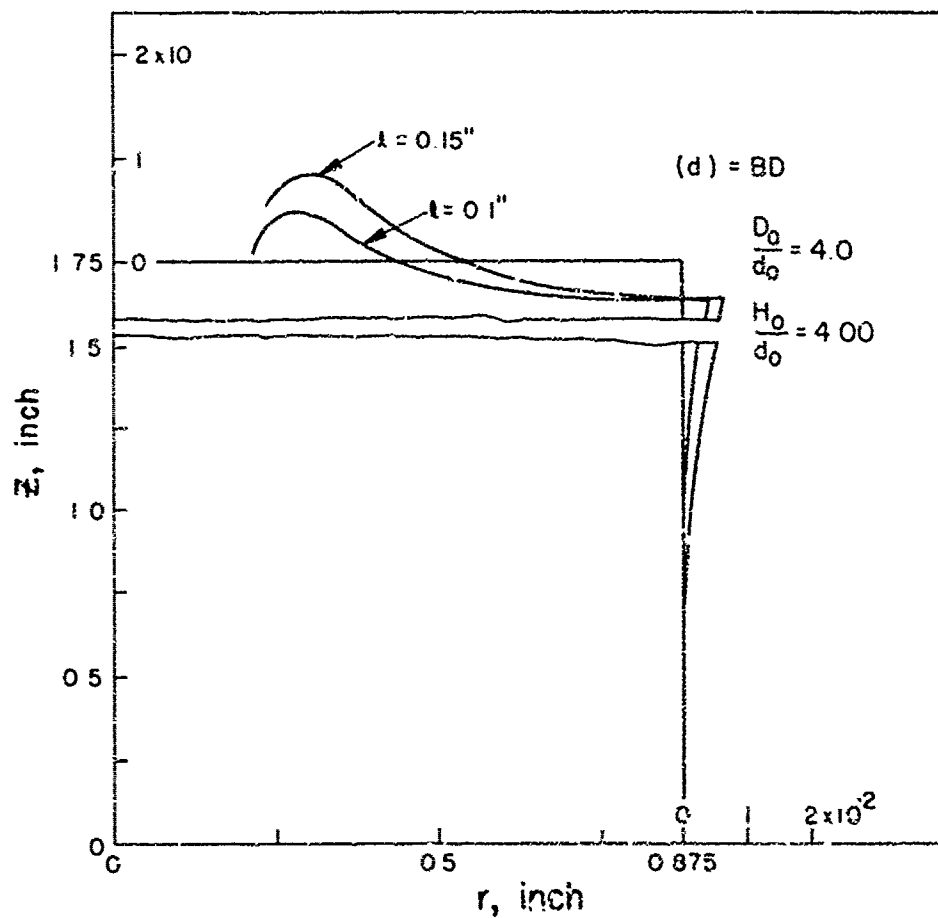
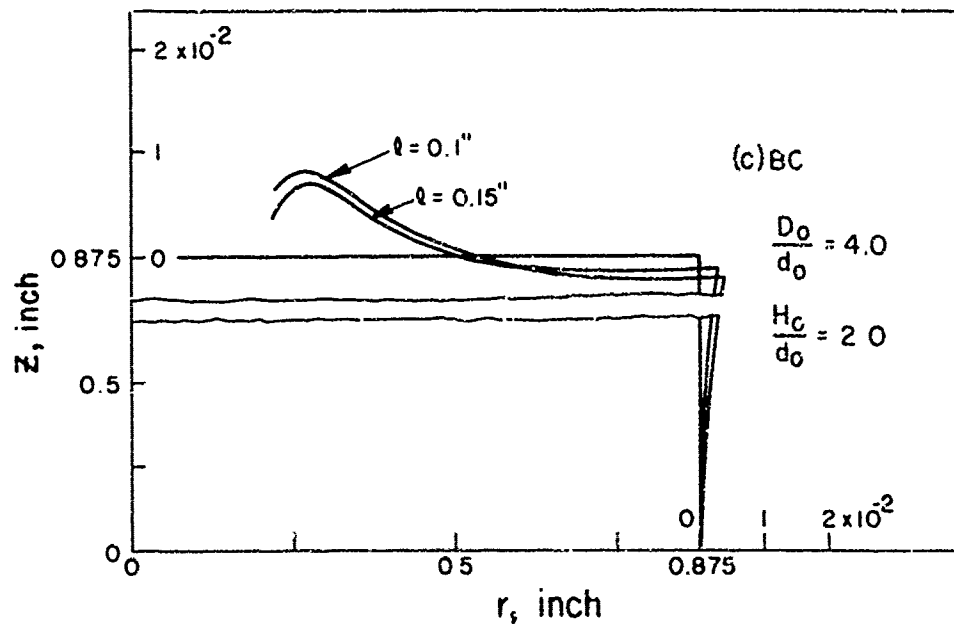


Fig. 9c, d Effect of workpiece thickness on the surface geometry for flat punch indentation. $D_0/d_0 = 4.00$, and (c) $H_0/d_0 = 2.00$ (BC); (d) $H_0/d_0 = 4.00$ (BD).

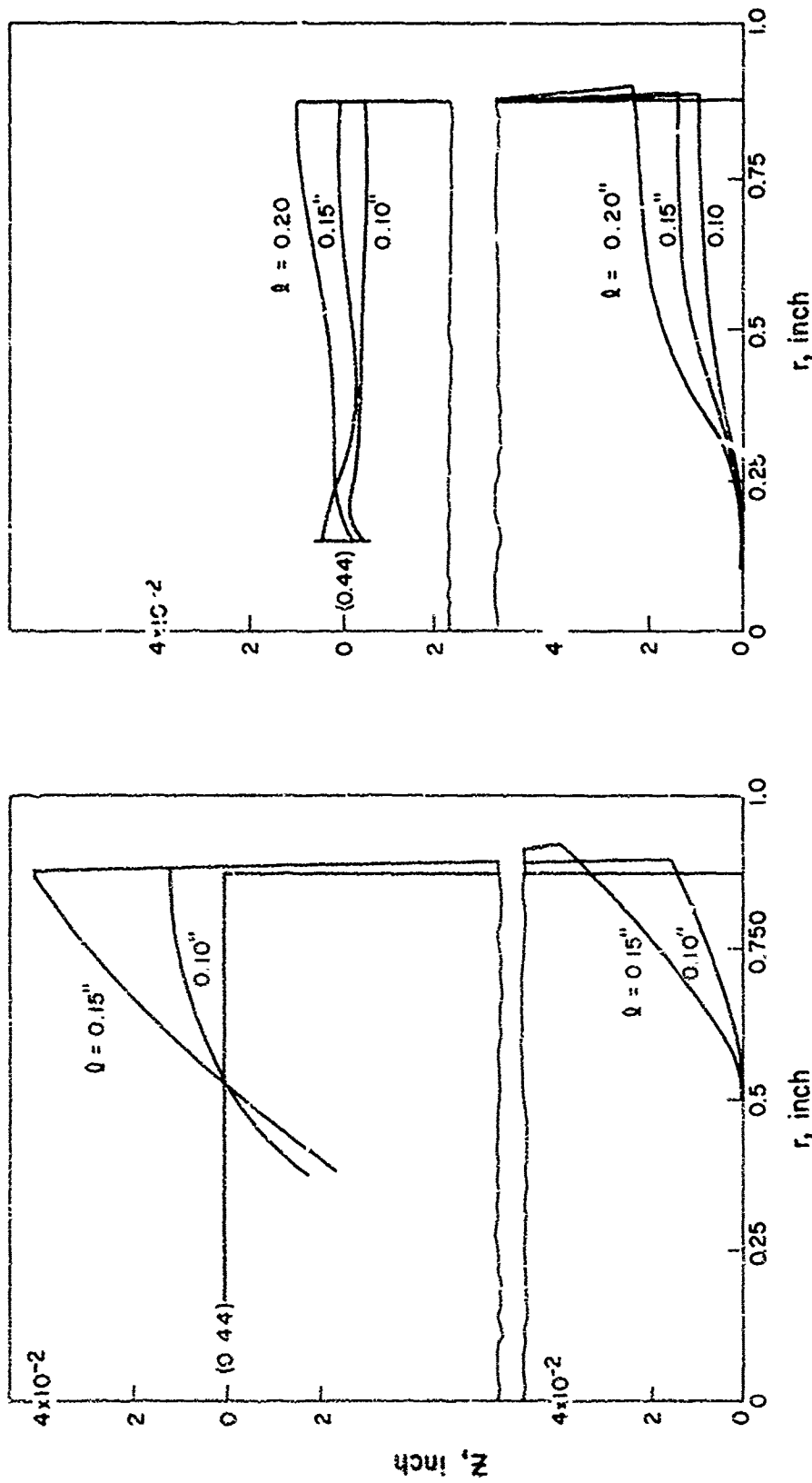


Fig. 10 Effect of flat punch diameter on the surface geometry for a workpiece of 0.44 in. thickness.

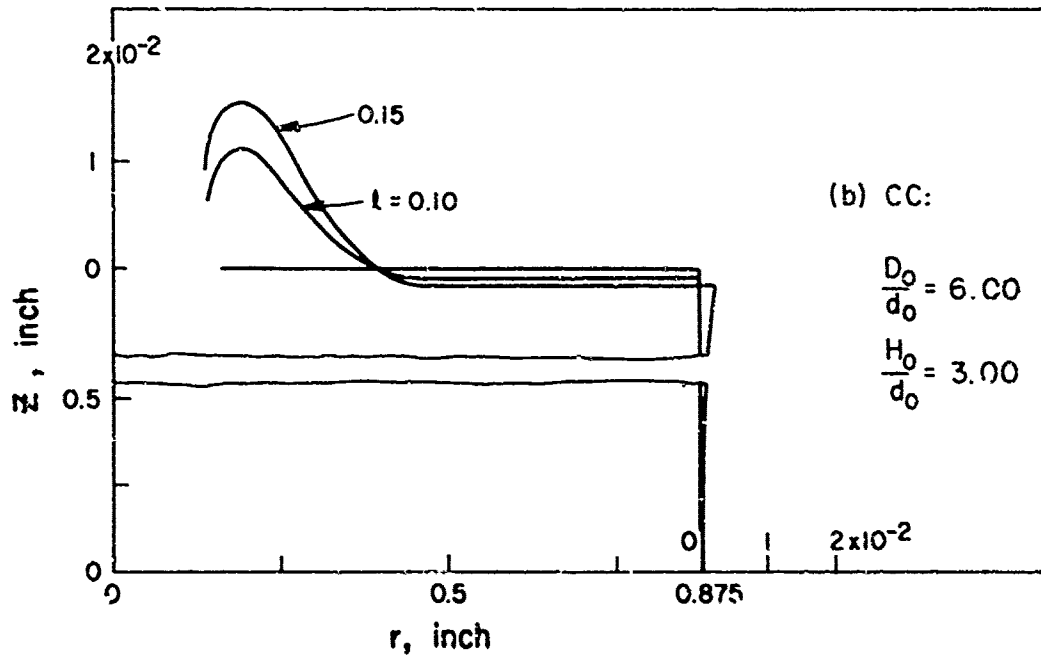
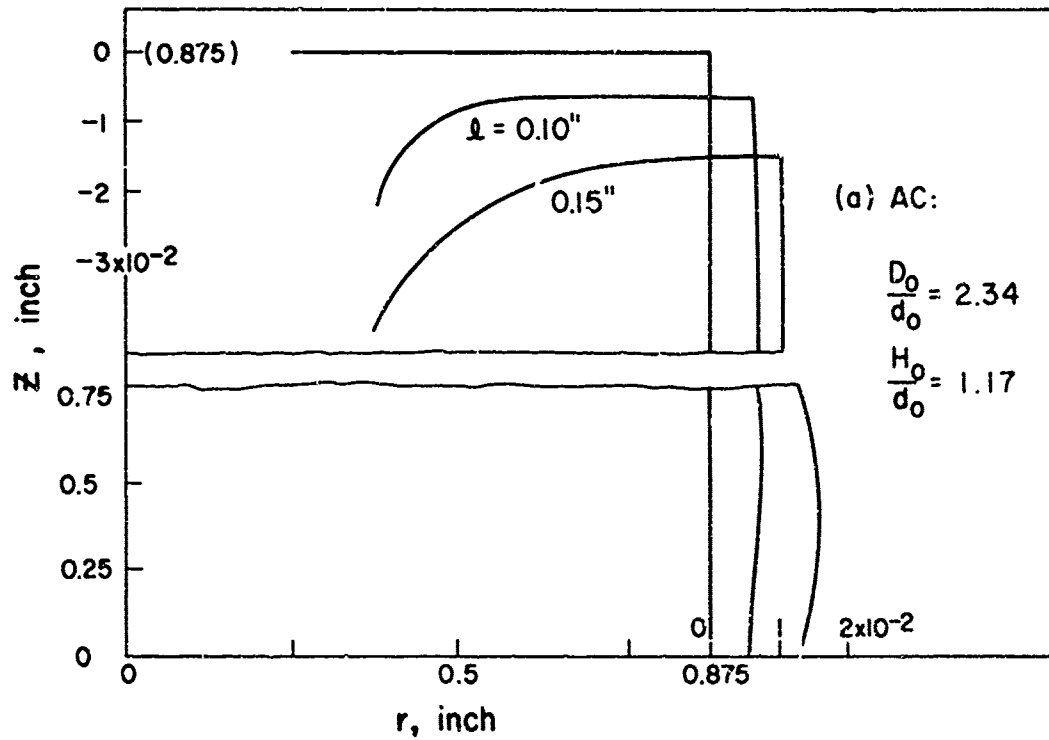


Fig. 11 Effect of flat punch diameter on the surface geometry for a workpiece of 0.875 in. thickness.

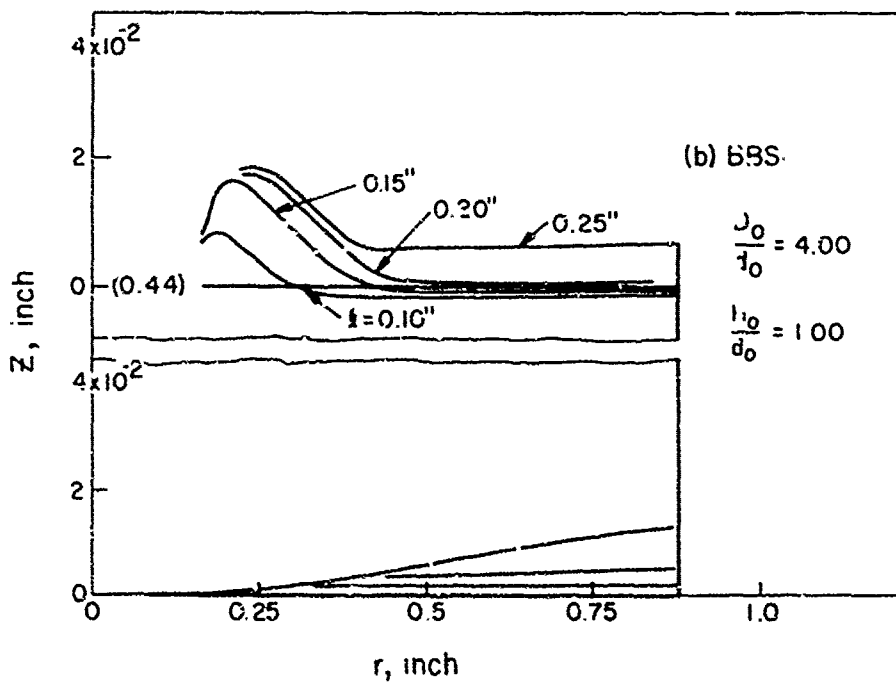
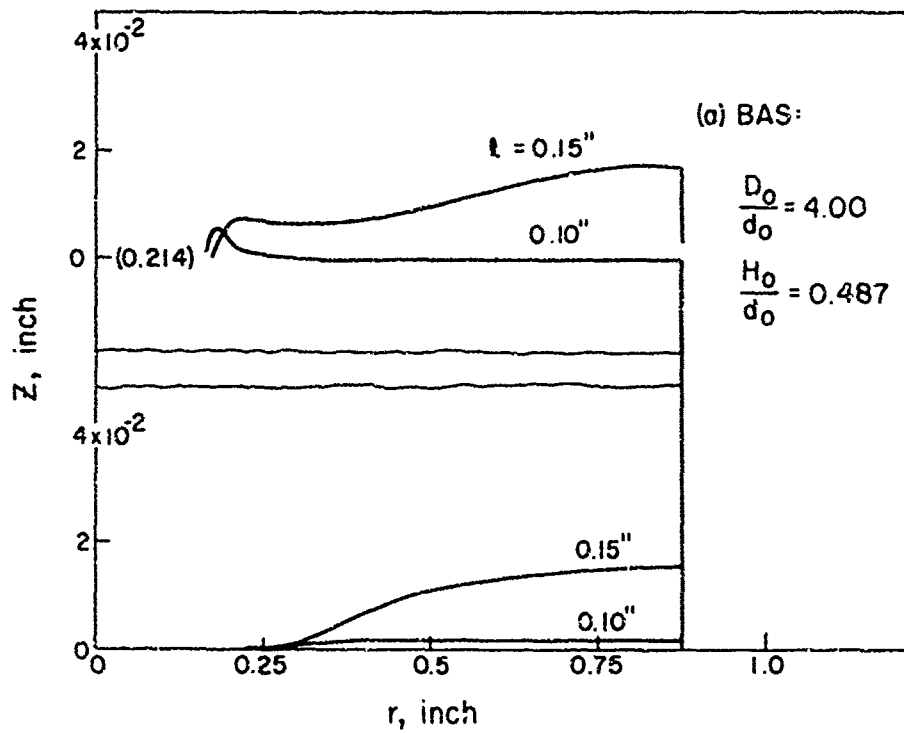


Fig. 12a, b Effect of workpiece thickness on the surface geometry for a hemispherical punch.

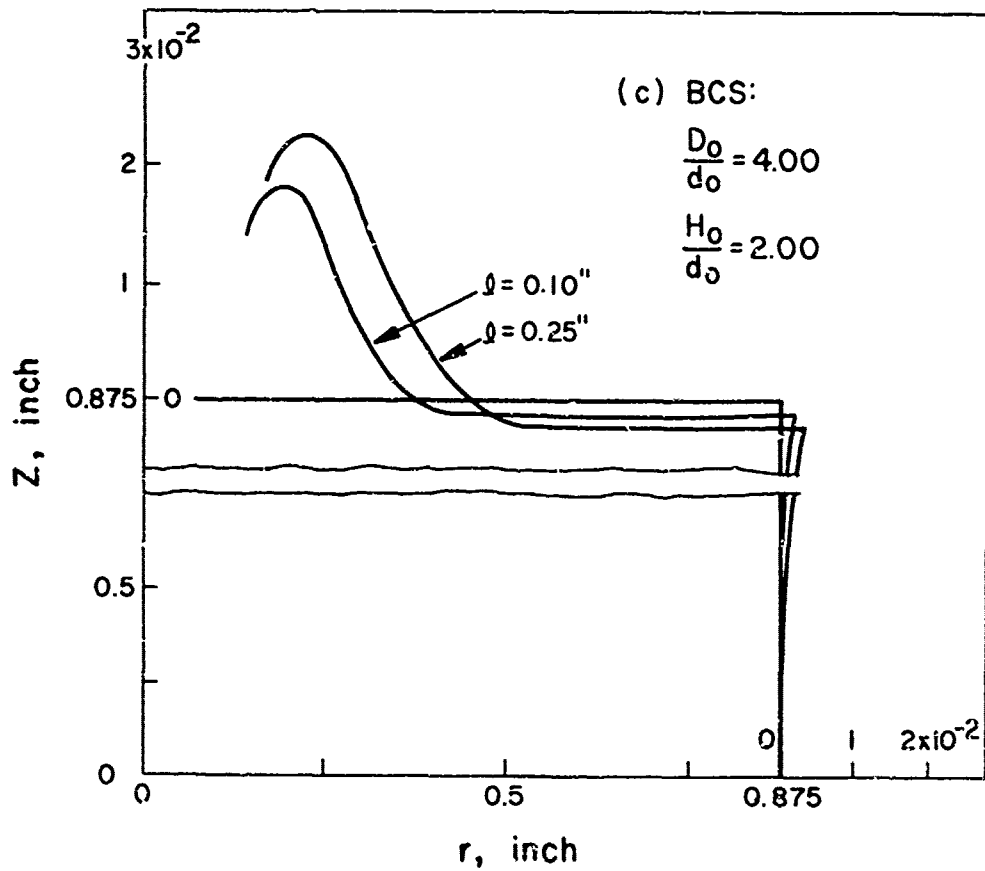


Fig. 12c Effect of workpiece thickness on the surface geometry for a hemispherical punch.

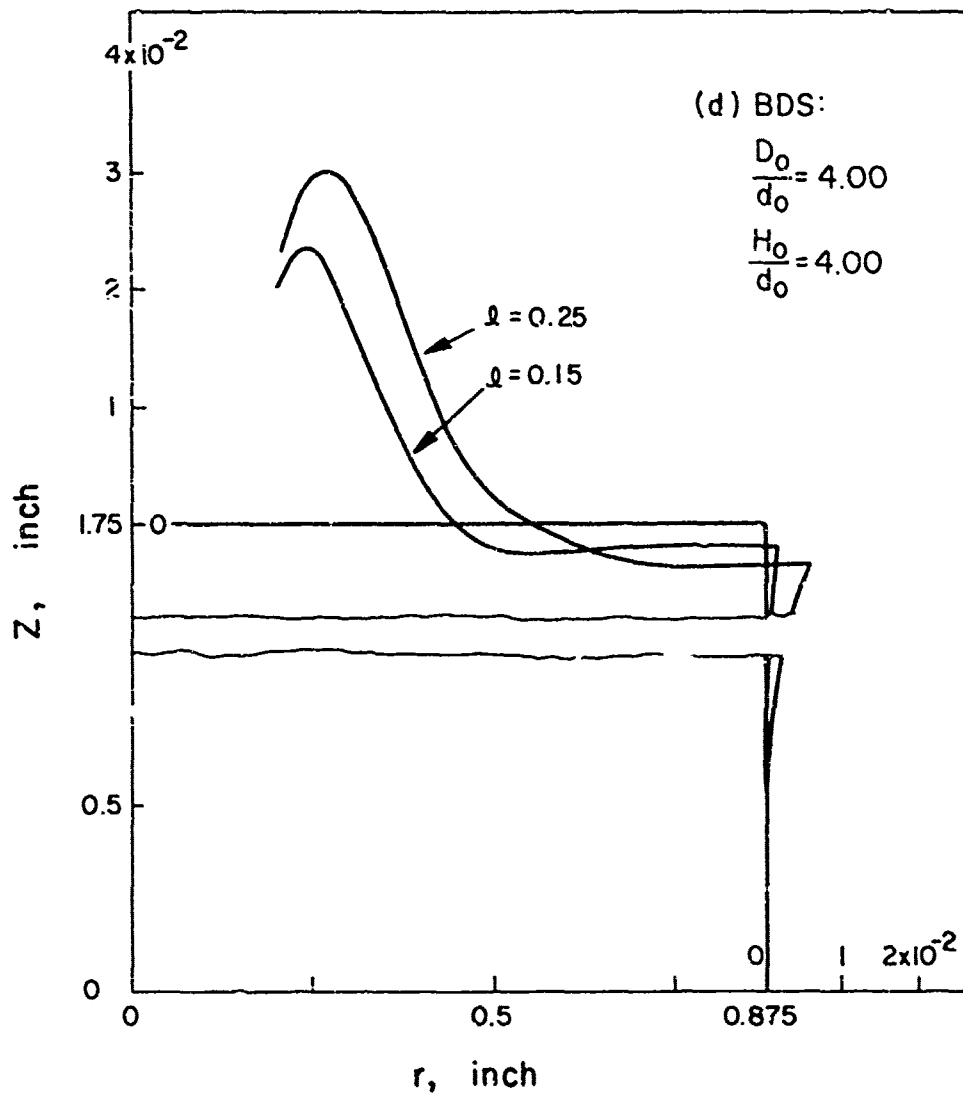


Fig. 12d Effect of workpiece thickness on the surface geometry for a hemispherical punch.

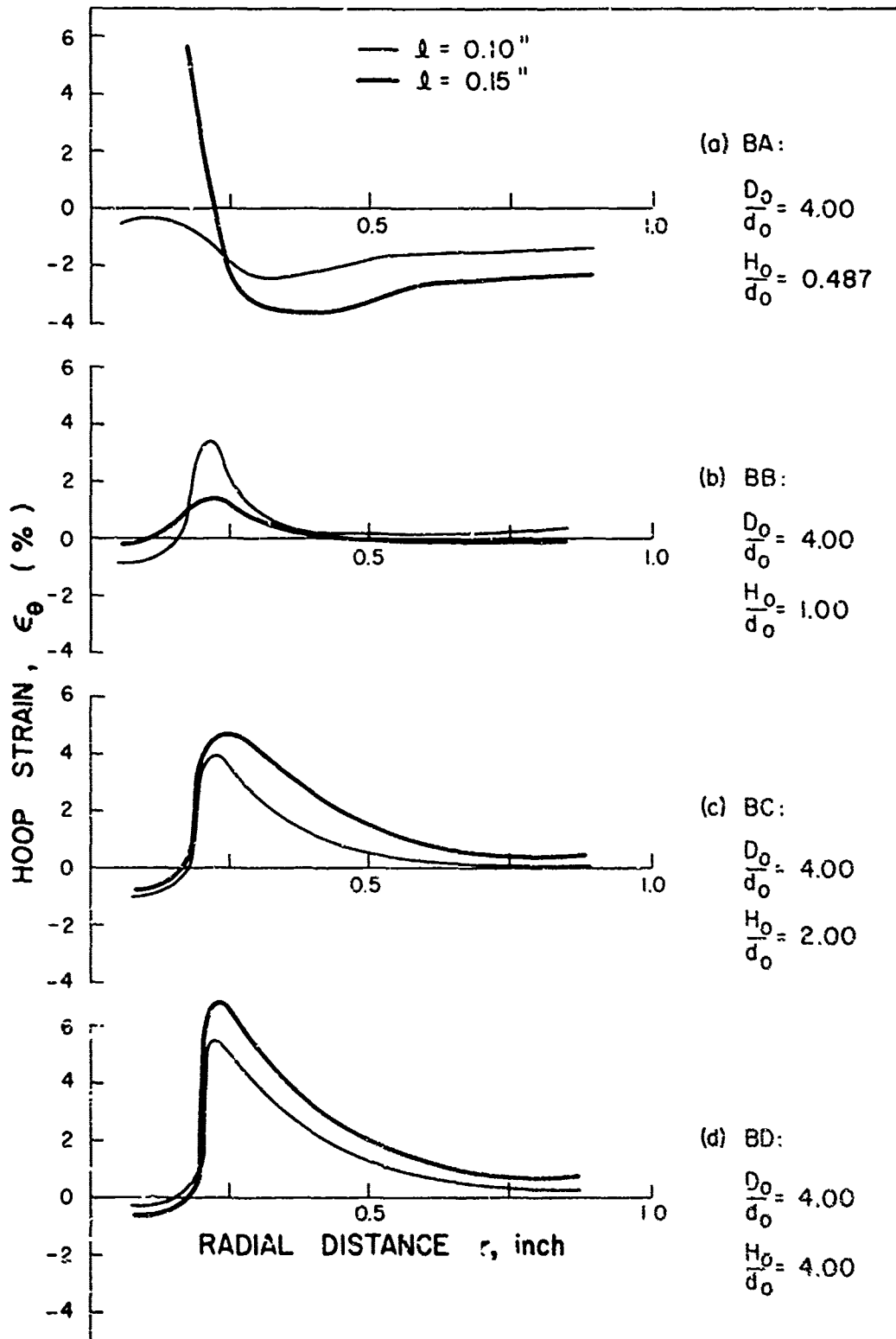


Fig. 13 Effect of workpiece thickness on strain distributions for flat punches.

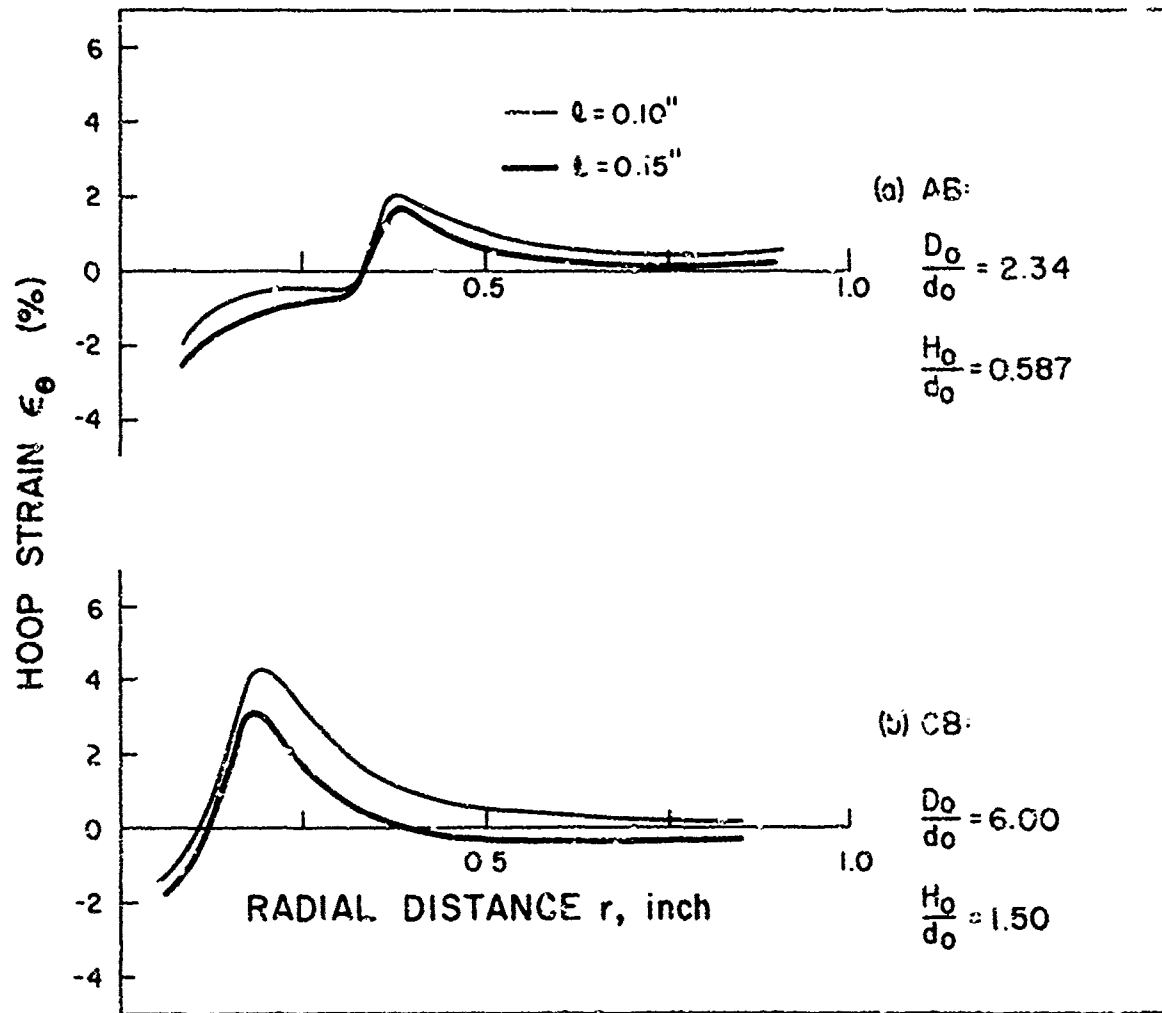


Fig. 14 Effect of flat punch diameter on strain distributions for $H_0/D_0 = 0.250$.

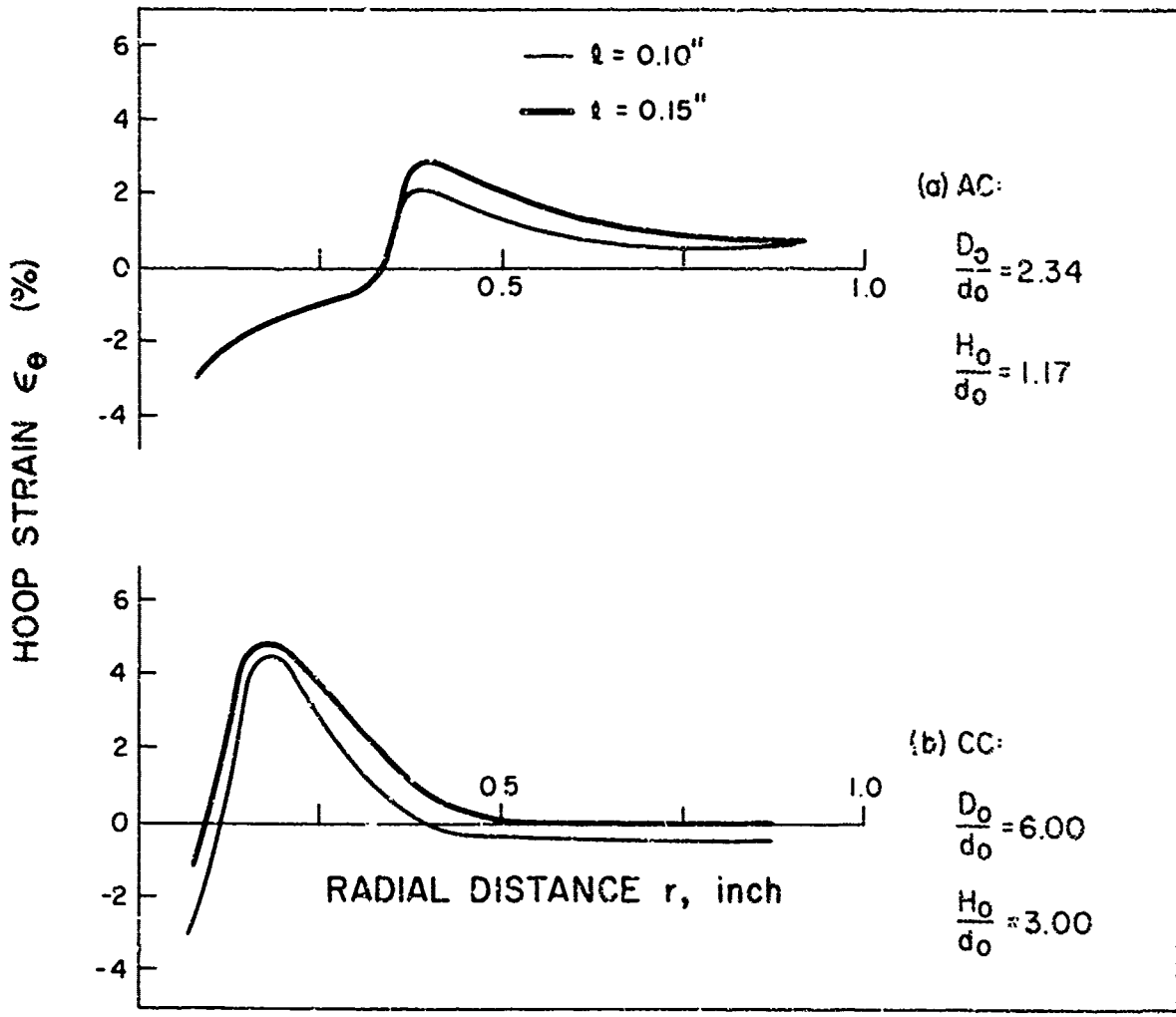


Fig. 15 Effect of flat punch diameter on strain distributions for $H_0/D_0 = 0.500$.

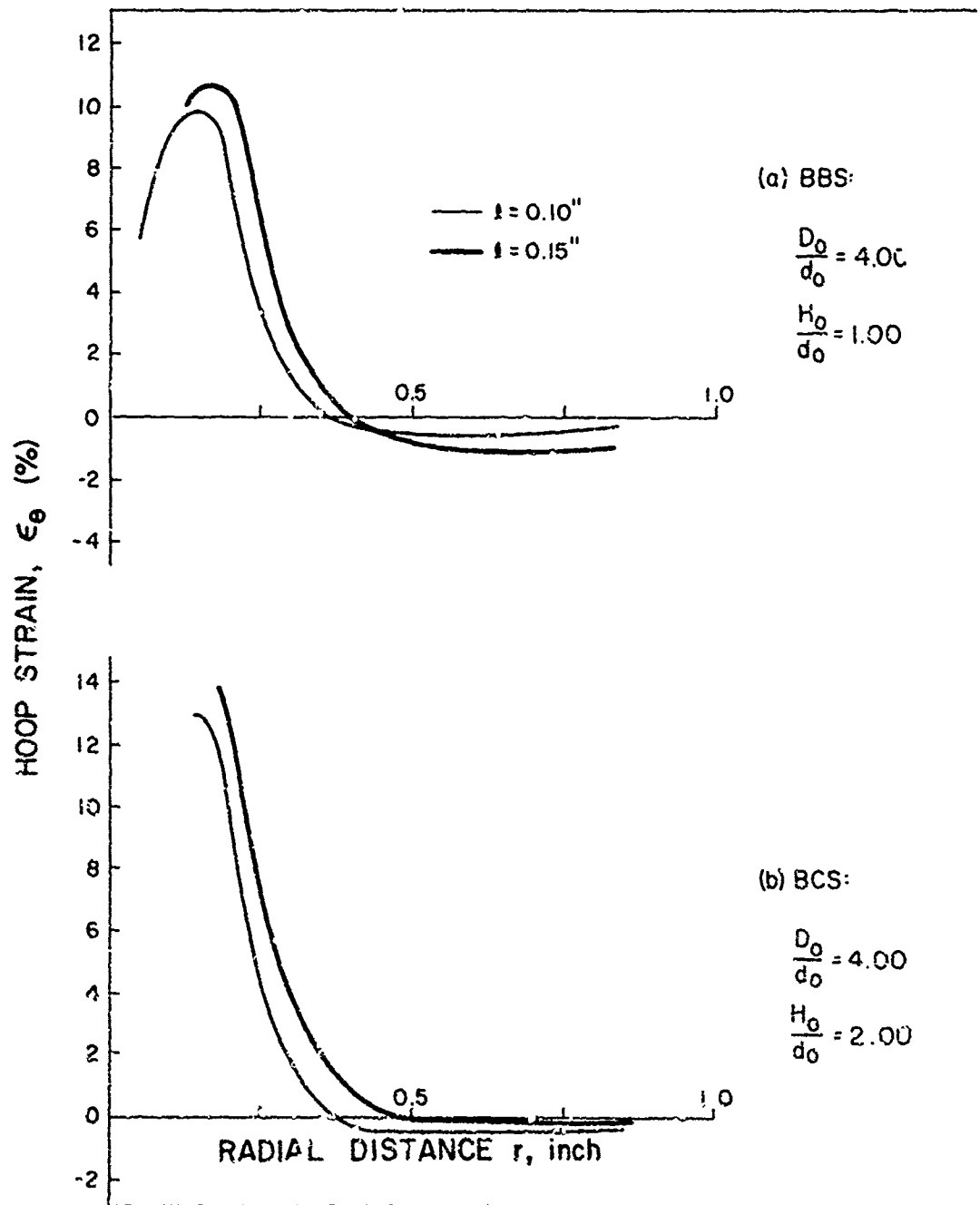


Fig. 16 Strain distributions for the punch with a hemispherical end.

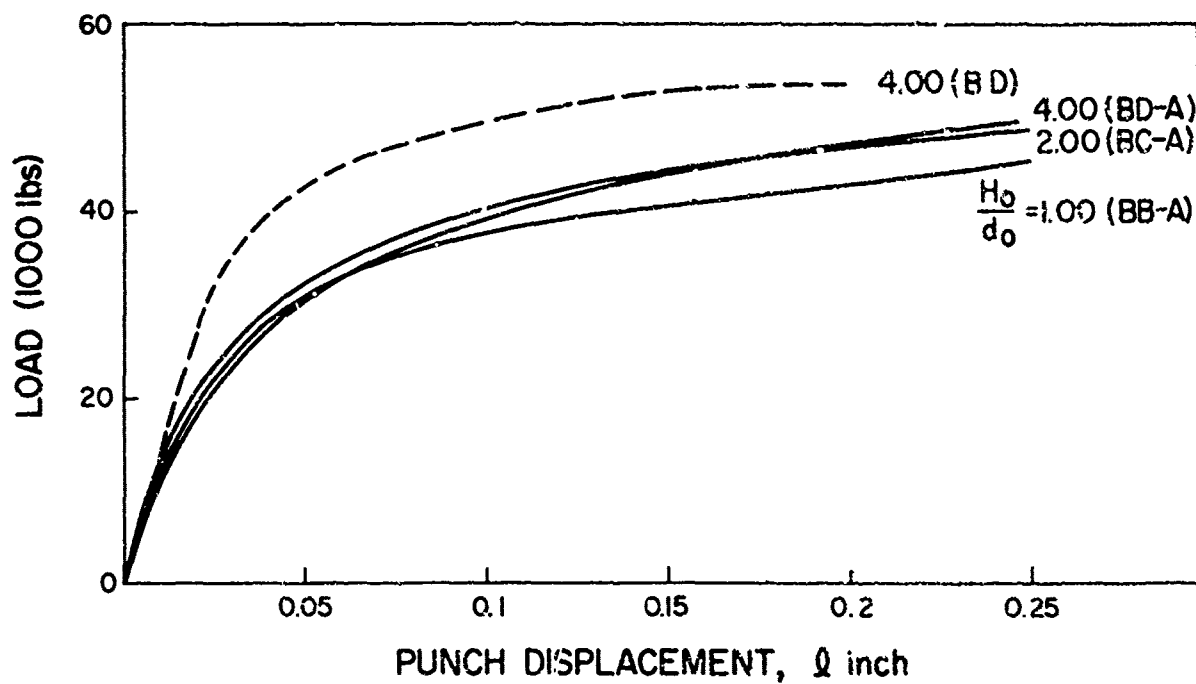


Fig. 17 Load-displacement curves for a flat punch of $D_0/d_0 = 4.00$.

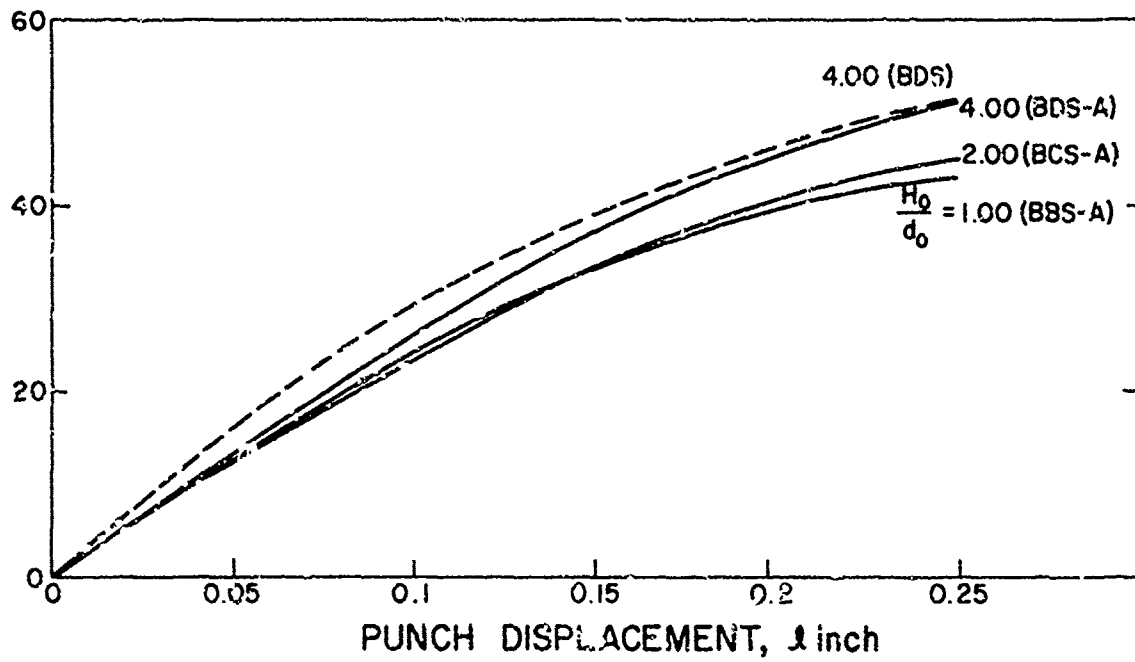


Fig. 18 Load-displacement curves for a hemispherical punch of $D_0/d_0 = 4.00$.

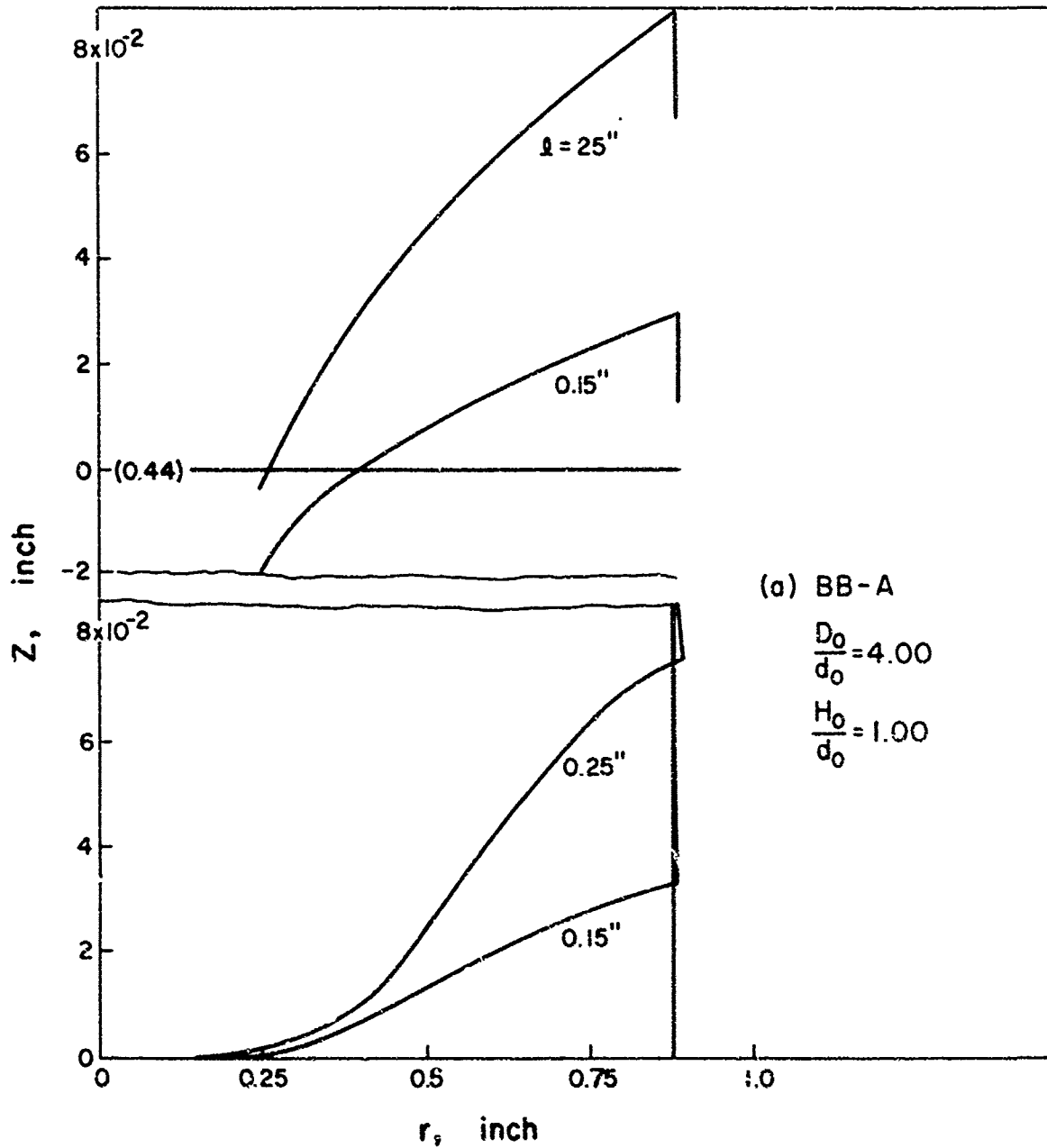


Fig. 19a Surface geometry in flat punch indentation for annealed steel.

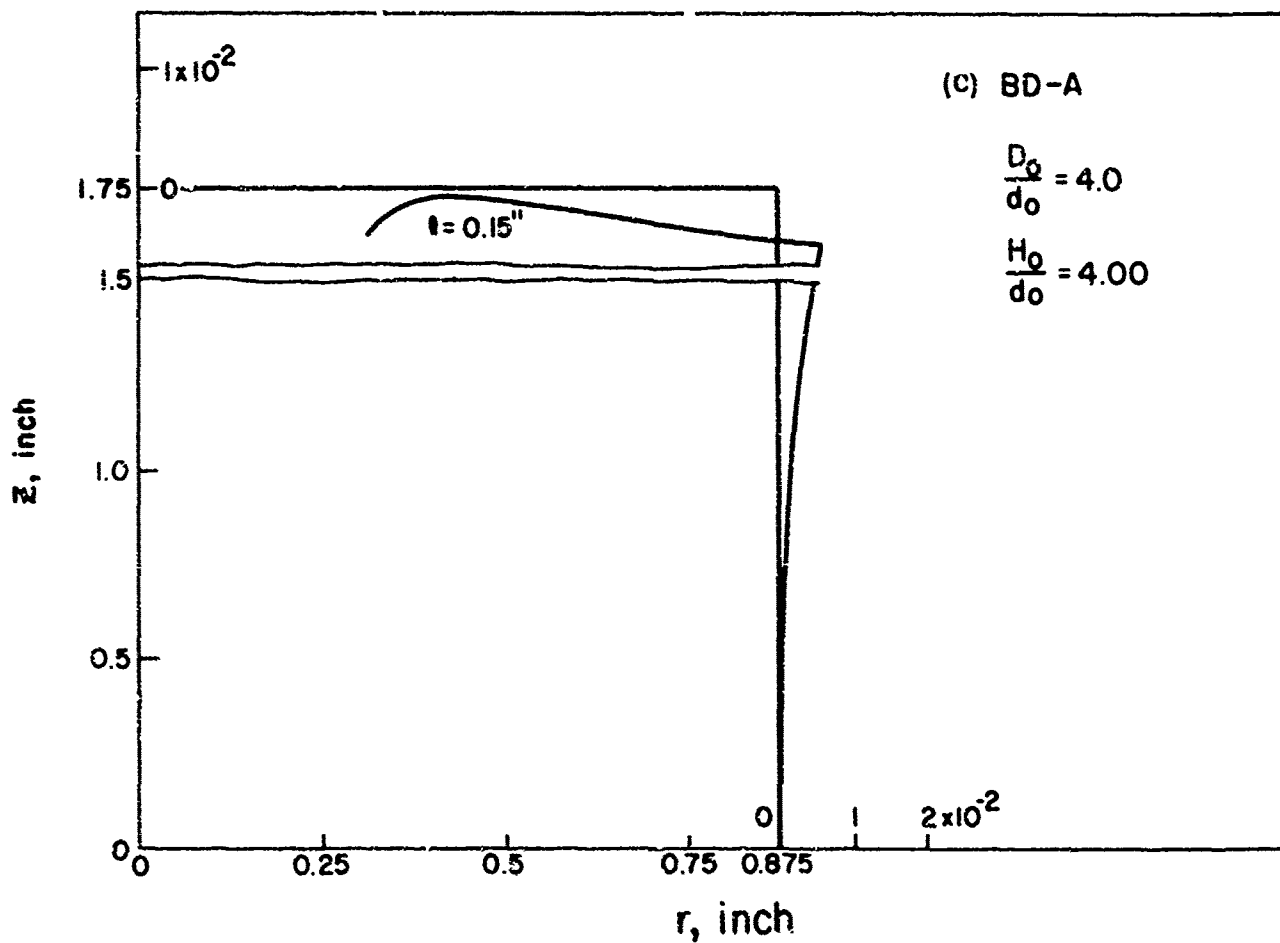
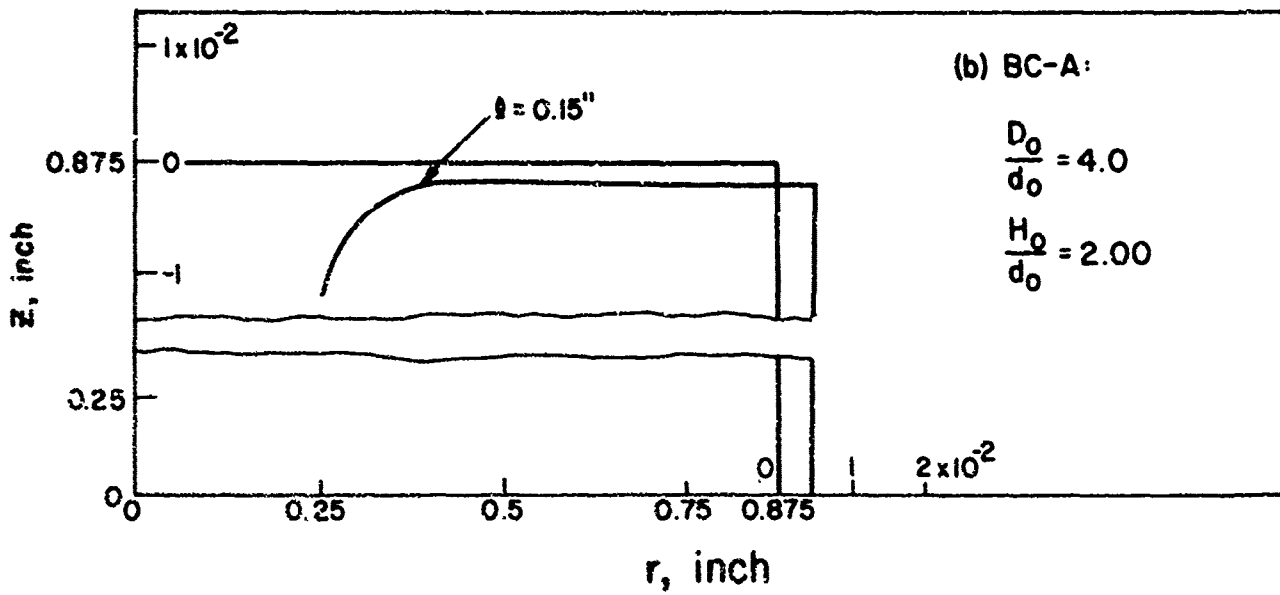


Fig. 19b, c Surface geometry in flat punch indentation for annealed steel.

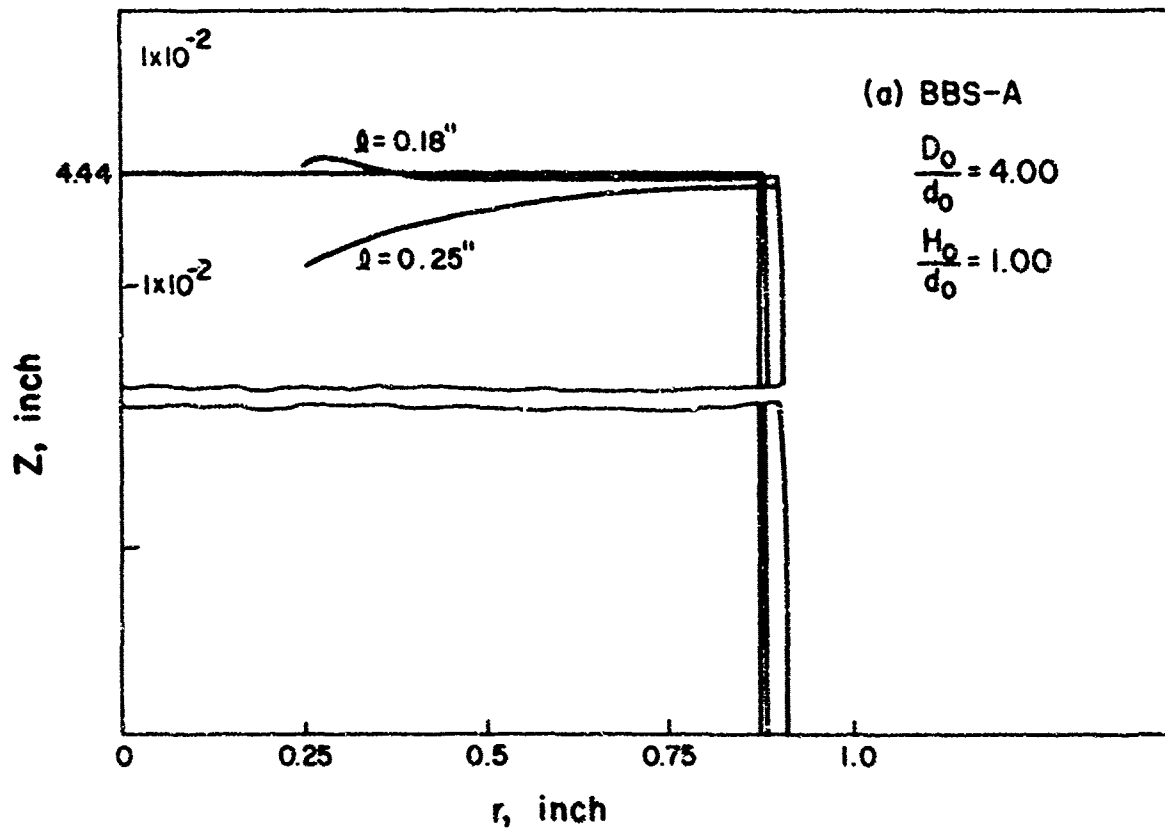


Fig. 20a Surface geometry in hemispherical punch indentation for annealed steel. $H_0/d_0 = 1.00$

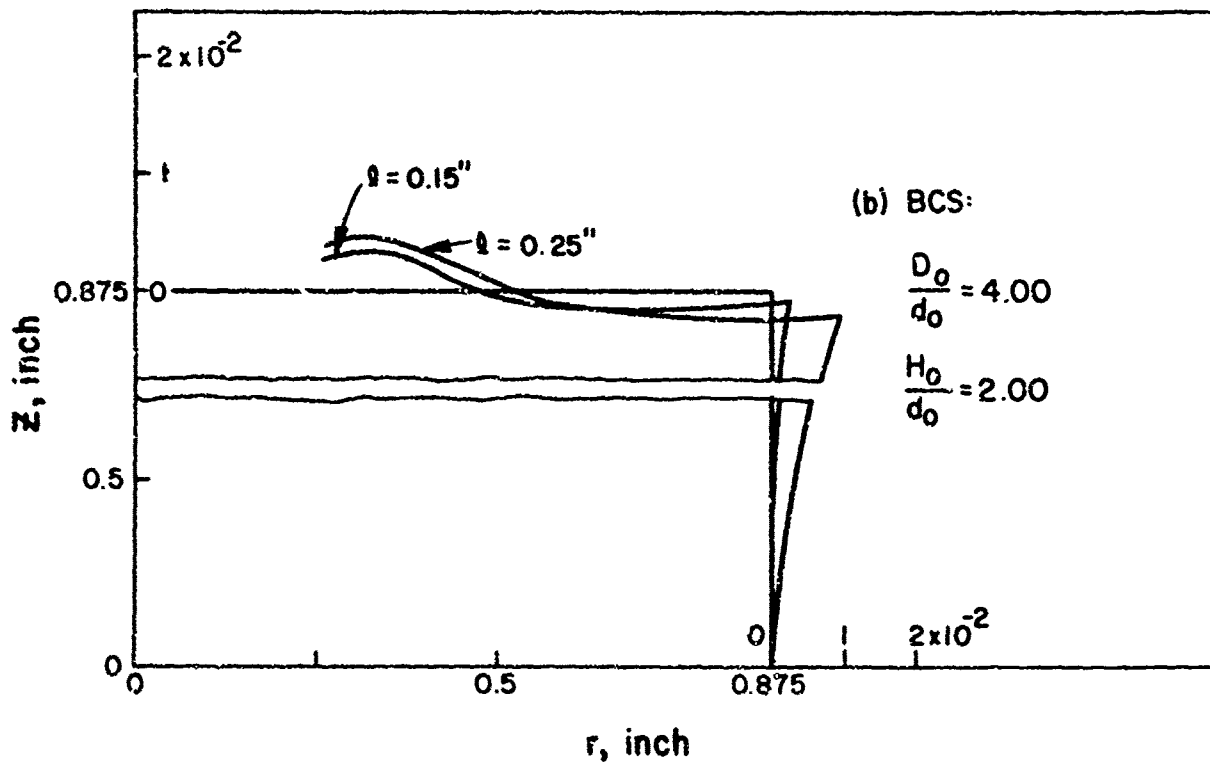


Fig. 20b Surface geometry in hemispherical punch indentation for annealed steel. $H_0/d_0 = 2.00$

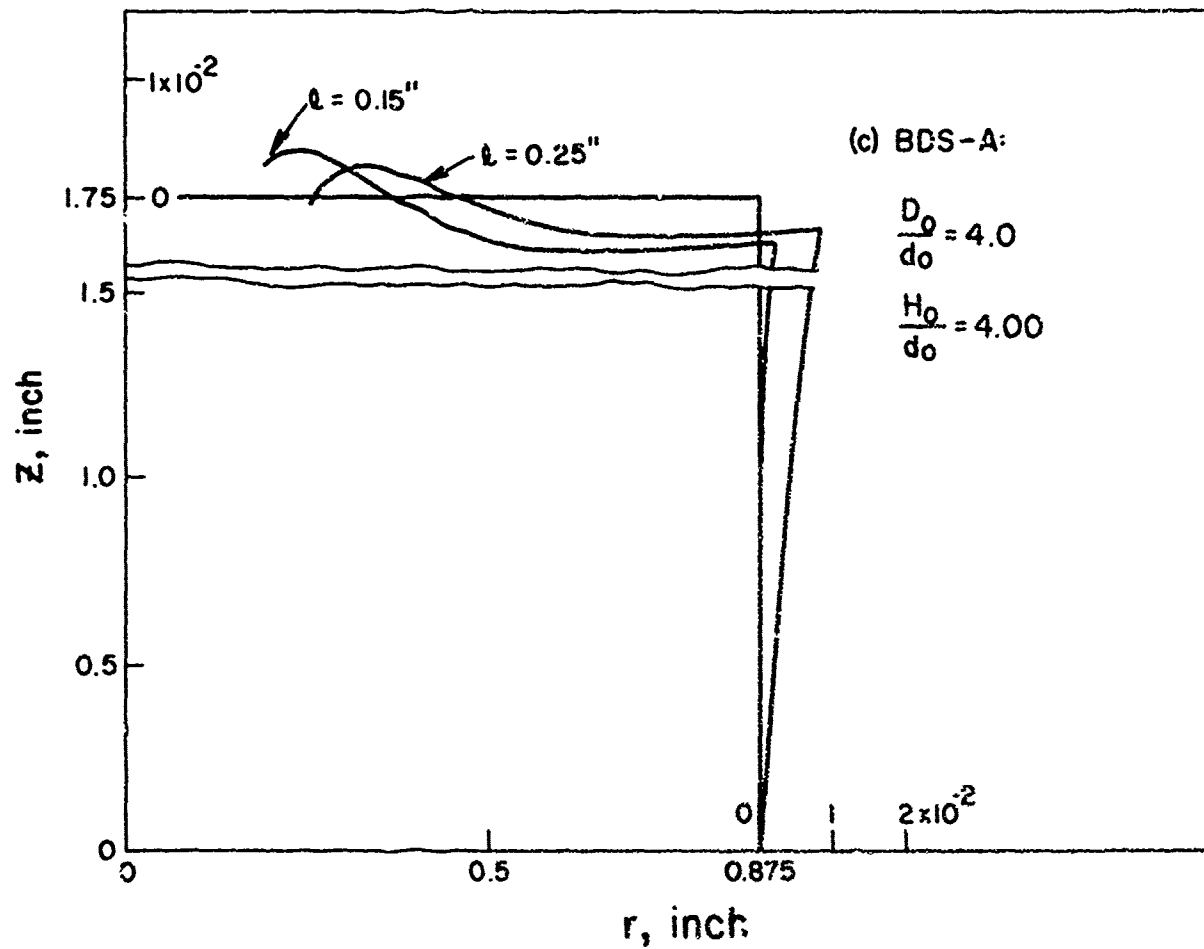
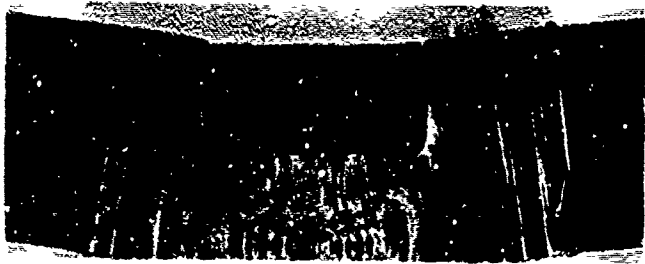


Fig. 20c Surface geometry in hemispherical punch indentation for annealed steel. $H_0/d_0 = 4.00$

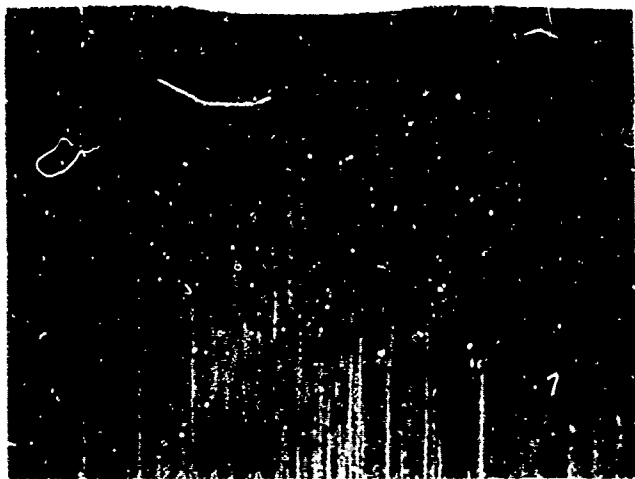


(a) BB
 $l = 0.25$ in

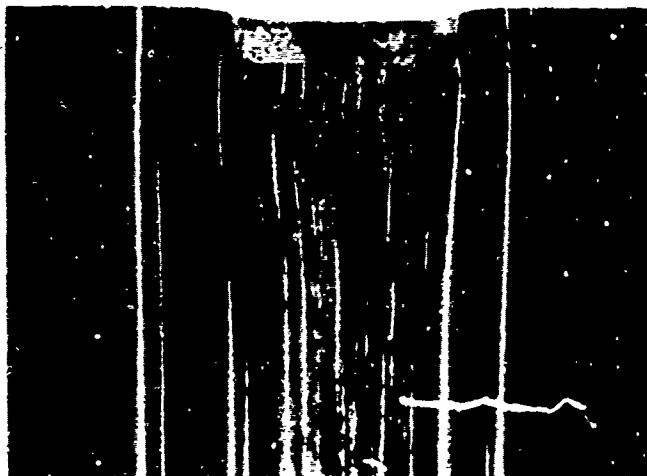


(c) BB-A
 $l = 0.25$ in

Reproduced from
best available copy.



(b) BD
 $l = 0.15$ in



(d) BD-A
 $l = 0.15$ in

Fig. 21 Flow lines for flat punch indentation.

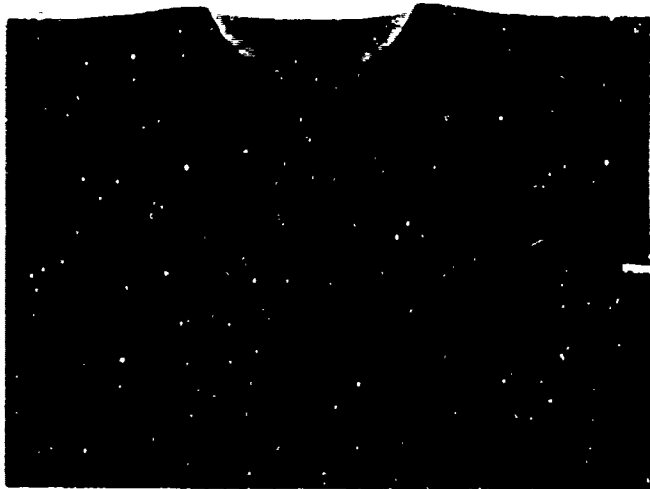


(a) BBS
 $l = 0.25$ in



(c) BBS-A
 $l = 0.25$ in

Reproduced from
best available copy.



(b) BDS
 $l = 0.15$ in



(d) BDS-A
 $l = 0.15$ in

Fig. 22 Flow lines for hemispherical punch indentation.



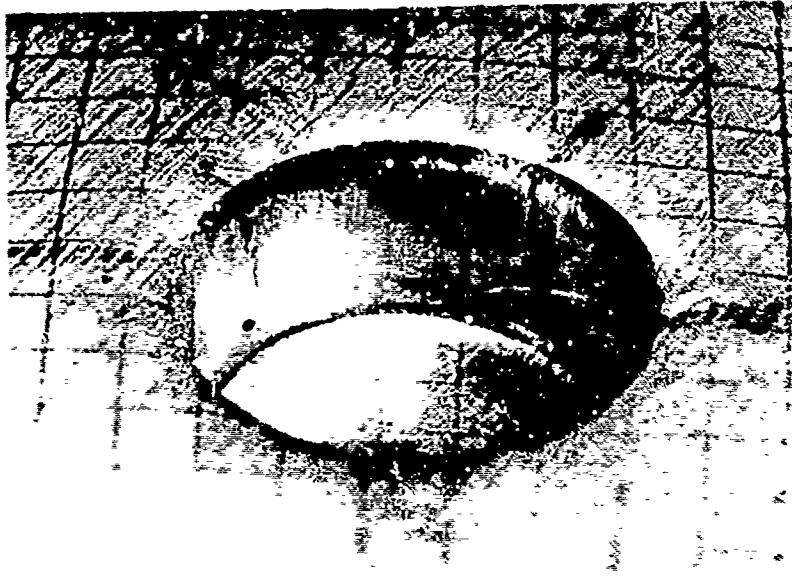
Reproduced from
best available copy.

(a) BBB
 $l = 0.25$



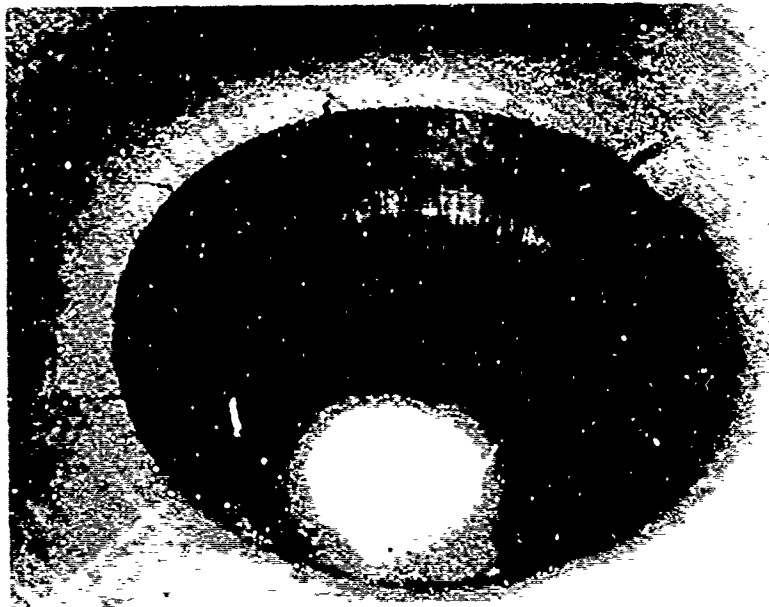
(b) BBS
 $l = 0.25 \text{ in}$

Fig. 23 Localized distortions along the punch surface.



(a) CC: $l = 0.15$ in

Reproduced from
best available copy. 



(a) BDS: $l = 0.25$ in

Fig. 24 The types of cracks occurring in the indentation process.

SECTION II. DEVELOPMENT OF THE MECHANICS OF PLANE STRAIN SIDE-PRESSING OF CIRCULAR CYLINDERS

by

S. Sohrabpour* and Shiro Kobayashi

1. INTRODUCTION

In advanced forging techniques, such as incremental forgings, the problems of compression or indentation of workpieces of complex shapes by dies of various geometries are involved. For a successful forging operation, it is necessary to predict and control the defects occurrences and product qualities. To achieve these ultimate objectives, it is essential to have information on, among other things, the deformation characteristics that occur during the operation. The present investigation deals with the detailed mechanics involved in the side-pressing of cylindrical rods under plane-strain conditions.

The side-pressing of cylindrical rods is one of the important primary metal-working processes, and it has been used in determining the forgeability of materials [1, 2]** A number of investigations on the mechanics of side-pressing of cylindrical rods can be found in the literature [3, 4, 5].

Using the slip-line field technique, Kudo and Nagahama [4] analyzed the upsetting of circular rods under plane-strain conditions. Jain and Kobayashi [5] investigated the deformation and fracture characteristics that occurred during the pressing of cylindrical rods

* Graduate student, Mechanical Design.

**Numbers in brackets refer to the references at end of Part II.

with machined flats of various widths. Despite the fact that the slip-line theory they used in the analysis was based on the assumption of rigid, perfectly plastic materials, it agreed very well with observations of the mean die pressure at the yield point, the load-displacement relationships, the effect of friction at the interface, and the effect of specimen geometry on the deformation characteristics. Jain and Kobayashi pointed out, however, that the critical conditions for defects occurrence can be determined only if accurate information on the local stress and strain distributions are available, taking into account the work-hardening property of the material.

Oxley [6] has shown how the basic equations for the stress variation along the slip lines are modified if the yield stress of the material varies throughout the field. It can be shown in this case, too, that the slip-line field consists of two families of orthogonal curves and they are the characteristics of the governing equations when the distribution of the yield stress is known. Therefore, it is not impossible to construct a slip-line field for work-hardening materials numerically in certain boundary-value problems if the yield stress distribution throughout the field is given. However, simple geometric rules concerning the slip-line field, such as Hencky-Prandtl theorems, are no longer applicable. Furthermore, in most plastic deformation problems, the distribution of yield stress due to work-hardening can be obtained only experimentally by observing the metal flow. Oxley constructed a slip-line field in the machining process from the observed boundary of the plastic zone. The hodograph for this slip-line field was then constructed and compared with the observed velocity distribution. The initial shape of the plastic zone

was adjusted until a more acceptable hodograph was obtained.

Inasmuch as experimental observations of velocities must be made for constructing a slip-line field, these velocities may then be used directly to complete the corresponding slip-line field, thus obtaining a complete solution to the problem. This is the procedure exactly followed in the viscoplasticity method [7-11], which has been used extensively to solve extrusion problems [12, 13, 14]. Usui [15, 16] applied the viscoplasticity technique to the analysis of discontinuous chip formation. He used the equilibrium equations referring to the slip-line directions for deriving the stresses. Using a new technique for observing the flow pattern in chip formation, Childs [17] made a stress analysis based both on the slip-line and principal-stress fields.

In this investigation the detailed mechanics of the side-pressing of circular cylinders under plane-strain conditions were obtained, based on the observed flow patterns of commercially pure aluminum and copper specimens. Slip-line fields and corresponding hodographs were constructed, and a stress calculation was made with the aid of the equilibrium equations referring to the slip-line directions. The effects on the deformation characteristics of friction at the interface, material properties, and initial geometry of the specimens were examined in terms of flow lines and strain and strain-rate distributions.

2. METHOD OF ANALYSIS

The process of side-pressing is a nonsteady-state problem. The plastic zone size and the specimen geometry vary from moment to moment. For rigid, plastic materials with work-hardening the flow stress $\bar{\sigma}$ is

expressed as a function of the effective strain $\bar{\epsilon}$, where $\bar{\epsilon}$ and $\bar{\sigma}$ are defined by

$$\bar{\epsilon} = \int d\bar{\epsilon} = \frac{\sqrt{2}}{3} \int \sqrt{(d\epsilon_1 - d\epsilon_2)^2 + (d\epsilon_2 - d\epsilon_3)^2 + (d\epsilon_3 - d\epsilon_1)^2}$$

and

$$\bar{\sigma} = \sqrt{\frac{1}{2} [(\sigma_1 - \sigma_2)^2 + (\sigma_2 - \sigma_3)^2 + (\sigma_3 - \sigma_1)^2]}$$

with the principal stresses $\sigma_1, \sigma_2, \sigma_3$ and the principal incremental strains $d\epsilon_1, d\epsilon_2, d\epsilon_3$. The effective strain distribution and thus the yield stress distribution also can be obtained at any instant by integrating the incremental effective strain for each element from the beginning of deformation to that instant. This necessitates a continuous observation of flow patterns during the process. At any stage of deformation, the incremental displacement or velocity* distribution can be obtained by the superposition of two consecutive flow patterns having a short time interval. The incremental strain components or strain-rate components are then calculated from the observed displacement field. The known strain-rate components can be used not only for finding the yield stress distribution due to work-hardening, but also for calculating the stresses. This is a principle of the viscoplasticity method. Since the work-hardening characteristics of the material are expressed by $\bar{\sigma} = H(\bar{\epsilon})$, we assume the materials are incompressible, obeying the von Mises yield criterion and its associated flow rule.

With reference to the Cartesian coordinate system x, y, z , the governing equations under plane-strain conditions ($\dot{\epsilon}_z = 0$) are

*Incremental displacement of a point divided by the movement of the die gives a velocity at that point for unit die velocity.

$$\frac{\partial \sigma_x}{\partial x} + \frac{\partial \tau_{xy}}{\partial y} = 0 ; \quad \frac{\partial \tau_{xy}}{\partial x} + \frac{\partial \sigma_y}{\partial y} = 0 \quad (1)$$

$$\sqrt{\frac{3}{4} (\sigma_x - \sigma_y)^2 + 3\tau_{xy}^2} = \bar{\sigma} \quad (2)$$

and

$$\frac{\dot{\epsilon}_x}{\sigma_x - \sigma_m} = \frac{\dot{\epsilon}_y}{\sigma_y - \sigma_m} = \frac{\dot{\gamma}_{xy}}{2\tau_{xy}} \quad (3)$$

where σ_x , σ_y , σ_{xy} are stress components and $\dot{\epsilon}_x$, $\dot{\epsilon}_y$, $\dot{\gamma}_{xy}$ are strain-rate components. Equations (1) and (2) can be solved for three stress components by the method of characteristics, namely, the slip-line method. Since the construction of a slip-line field is extremely difficult, particularly when the yield stress varies throughout a deforming body, the known strain-rate components are used in various ways for the stress analysis. In one method [11], combining Eqs. (2) and (3),

$$\begin{aligned} \dot{\epsilon}_x &= -\dot{\epsilon}_y = \lambda(\sigma_x - \sigma_m) \\ \dot{\gamma}_{xy} &= 2\lambda\tau_{xy} \end{aligned} \quad (4)$$

where

$$\lambda = \frac{3}{2} \frac{\dot{\bar{\sigma}}}{\bar{\sigma}}, \quad \sigma_x = \sigma_z = \frac{1}{2}(\sigma_x + \sigma_y)$$

Equation (4) provides two relationships for three stress components and the third will be one of the two equilibrium equations given in (1). The remaining equilibrium equation can be used partially for substantiating insufficient boundary conditions and also for examining the accuracy of the computed solution.

In the second method [17], the principal stress field is constructed from the strain-rate components according to

$$\tan 2\theta = \frac{\dot{\gamma}}{2\dot{\epsilon}_x} \quad (5)$$

where θ is the angle measured anticlockwise from the x-axis to the σ_1 - axis ($\sigma_1 > \sigma_2$). Then the principal stresses are calculated from the equilibrium equations expressed along the principal stress directions as

$$\begin{aligned} \frac{\partial \sigma_1}{\partial s_1} + (\sigma_1 - \sigma_2) \frac{\partial \theta}{\partial s_2} &= 0 \\ \frac{\partial \sigma_2}{\partial s_2} + (\sigma_1 - \sigma_2) \frac{\partial \theta}{\partial s_1} &= 0 \end{aligned} \quad (6)$$

The overall accuracy of the field construction and stress computation is examined with the aid of the yield condition.

The third method consists in performing the stress calculation, based on the equilibrium equation along the slip-lines, the fields of which can be constructed from the known strain-rate distribution [6, 15]. The equilibrium equations along the slip-lines become

$$\begin{aligned} \frac{\partial \sigma}{\partial s_\alpha} - 2k \frac{\partial \varphi}{\partial s_\alpha} + \frac{\partial k}{\partial s_\beta} &= 0 \quad \text{along } \alpha\text{-line} \\ \frac{\partial \sigma}{\partial s_\beta} + 2k \frac{\partial \varphi}{\partial s_\beta} + \frac{\partial k}{\partial s_\alpha} &= 0 \quad \text{along } \beta\text{-line} \end{aligned} \quad (7)$$

where σ and k are the normal and shear stresses along the slip-line respectively, and s_α and s_β are the distances along the slip lines of each family. The two families of slip-lines α and β are distinguished in such a way that if they are regarded as a pair of right-handed curvilinear axes, the line of action of the algebraically greatest principal stress falls in the first and third quadrant [18]. The angle φ is the anticlockwise angular rotation of the α -line from the x-axis. In

Eq. (7), the shear stress k is given by $k = \bar{\sigma}/\sqrt{3}$ according to the yield condition, and its distribution is known throughout a deforming body. The accuracy of the computation as well as the construction of the slip-line field can be checked by the fact that the stress value at a point is independent of the integration paths, or by an examination of the orthogonality relation between the slip-line field and the hodograph. This orthogonality condition should hold for work-hardening materials also, so long as the materials are assumed to be incompressible

In the present investigation the slip-line method was used for the stress analysis. Integrating Eq. (7), we obtain

$$\begin{aligned} \sigma - 2 \int k \frac{\partial \varphi}{\partial s_{\alpha}} ds_{\alpha} + \int \frac{\partial k}{\partial s_{\beta}} ds_{\alpha} &= \text{const.} \\ &\text{along } \alpha\text{-lines} \end{aligned} \quad (8)$$

$$\sigma + 2 \int k \frac{\partial \varphi}{\partial s_{\beta}} ds_{\beta} + \int \frac{\partial k}{\partial s_{\alpha}} ds_{\beta} = \text{const.}$$

along β -lines

Equation (8) is the basis for determining the stress field from the slip-line field. Once the value of σ is known, the stress components can be deduced from the relationships given by

$$\begin{aligned} \sigma_x &= \sigma - k \sin 2\varphi, \quad \tau_{xy} = k \cos 2\varphi \\ \sigma_y &= \sigma + k \sin 2\varphi \end{aligned} \quad (9)$$

3. EXPERIMENTS AND CALCULATION PROCEDURES

The experiments consisted of side-pressing at room temperature, cylindrical rods of commercially pure aluminum and copper, having machined flats of various widths. Observations of grid distortions were made and the load-displacement curves were recorded for

various specimen geometries with smooth and rough dies.

Circular cylinders 1 in. in diameter ($2R_0$) and 1 in. long were prepared from aluminum 1100-F and commercially pure hard copper, and parallel flats of various widths were machined to give the following initial geometry:

Width of Flat	$2W_0$ in.	0.125	0.452	0.606	0.722
Height	$2H_0$ in.	0.992	0.892	0.792	0.692

The stress-strain curves of the two materials are given in Fig. 1.

Two interface friction conditions were used in the tests. Low friction was achieved by using smooth dies lapped to an 8 μ in. surface finish and by applying Fluorocarbon spray lubricant. For high friction, rough dies having machined serrations 900 μ in. deep were used, and the specimens and die surfaces were cleaned with ethylene dichloride and dried before each test.

The experimental setup is shown in Fig. 2. The experiments were performed with an apparatus for plane-strain side-pressing placed on a 160,000-lb. Tinius Olson testing machine with a speed of 0.05 in/min. This apparatus was also used for a previous study on the fracturing of a high strength aluminum alloy during side-pressing [19]. The displacement of the die was measured with a deflectometer, and the load-displacement curves were obtained on a recorder attached to the testing machine. A Nikon camera was mounted in front of the side-pressing apparatus for photographing the grid patterns behind a glass plate.

Grid-lines with 0.050 in. spacing were printed on one end surface of the specimen, using the Kodak Photo-Resist method. The copper specimens were coated with tin before grid-printing to give a better

contrast in the photographs. A series of photographs of the grid patterns was taken at an interval of 0.020 in. of die displacement. The grid distortions were traced by a scanning machine at the Lawrence Radiation Laboratory, and the current coordinates of each grid point in these patterns were punched on IBM cards. These coordinates constitute the input data for the analysis.

The analysis begins with a calculation of the strain-rate field from the coordinates of the grid points [20]. With reference to Fig. 3, the grid pattern shown by solid lines distorts to that given by dashed lines after a time increment Δt . The deformed grid pattern is translated so that the points $(0, 0)$ and $(0, 0)'$ coincide. The strain-rate components can then be calculated by

$$\begin{aligned}(\dot{\epsilon}_x)_{00} &= \frac{1}{2\Delta t} \left(\frac{x'_{10} - x_{10}}{x_{10}} + \frac{x'_{10} - x_{10}}{x_{10}} \right) \\(\dot{\epsilon}_y)_{00} &= \frac{1}{2\Delta t} \left(\frac{y'_{01} - y_{01}}{y_{01}} + \frac{y'_{01} - y_{01}}{y_{01}} \right) \\(\dot{\gamma}_{xy})_{00} &= \frac{1}{2\Delta t} \left[\left(\frac{x'_{01} - x_{01}}{y_{01}} + \frac{y'_{10} - y_{10}}{x_{10}} \right) + \left(\frac{x'_{01} - x_{01}}{y_{01}} + \frac{y'_{10} - y_{10}}{x_{10}} \right) \right]\end{aligned}$$

where $(x_{10}, y_{10}), \dots$ are the x- and y-coordinates of the points $(1, 0), \dots$, and the prime indicates the coordinates after the incremental deformation. Calculated values of $\dot{\epsilon}_x$ and $\dot{\epsilon}_y$ generally satisfied the incompressibility, namely, $\dot{\epsilon}_x = -\dot{\epsilon}_y$, with negligible error. The effective strain rate is obtained from the strain-rate components, based on the relationship given by $\dot{\epsilon} = \frac{1}{\sqrt{3}} \sqrt{4\dot{\epsilon}_x^2 + \dot{\gamma}_{xy}^2}$ for plane-strain.

In order to construct the slip-line field, the maximum shear strain-rate directions were determined within the deforming region according to

$$\tan 2\varphi = \frac{2\dot{\epsilon}_y}{\dot{\gamma}_{xy}} = - \frac{2\dot{\epsilon}_x}{\dot{\gamma}_{xy}} .$$

The foregoing calculations were made by a computer. The slip-lines were found graphically after the maximum shear strain-rate directions were obtained. The hodograph was derived from the measured incremental displacement field and compared with the slip-line field to examine the orthogonality between them. The slip-line field was then adjusted until the orthogonality relationship was satisfied. After the slip-line field was constructed, the distribution of the yield stress was obtained along the slip-lines by a linear interpolation. The calculation of stresses along the slip-lines is possible using Eq. (8). Integration starts from a point on the free surface that is definitely in a plastic state. Calculation of the yield stress distribution and subsequent stress calculations were again made with a computer.

Observations of the flow patterns and calculations of the strain and strain-rate were made for all the tests. The construction of the slip-line field and the stress analysis, however, were performed only for the side-pressing of circular cylinders of copper specimens with smooth dies. Although the load-displacement curves were recorded, the results are not shown here because the general behavior of load-displacement characteristics involved in side-pressing has been discussed elsewhere [19].

4. DETAILED MECHANICS OF SIDE-PRESSING CIRCULAR CYLINDERS OF COPPER

Examples of grid patterns at various reductions in height for smooth and rough dies are shown in Fig. 4. The darker area of the specimen seen in the figure is the zone where deformation occurred

against the glass plate in the direction of plane-strain constraint. The width-height ratio (W/H) is a decisive factor in side-pressing deformation, and this ratio varies during compression. The W/H ratio values obtained from Fig. 4 are as follows:

Reduction in Height (%)	10	20	30	40
Smooth Die	0.415	0.769	1.210	1.770
Rough Die	0.419	0.750	1.198	1.756

It is observed in Fig. 4 that the plastic deformation zone spreads through the workpiece material between the dies, leaving a part of the workpiece at both sides undeformed. The boundary between these two regions can be visualized by superposing the distorted grid pattern over the original grid lines. Figure 5 shows an example of these boundaries. The deformation zone has, in general, a shape similar to the one assumed in the slip-line field for perfectly plastic material, but is larger in size, because in work-hardening materials the localized deformation zone diffuses to a finite zone. Flow lines shown in Fig. 6 were obtained by following the displacement path of each grid point. Flow lines for rough and smooth dies are compared during deformations up to a 40 percent reduction in height. A close examination of Fig. 6 reveals that a minor difference exists in the flow line directions for rough and smooth dies at the beginning of deformation, but the difference in the flow direction as well as in the total distance of point movement becomes more pronounced as the deformation continues. It can be recalled that for the indentation

problem, the slip-line theory for rigid, perfectly plastic materials predicts the presence of a rigid zone beneath the die and thus the occurrence of identical deformation for all friction conditions at the interface when the width-height ratio is equal to or less than unity. Experiments [5] indicated that the actual material's behavior was in agreement with the predictions in terms of load-displacement curves. Therefore, the flow lines for rough and smooth dies would be expected to be the same for 10 and 20 percent reductions in height where the width-height ratio is smaller than 1, but they would be expected to deviate from each other for larger deformations since the width-height ratio increases and exceeds unity with increasing deformation.

Figure 7 gives the measurements of the relative sliding displacement (Δu) of the deforming material during a small die displacement (ΔU), and these measurements suggest the presence of a rigid body near the die-workpiece interface at the beginning of deformation. For real situations, however, the rigid body assumption is only approximate. The effect on the overall deformation of friction conditions at the interface is also shown by calculating the strain distributions within the deforming body. Figure 8 shows the strain distributions along the horizontal axis of symmetry (x-axis) at various stages of deformation for the two friction conditions. The strain ϵ_x is large and tensile at the center of the specimen but decreases toward the free surface. It is of interest to note that the strain distributions for rough and smooth dies are almost the same for 10 and 20 percent reductions in height, but they differ considerably for larger deformations. The strain levels corresponding to homogeneous deformation are given for reference.

The strain distributions along the vertical axis of symmetry (y-axis) are shown in Fig. 9. Again, a large, tensile strain was found at the center of the specimen, decreasing toward the die. It is evident that a region of small deformation exists beneath the die, except when a reduction is 40 percent with a smooth die, and that the deviation of the strain distributions for the two friction conditions is confirmed for width-height ratios larger than unity. The detailed deformation characteristics can be represented by the distribution of the effective strain. This is shown in Fig. 10 for various stages of deformation. A comparison of effective strain distributions for smooth and rough dies is also shown. At a 10 percent reduction in height (Fig. 10a), the largest strain was found along the vertical axis of symmetry at some distance from the die-workpiece interface. The location of the largest effective strain moves to the center of the specimen when the reduction in height is 20 percent (Fig. 10b). Also at this reduction, the region of large strain appears near the edge of the contact surface. It is observed, too, that the difference in the degree of deformation for the two friction conditions at these reductions is minor. At a larger deformation (Fig. 10c) the trend of the distributions is similar for rough and smooth dies, but there is some difference in the magnitudes. Finally, at a reduction of 40 percent (Fig. 10d), an appreciable difference is apparent not only in the magnitude of the effective strain, but also in the form of the distribution. The largest strain remains at the center of the specimen, suggesting that this area may be a critical location for defects occurrence in this process.

Since the stress system also is a critical factor for fracturing, we now examine the stress distributions. For stress analysis, the slip-line fields were determined from the maximum shear strain-rate directions at each grid point, and then modified, using a hodograph constructed from the incremental displacement distributions obtained experimentally. The slip-line fields and corresponding hodographs are shown in Fig. 11 for smooth dies at various reductions. The letters and numbers indicate the corresponding points in the slip-line field and the hodograph. The slip-line fields obtained from the experimental velocity fields are seen to differ appreciably from those found for perfectly plastic materials in the transition region from the deforming zone to the rigid zone. Shabaik [2] examined the flow field in the plane-strain compression of a slab and reached a similar conclusion, which led him to propose a new slip-line solution to the problem.

Using Eq. (8), the stresses were calculated from the slip-line fields shown in Fig. 11. Figures 12 and 13 show the σ_x and σ_y distributions along the x-axis. The stresses are normalized by dividing by $Y'_0 = \frac{2}{\sqrt{3}} Y_0$, where Y_0 is the initial yield stress of the material. In Fig. 12, the stress σ_x is tensile, then decreases as the deformation continues, and becomes compressive near the center. This change of the stress distribution is caused by a spread of the plastic deformation zone sideways with the increasing width-height ratio. The stress is always compressive with the largest magnitude at the center, and its magnitude increases with the increased deformation. The stress distributions along the y-axis are given in Figs. 14 and 15. The distributions calculated from slip-line fields for rigid, perfectly plastic materials are also shown at 10 and 20 percent reductions for comparison.

The stress σ_x shown in Fig. 14 is compressive near the die surface and becomes tensile toward the center of the specimen at a 10 percent reduction, but the distributions at larger reductions indicate an opposite trend. Also, the stress distribution at a 10 percent reduction agrees well in magnitude and trend with that obtained for perfectly plastic materials, but no correlation exists between them at a 20 percent reduction. Similar results are obtained for the stress distribution of σ_y in Fig. 15. Comparing the stress σ_y at 10 percent and at larger reductions, again the opposite trend is seen in its distributions, and the distribution at a 20 percent reduction apparently shows no similarity with that for perfectly plastic materials. A comparison of the stress distributions for work-hardening materials and for perfectly plastic materials shown in Figs. 14 and 15 indeed confirms the remarks made with regard to the slip-line fields in Fig. 11.

In Fig. 16, the distribution of σ_z , which is equal to the hydrostatic component $\frac{1}{2}(\sigma_x + \sigma_y)$ for plane strain, is shown throughout the deforming region. At a 10 percent reduction (Fig. 16a), there is a large amount of hydrostatic pressure near the die, and a hydrostatic tension region is observed near the center of the specimen. When the reduction is 20 percent, the region of large hydrostatic pressure moves toward the center of the specimen and, in addition, a large pressure zone appears near the edge of the contact surface (Fig. 16b). The pressures at these two regions increase as the reduction increases (Fig. 16c), but become somewhat relaxed at a reduction of 40 percent. The distributions of σ_z shown in Fig. 16 are directly responsible for the small deformation against the glass plate in the direction of plane-strain constraint discussed with reference to Fig. 4.

The contact pressure distribution along the die-workpiece interface is plotted in Fig. 17. The pressure increases from the center toward the edge for 10, 20, and 30 percent reductions, and the distribution curve flattens at 40 percent reductions. The side-pressing loads calculated from the contact pressures agreed within 10 percent with those measured. The average pressure is higher at a 10 percent reduction and remains approximately the same at other reductions. This is due to the value of the width-height ratio, and is in agreement qualitatively with the slip-line theory prediction for perfectly plastic materials.

It was shown that the center of the specimen was a critical location for fracturing because the effective strain was found to be largest at that point. The stress system and its variation during deformation at this point was therefore examined (Fig. 18). In the beginning of deformation σ_x is tensile and it increases as the deformation proceeds. Then at a width-height ratio of about 0.5 the stress σ_x tends to decrease rapidly, resulting in a state of increased hydrostatic pressure. With further deformation, the pressure rises gradually. It is a well-known fact that the ductility of the material increases generally under the compressive stresses. Thus, the center of the specimen may not become a critical point for fracturing if the width-height ratio is sufficiently large.

5. EFFECTS OF SPECIMEN GEOMETRY AND MATERIAL PROPERTIES

For examining the effect of initial specimen geometry, specimens with machined flats of various widths were side-pressed, and the strain and strain-rate distributions were compared. Figures 19 and 20 show

the constant effective strain-rate contours at configurations given by $W/H = 1.22$ and 1.80 , respectively, for specimens having initial flats of different widths. The values of the strain rates in the figures are for the unit die velocity. It is a common occurrence for a zone of relatively high strain rate to run diagonally from the corner of the die-workpiece contact surface toward the center of the specimen, as seen in Fig. 19. The distribution patterns, however, show minor differences. Since measurements of the sliding velocity distributions along the interface show no difference for three specimens, the differences in strain-rate patterns are attributed to the variation in the yield stress distributions. In comparing the magnitudes of strain rates, it must be pointed out that the actual sizes of the three specimens at the same values of width-height ratio differ, and that the strain-rate values should be adjusted according to geometrical similarity, though this adjustment is small in the present case. For a width-height ratio of 1.80 , Fig. 20 reveals that the high-strain-rate region exists from a corner of the contact surface in a direction roughly 45 degrees to the contact surface. Furthermore, another high-strain-rate zone appears at the center of the specimen just beneath the die. In this case, too, the friction condition along the die-workpiece interface is almost identical for the three specimens. With this width-height ratio, the strain-rate distributions are in good agreement with each other despite the fact that variations in the yield stress distributions still exist. When the width-height ratio is considerably larger than unity, the interface friction and the current geometrical configuration (W/H) appear to be controlling factors for determining instantaneous flow patterns. Figure 21 gives the total

strain distributions along the x-axis at the configurations shown in Figs. 19 and 20. The magnitudes of the strains should obviously be different. A larger deformation has to take place in a specimen with a narrower machined flat to arrive at the same value of width-height ratio. During the deformation, until W/H reaches 1.22, the location of the largest strain rate along the x-axis remains at the center of the specimen, resulting in the largest strain occurring there also, then decreasing toward the free surface. On the other hand, with an increasing W/H value, the point of the largest strain rate moves away from the center of the specimen. Thus the larger strains occur at some distance from the center. Figure 22 shows the strain distributions along the y-axis. Again, the strain is largest at the center of the specimen, and decreases toward the die-workpiece interface at $W/H = 1.22$, while the increase of the strain near the interface is much larger than that at the center at $W/H = 1.80$. This is due to the appearance of the relatively high strain-rate region near the interface along the y-axis. Thus, the results shown in Figs. 21 and 22 are consistent with the observations made in Figs. 19 and 20. Since the strain variation at the center of the specimen appears to reflect sensitively the change of deformation pattern, the effective strains $\bar{\epsilon}$ at the center of the specimen were plotted in Fig. 23 as functions of the width-height ratio for specimens with various initial flats. The curves with smooth dies are characterized by a rapid increase until W/H becomes unity, followed by a sharp decrease in slope, and then another increase in slope at about $W/H = 2.0$. With rough dies, the strain follows the same path as that for smooth dies and begins to deviate around a width-height ratio value of 1.0. It is concluded then that the deformation

is determined by the current geometry alone for $W/H < 1.0$, and the friction condition and width-height ratio control the deformation mode when W/H becomes larger than unity. These conclusions indeed coincide with those predicted by the slip-line theory for rigid, perfectly plastic materials. It may be of interest to examine further the effect of material properties on metal flow. The flow lines in side-pressing circular cylinders of aluminum and copper are compared in Fig. 24 for a reduction in height of up to 22 percent. Since in this range of reduction the width-height ratio is less than unity, the effect of friction on deformation should be negligible. Therefore, any deviation in flow lines in this range may be considered as the effect of material properties. As seen in the figure some differences are indicated, but they are insignificant. This is confirmed again by the effective strain variation at the center of the specimen shown in Fig. 25 for the two materials. Investigation of the effect of material properties was limited, mainly because the two materials selected had similar stress-strain curves with only a difference in magnitude, and it was therefore not possible to draw a general conclusion. However, it can be speculated that, in general, the material properties would not cause a significant change of the deformation characteristics in this process. This hypothesis is based on the argument that a large part of the free surface remains in the elastic state; therefore, the frictional and geometrical constraints dominate the determination of plastic flow involved in side-pressing.

6. SUMMARY

The flow patterns of commercially pure aluminum and copper specimens were observed in side-pressing under plane-strain conditions.

The detailed mechanics were derived for side-pressing circular cylinders, and the effects on the deformation characteristics of friction at the interface and initial specimen geometry were examined. The slip-line theory, based on the assumption of rigid, perfectly plastic materials agreed well with the observations of overall deformation characteristics. The detailed mechanics for actual materials, however, differed considerably from those predicted by the theory for idealized materials. The local stress, strain, and strain-rate distributions were revealed, and stress and strain paths at the center of the specimen were examined. The effects of initial specimen geometry and material properties were also studied. It was shown that the current geometry and the friction conditions determined the deformation mode, and practically no difference existed in flow fields for the two materials selected for this investigation.

7. REFERENCES

- [1] A. L. Hoffmann, Workability Testing Techniques, Technical Report AFML-TR-69-174, June 1969.
- [2] R. J. Quigg, "Effect of Phase Changes on the Workability and Mechanical Properties of Udimet 700," High Temperature Materials II, (G. M. Ault, W. F. Barday, and H. P. Munger, eds.), Interscience. N. Y., 1965, p. 245.
- [3] E. P. Unksov, An Engineering Theory of Plasticity, Butterworths, London, 1961.
- [4] H. Kudo and T. Nagahama, "Analysis of Working Pressure, Material Spread and Fracturing--Study in Transverse Upsetting Process of Circular Rod, 2nd Report," J. Japan Soc. Technol. Plasticity, vol. 10(106), 1969, p. 837.
- [5] S. C. Jain and Shiro Kobayashi, "Deformation and Fracture of an Aluminum Alloy in Plane-Strain Side-Pressing," Proceedings of the 11th International Conference of Machine Tool Design and Research Conference, Birmingham, England, Sept. 1970.
- [6] P. L. B. Oxley, "A Photographic Investigation of the Metal Cutting Process," Ph.D. thesis for University of Leeds, England, 1957.
- [7] E. G. Thomsen and J. T. Lapsley, Jr., "Experimental Stress Determination within a Metal during Plastic Flow," Proceedings of the American Society of Experimental Stress Analysis, vol. 11, 1954, pp. 59-68.
- [8] E. G. Thomsen, C. T. Yang, and J. B. Bierbower, "An Experimental Investigation of the Mechanics of Plastic Deformation of Metals," University of California Press, Berkeley, 1954.
- [9] E. G. Thomsen and J. Frisch, "Stresses and Strains in Cold Extrusion of 250 Aluminum," Trans ASME, vol. 77, 1955, p. 1344.
- [10] E. G. Thomsen, "Visioplasticity," CIRP Annalen, vol. 12, 1963-64, p. 127.
- [11] E. G. Thomsen, C. T. Yang, and Shiro Kobayashi, Mechanics of Plastic Deformation in Metal Processing, Macmillan, 1964.
- [12] A. H. Shabaik and E. G. Thomsen, "Investigation of the Application of Visioplasticity Methods of Analysis to Metal Deformation Processes," Final Report prepared for the Navy, Bureau of Naval Weapons, Feb. 1967.
- [13] A. H. Shabaik and E. G. Thomsen, "Investigation of the Application of Visioplasticity Methods of Analysis to Metal Deformation Processes," Final Report prepared for the Navy, Bureau of Naval Weapons, Feb. 1968.

- [14] H. S. Mehta, A. H. Shabaik, and Shiro Kobayashi, "Analysis of Tube Extrusion," Trans. ASME, Journal of Engineering for Industry, vol. 92, 1970, pp. 403-411.
- [15] E. Usui, "Plasticity Analysis of Discontinuous Chip Formation (Part 1) - Experimental Techniques and Method of Analysis," Seimitsu-Kikai, vol. 32, No. 12, 1966, pp. 812-819 (in Japanese).
- [16] E. Usui, "Plasticity Analysis of Discontinuous Chip Formation (Part 2) - Deformation Mode, Slip-Line Field and Hodograph," Seimitsu-Kikai, vol. 33, No. 2, 1967, pp. 77-85 (in Japanese).
- [17] T. H. C. Childs, "A New Experimental Technique for Observing Chip Deformation," Proceedings of the 11th International Machine Tool Design and Research Conference, Birmingham, England, Sept. 1970.
- [18] K. Hill, The Mathematical Theory of Plasticity, Oxford, Clarendon Press, 1950.
- [19] Shiro Kobayashi, C. H. Lee, Y. Saida, and S. C. Jain, "Analytical Prediction of Defects Occurrence in Simple and Complex Forgings," Technical Report AFML-TR-70-90, Air Force Materials Laboratory, Wright-Patterson Air Force Base, Ohio, July 1970.
- [20] Y. Yamada, Sosei Rikigaku, Nikkan Kogyo Shinbun, Tokyo, 1965 (in Japanese).
- [21] A. H. Shabaik, "Prediction of the Geometry Changes of the Free Boundary during Upsetting by the Slip-Line Theory," presented at the ASME Winter Annual Meeting, New York, Dec. 1970.

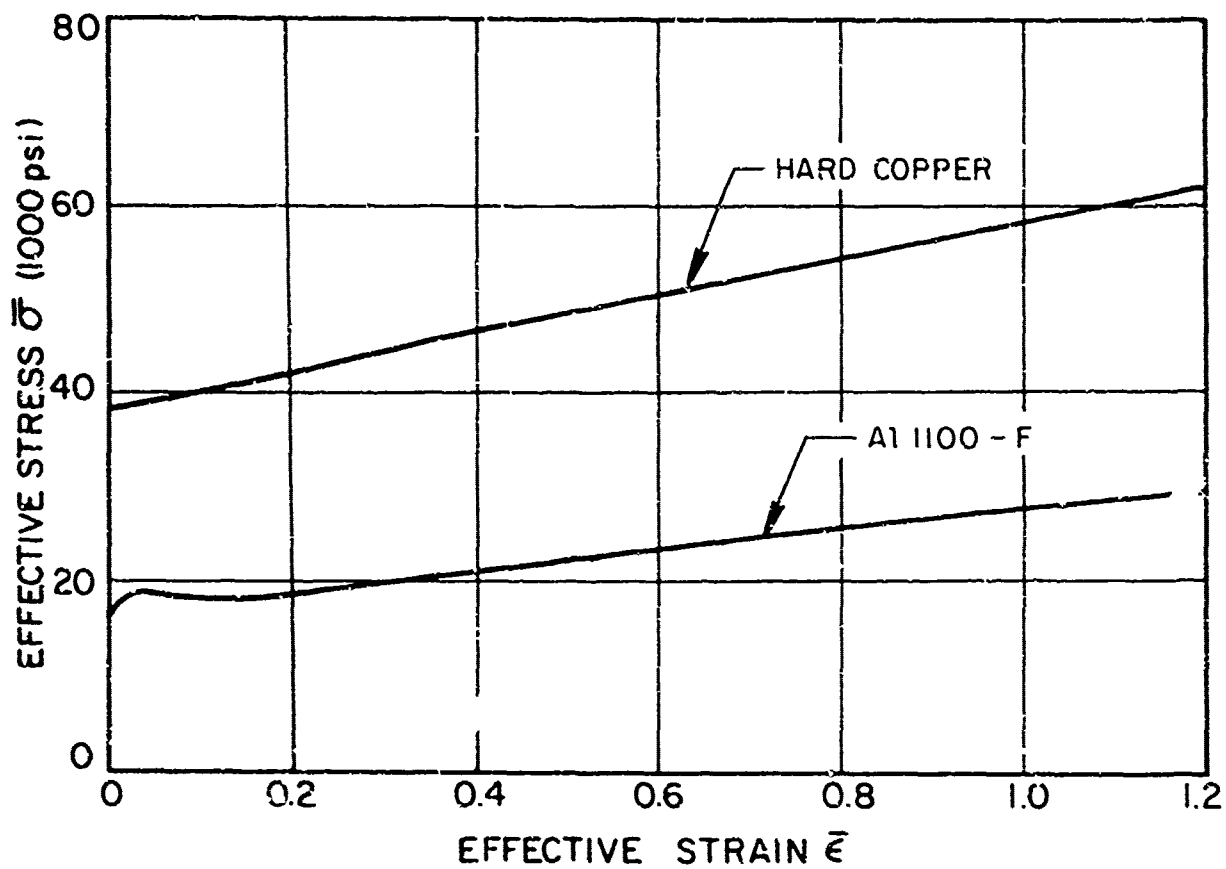


Fig. 1 Stress-strain curves of aluminum 1100-F and commercially pure hard copper.

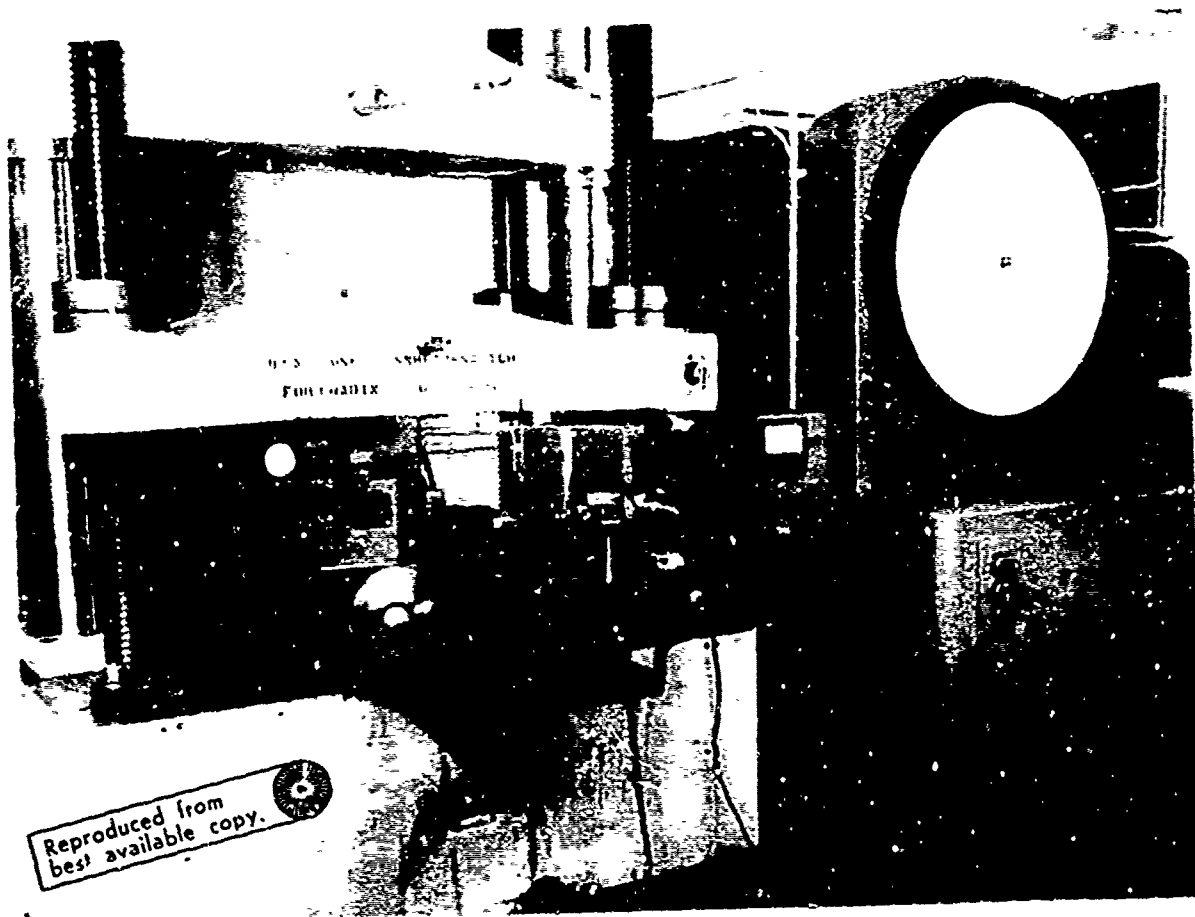


Fig. 2 Experimental setup for one-strain side-pressing.

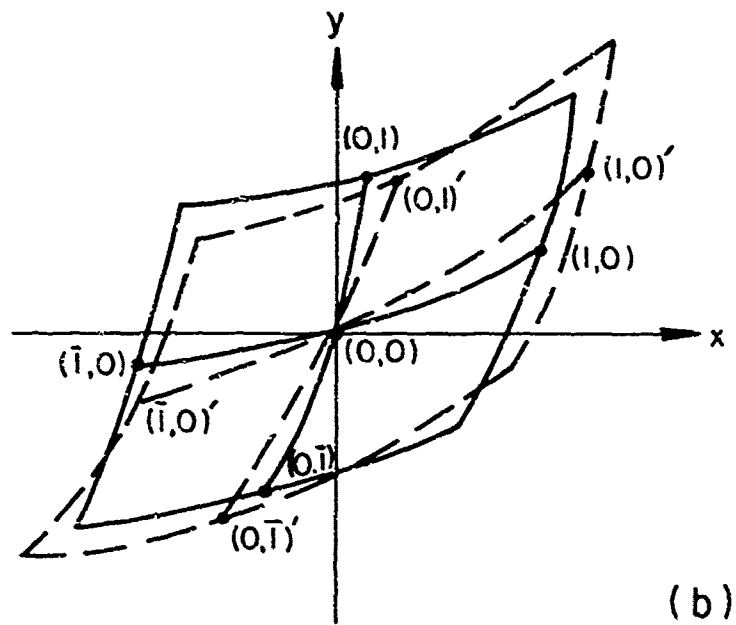
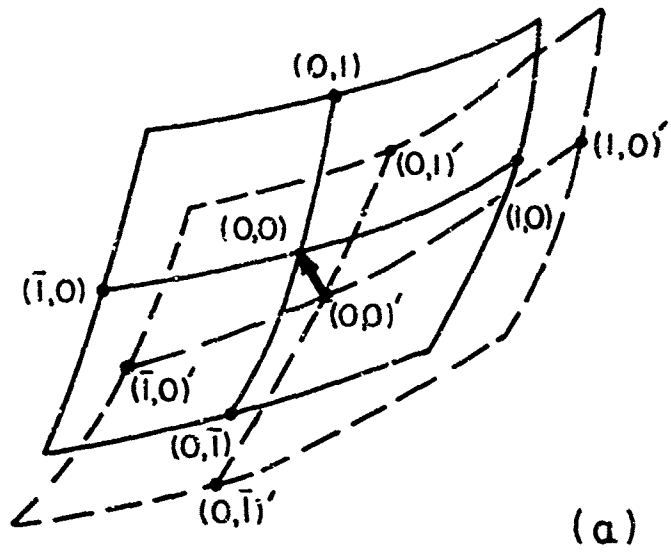


FIG. 3 Grid-distortions for the calculation of incremental strains.

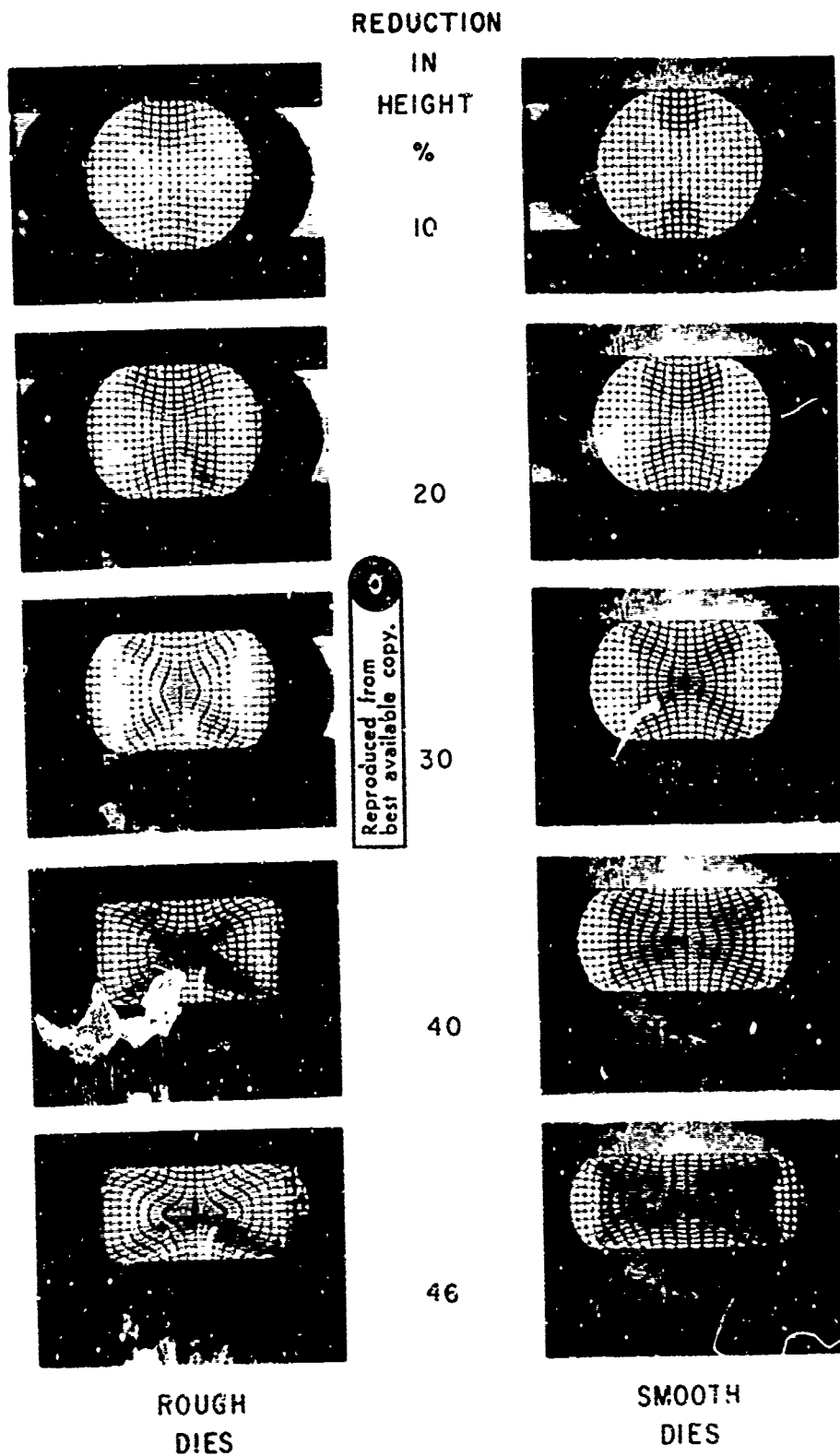
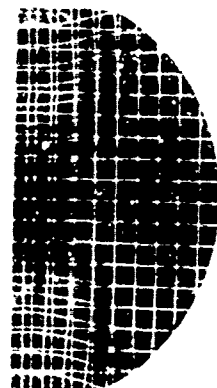
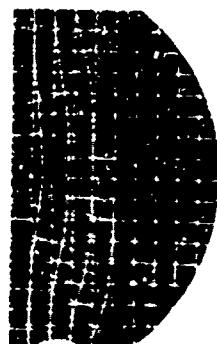


Fig. 4 Grid patterns in side-pressing of circular cylinders of copper at various stages of deformation.



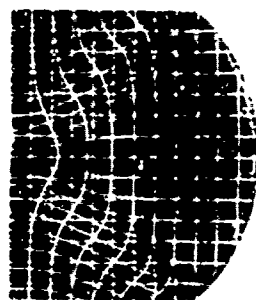
REDUCTION
IN
HEIGHT
(PERCENT)

10%



20%

Reproduced from
best available copy.



30%

Fig. 5 Boundaries of the plastically deforming zone: copper specimen, smooth dies.

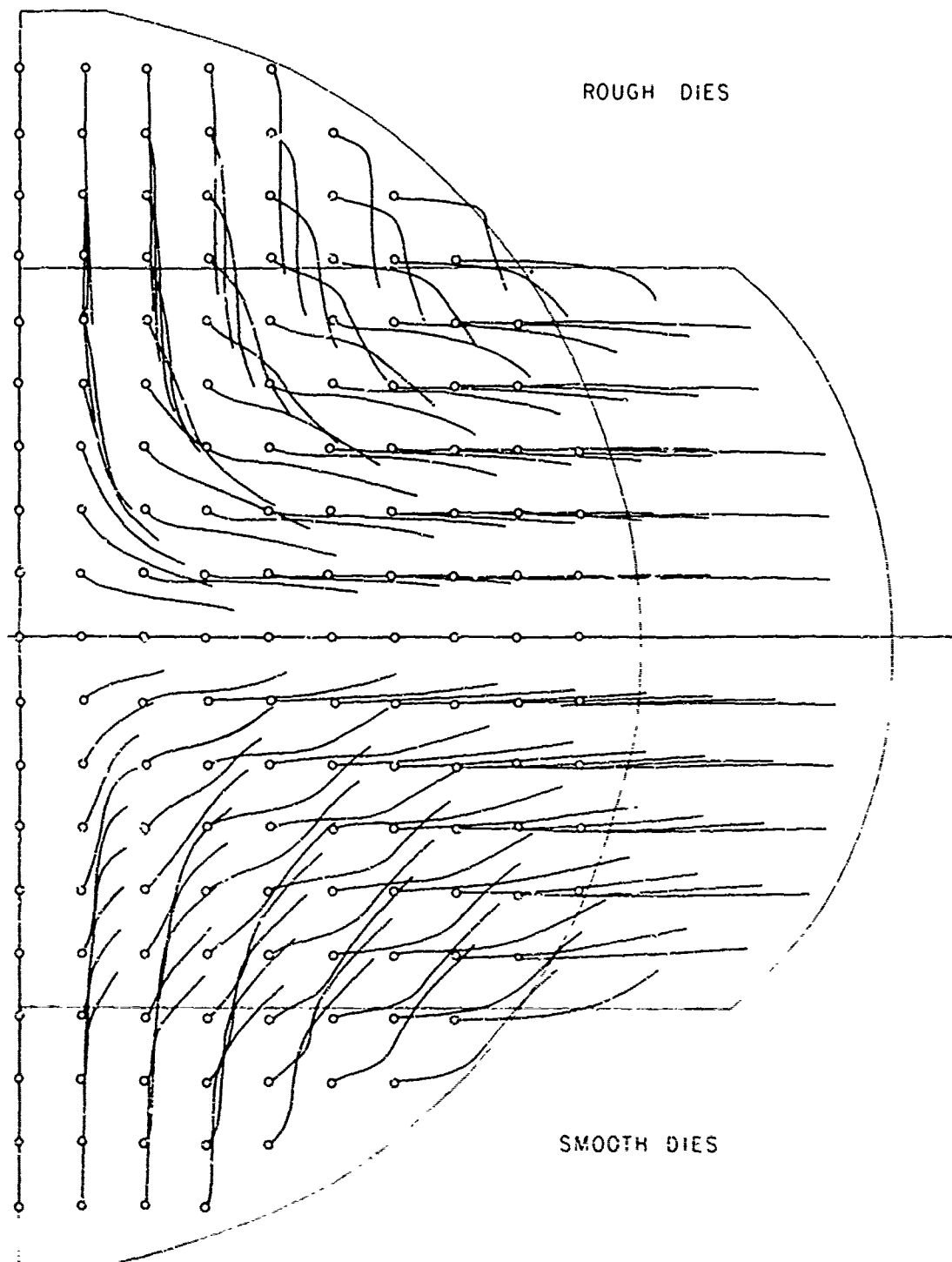


Fig. 6 Comparison of flow lines in pressing at reductions in height up to 10 percent with smooth and rough dies.

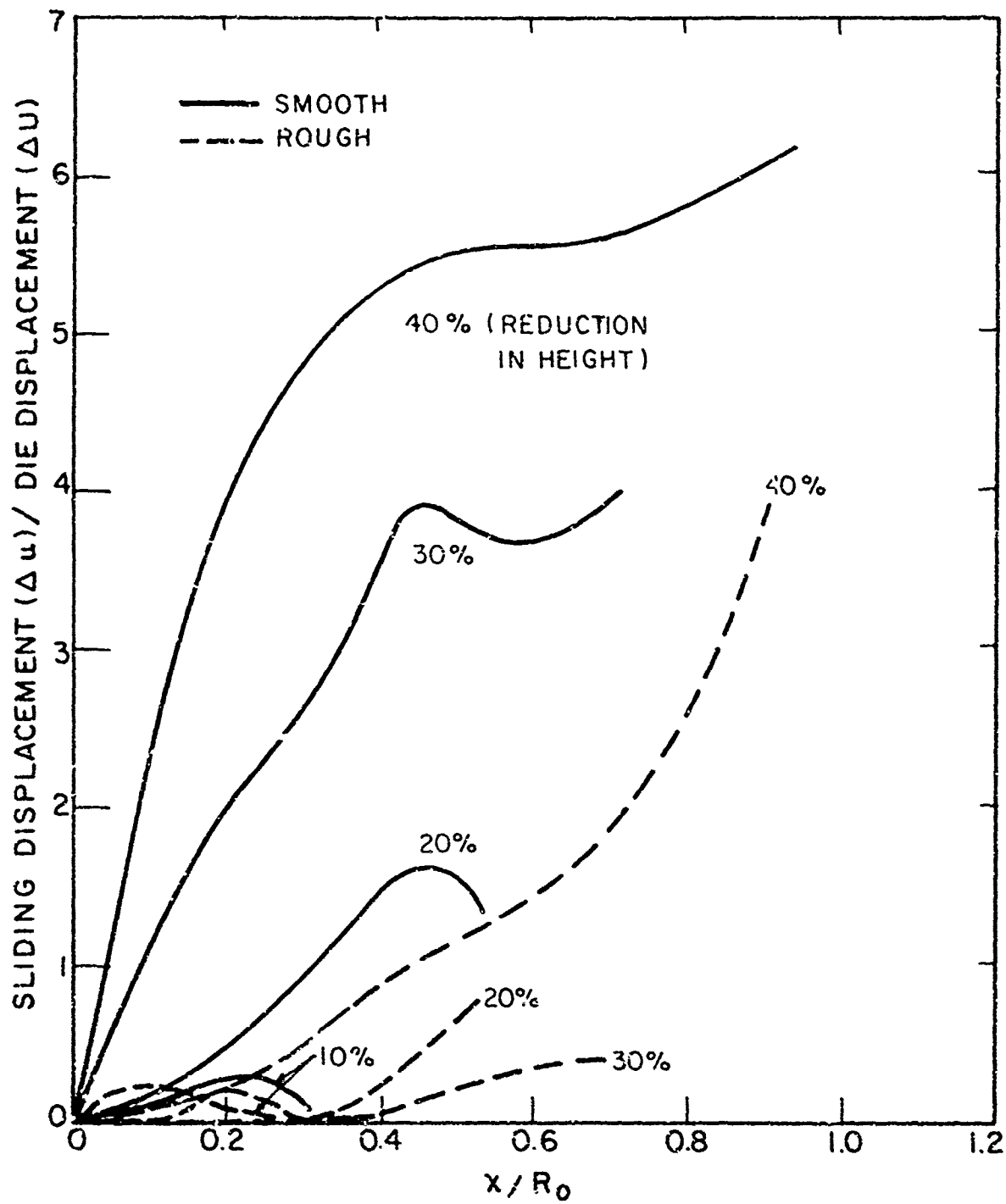


Fig. 7 Sliding displacement distributions at the die-workpiece interface for smooth and rough dies.

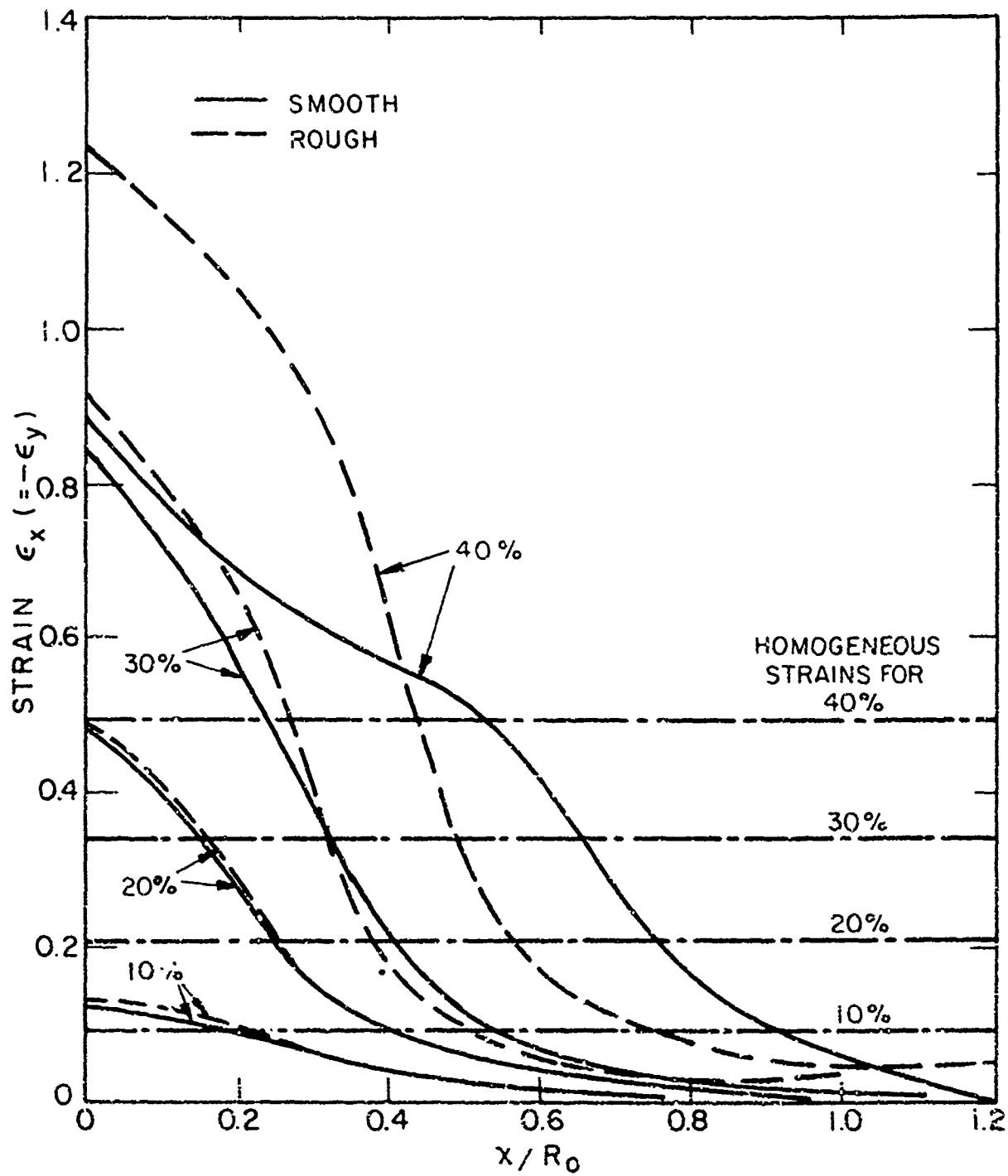


Fig. 8 Strain distributions along the x-axis at various reductions in height: smooth and rough dies.

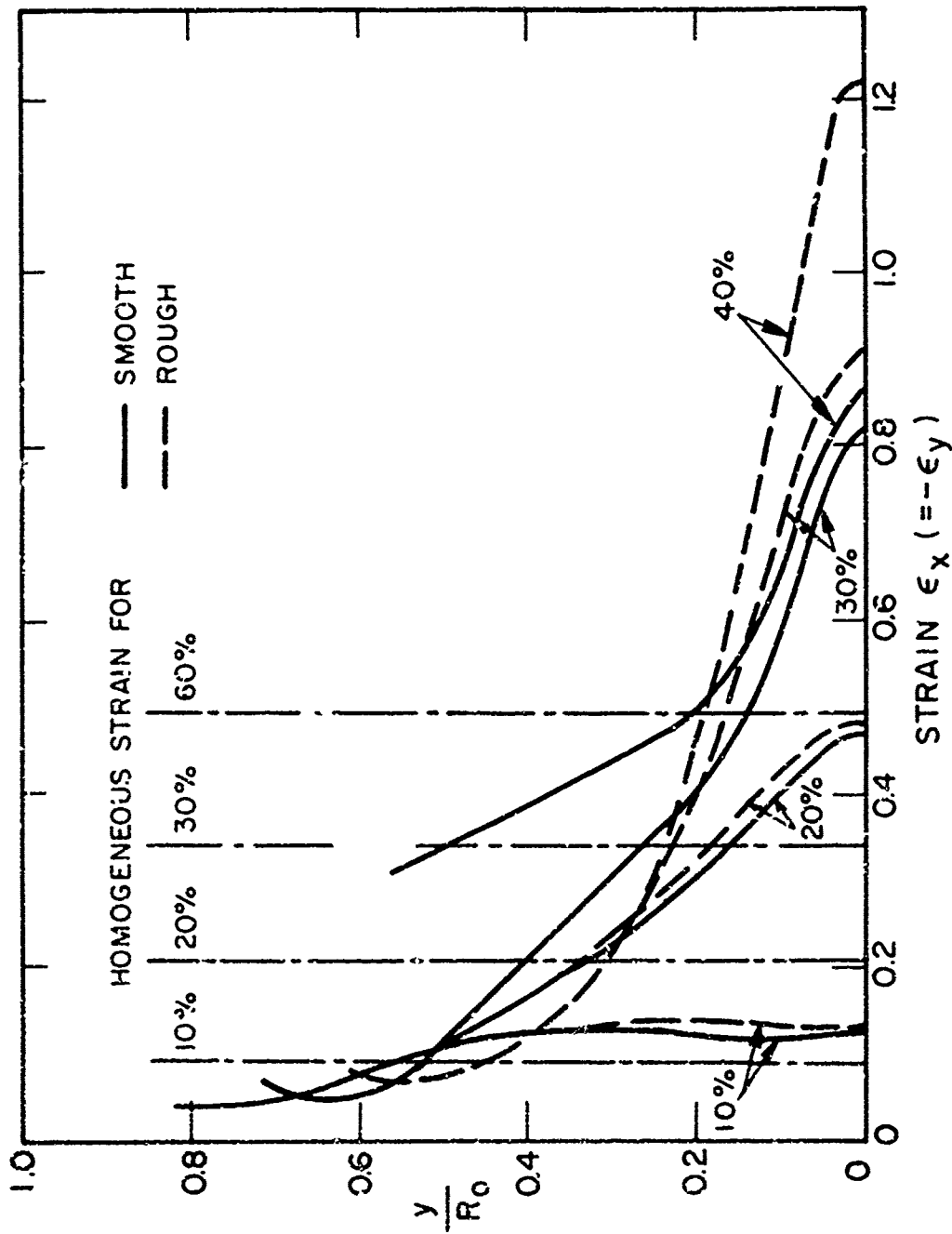


Fig. 9 Strain distributions along the y-axis at various reductions in height: smooth and rough dies.

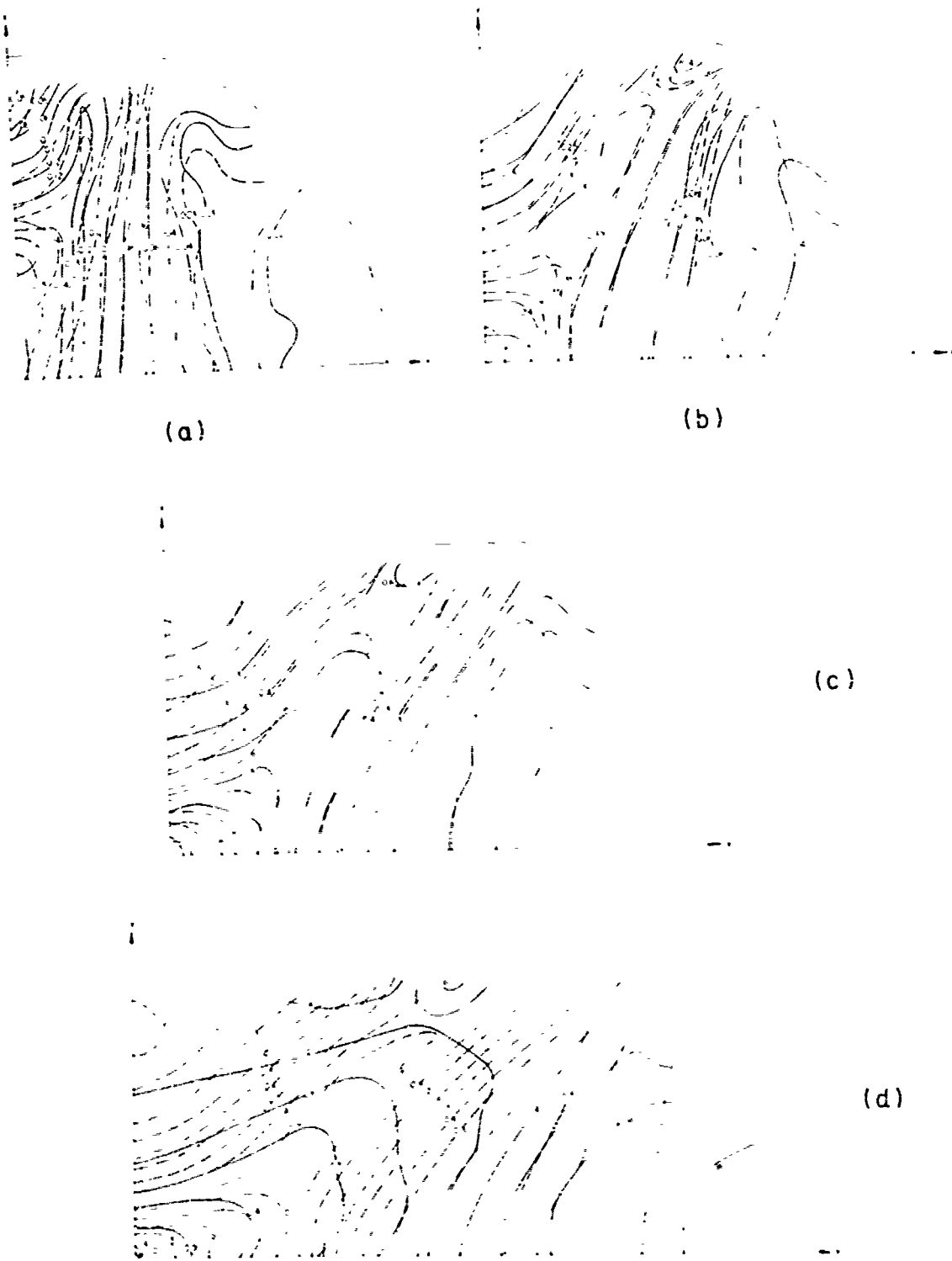


Fig. 10 Constant effective strain contours for smooth (solid curves) and rough (dashed curves) disks at various reductions in height: (a) 10 percent, (b) 20 percent, (c) 30 percent, (d) 40 percent.

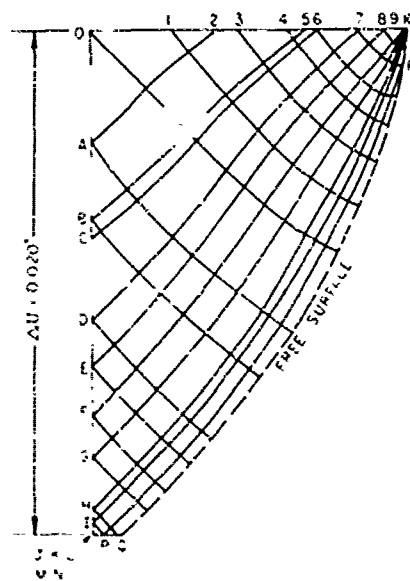
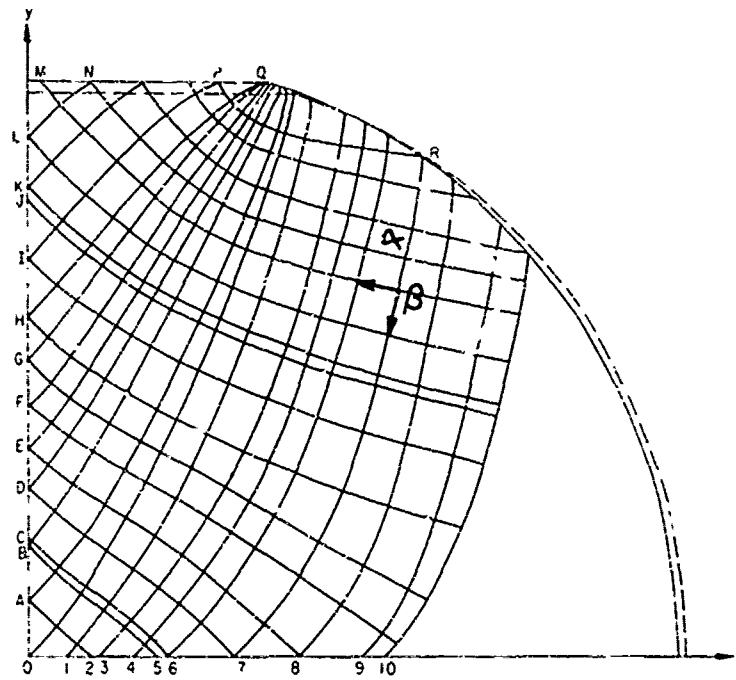


Fig. 11a Slip-line fields and corresponding hodographs for smooth dies at various reductions in height: 10 percent.

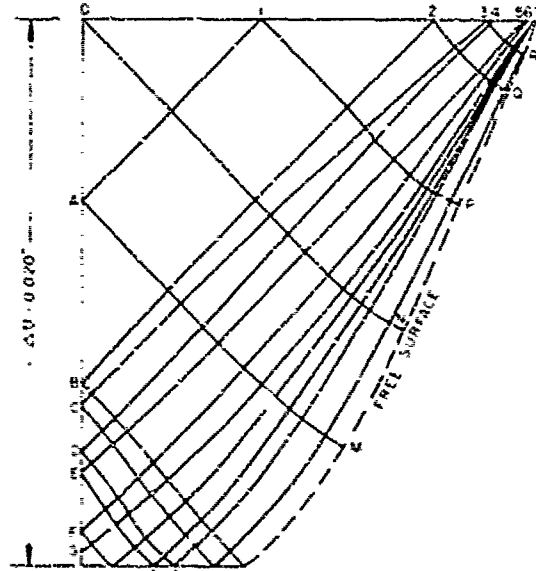
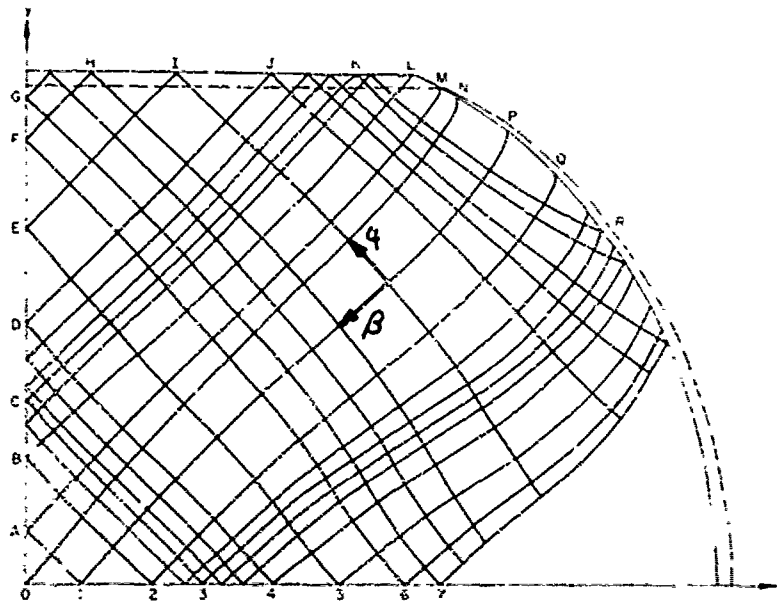


Fig. 11b Slip-line fields and corresponding hodographs for smooth dies at various reductions in height: 20 percent.

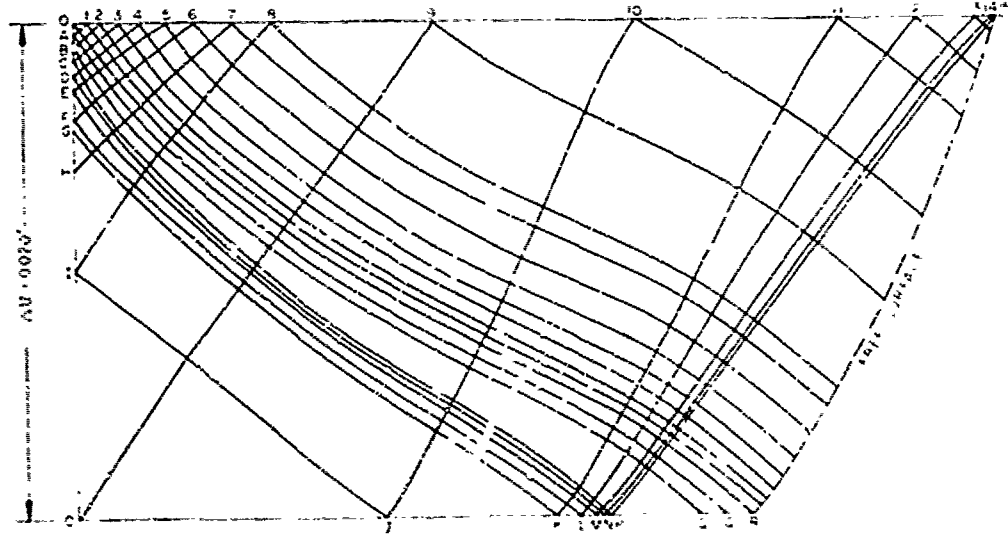
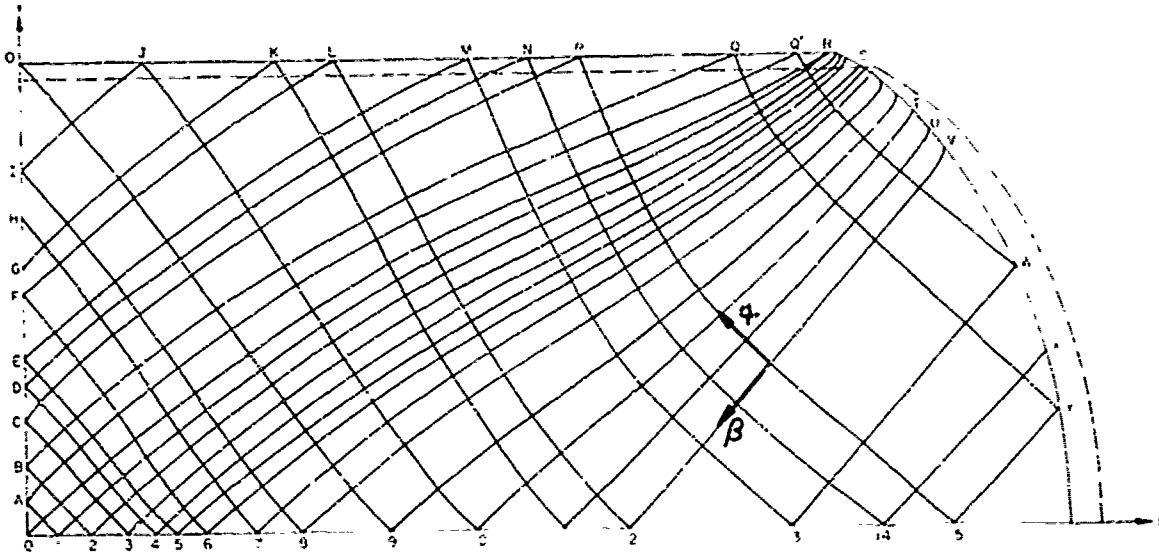


Fig. 11d Slip-line fields and corresponding hodographs for smooth dies at various reductions in height: 40 percent.

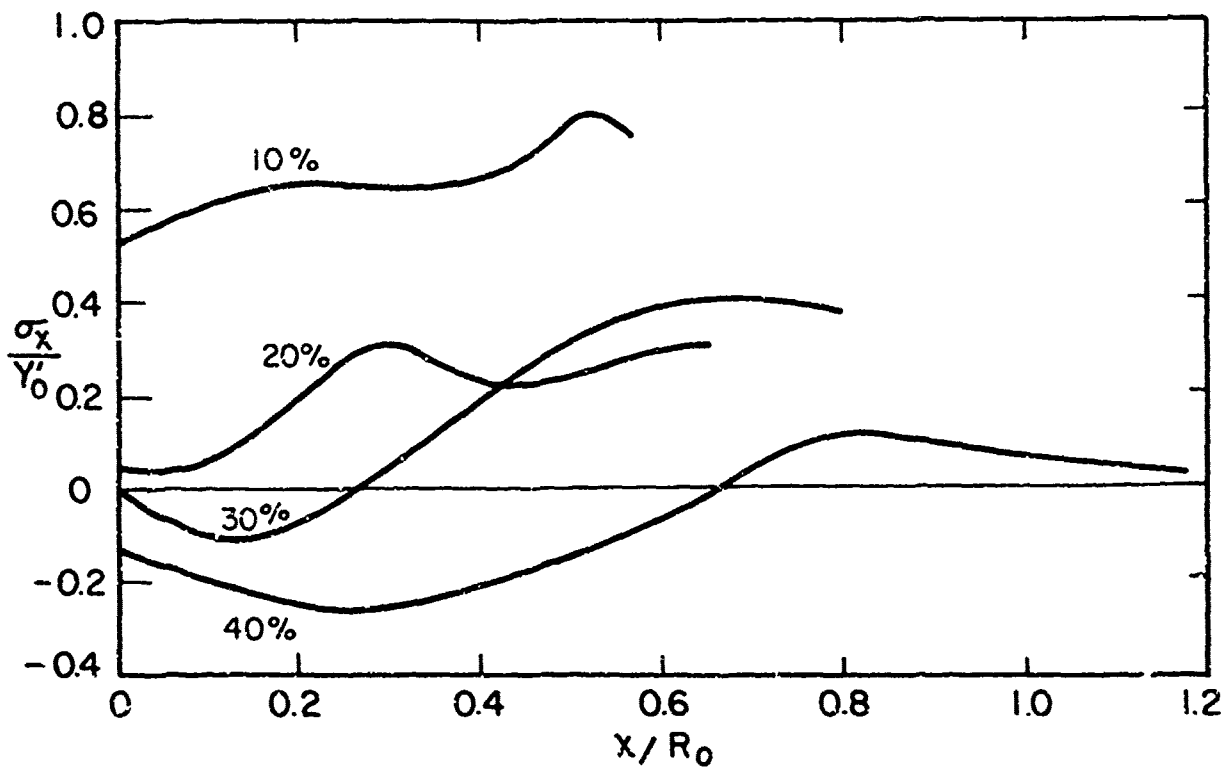


Fig. 12 Distributions of stress σ_x along the x-axis at various reductions in height.

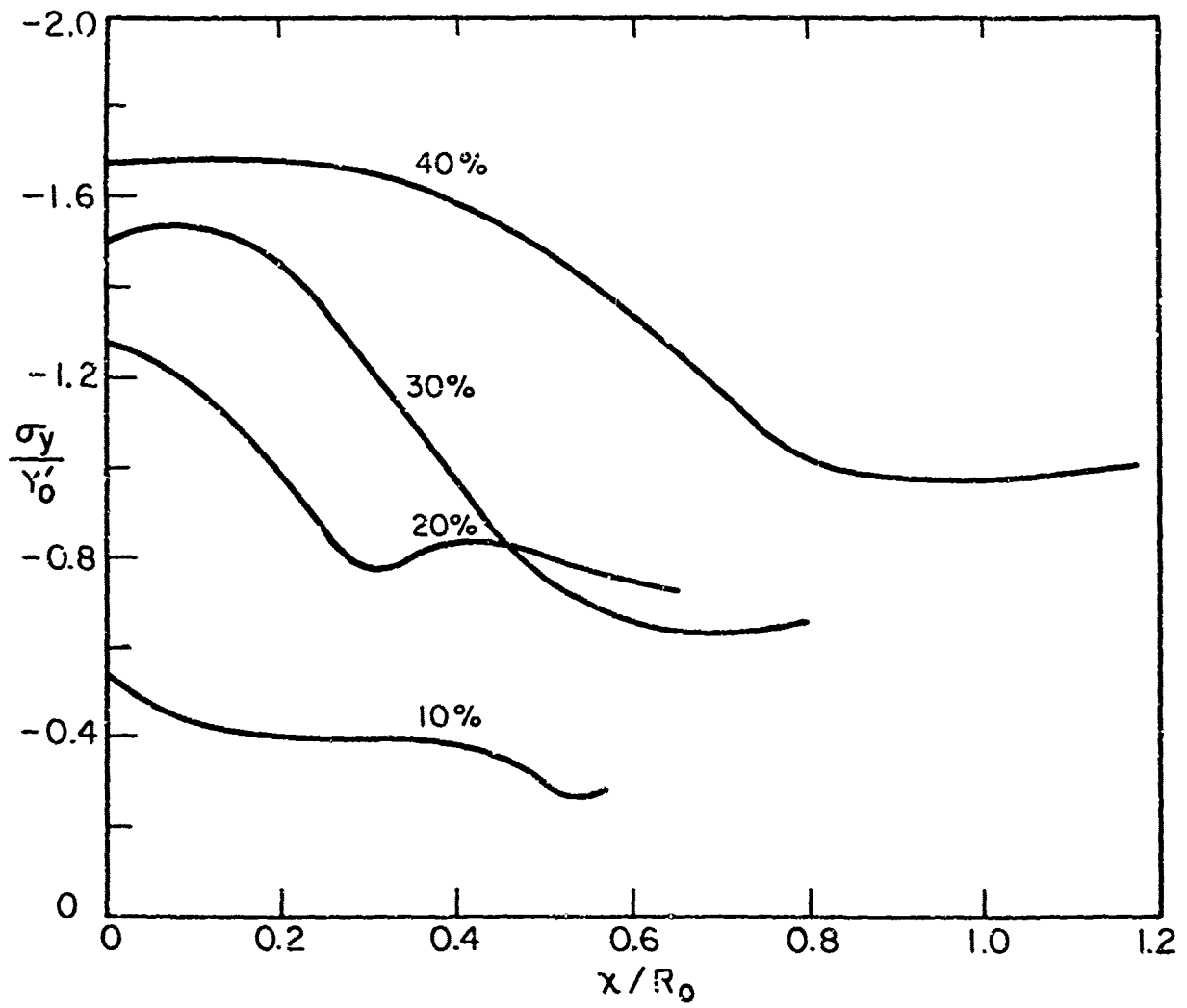


Fig. 13 Distributions of stress σ_y along the x-axis at various reductions in height.

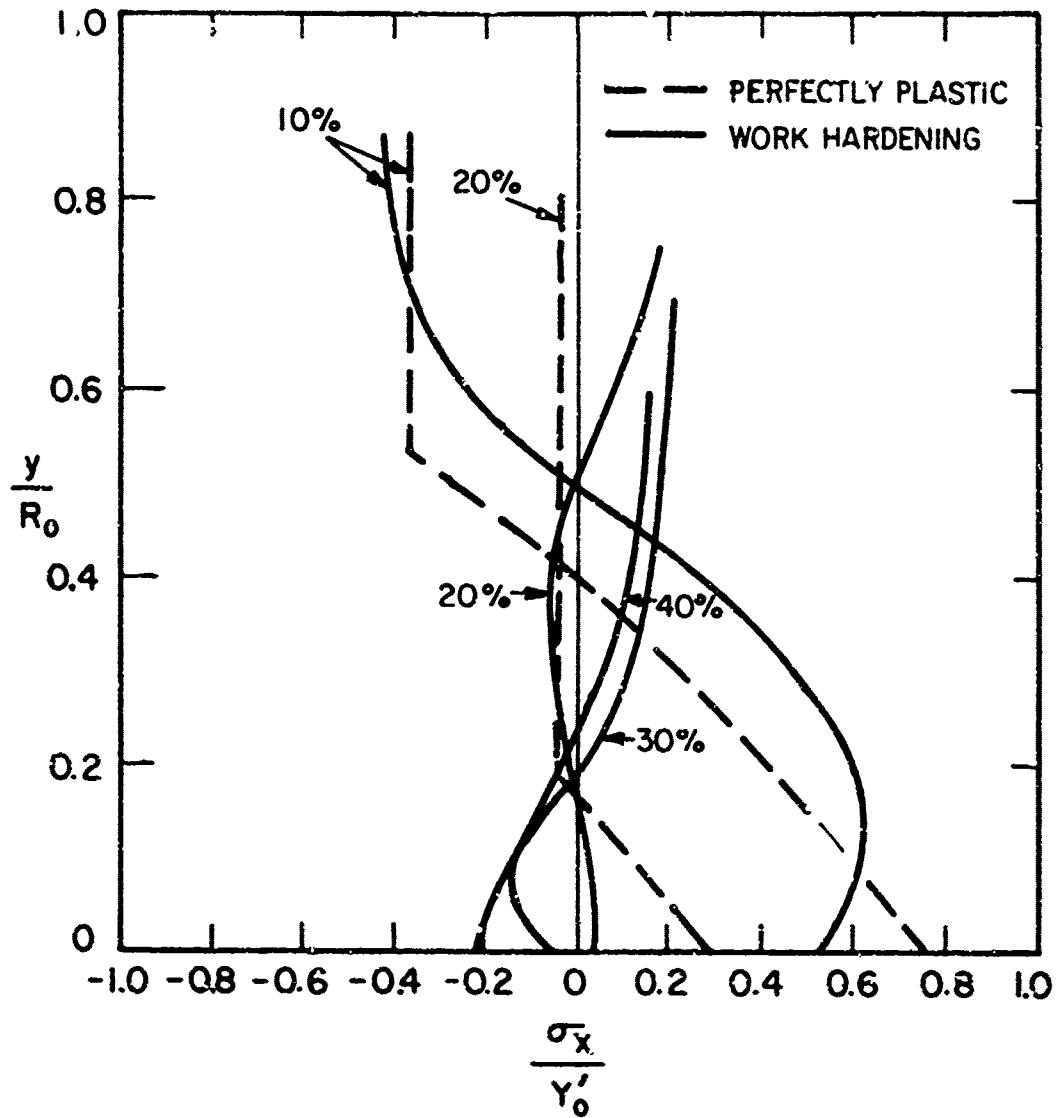


Fig. 14 Distributions of stress σ_x along the y-axis and a comparison with those for rigid, perfectly plastic materials at various reductions in height.

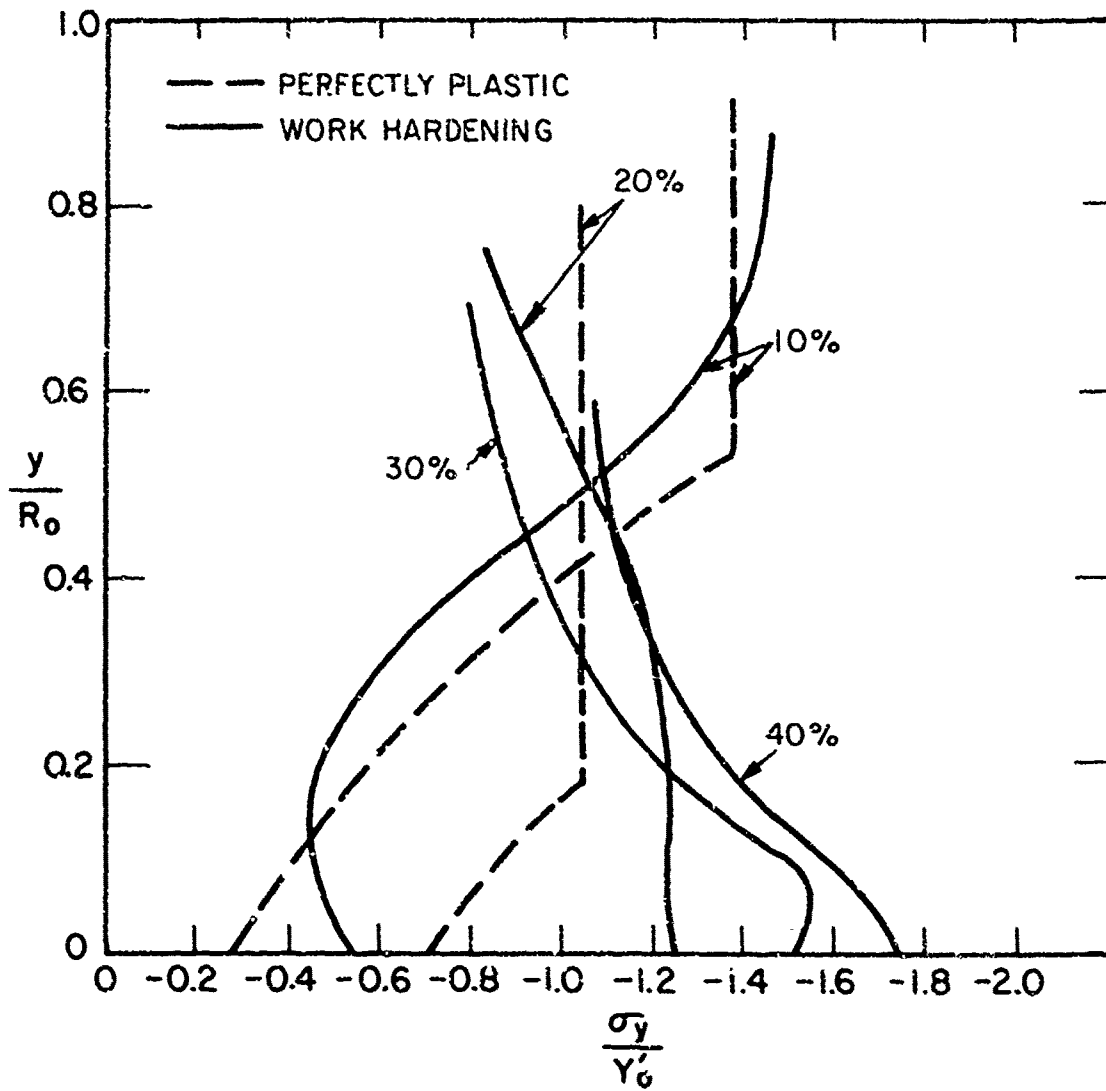
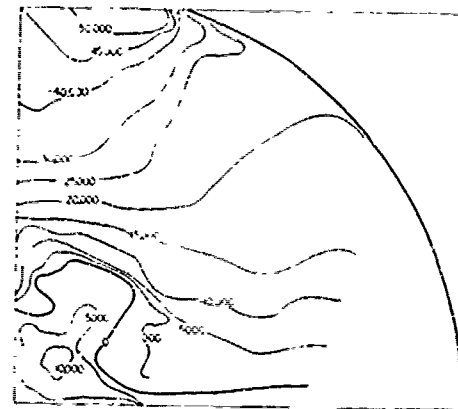
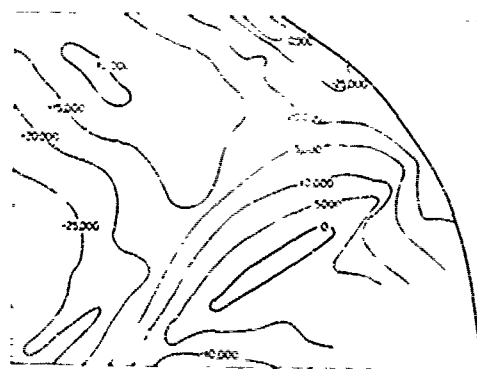


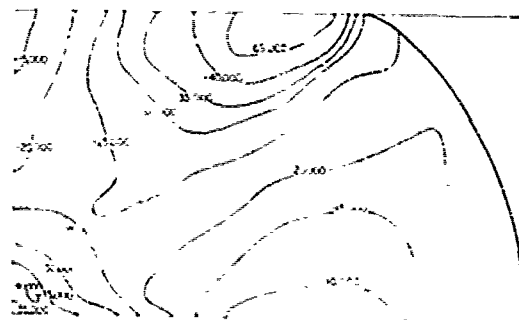
Fig. 15 Distributions of stress σ_y along the y-axis and a comparison with those for rigid, perfectly plastic materials at various reductions in height.



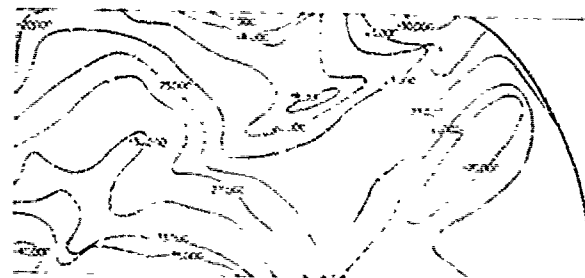
REDUCTION
IN
HEIGHT
10%



20%



30%



40%

Fig. 16 Constant stress σ_z contours at various reductions in height (unit: psi).

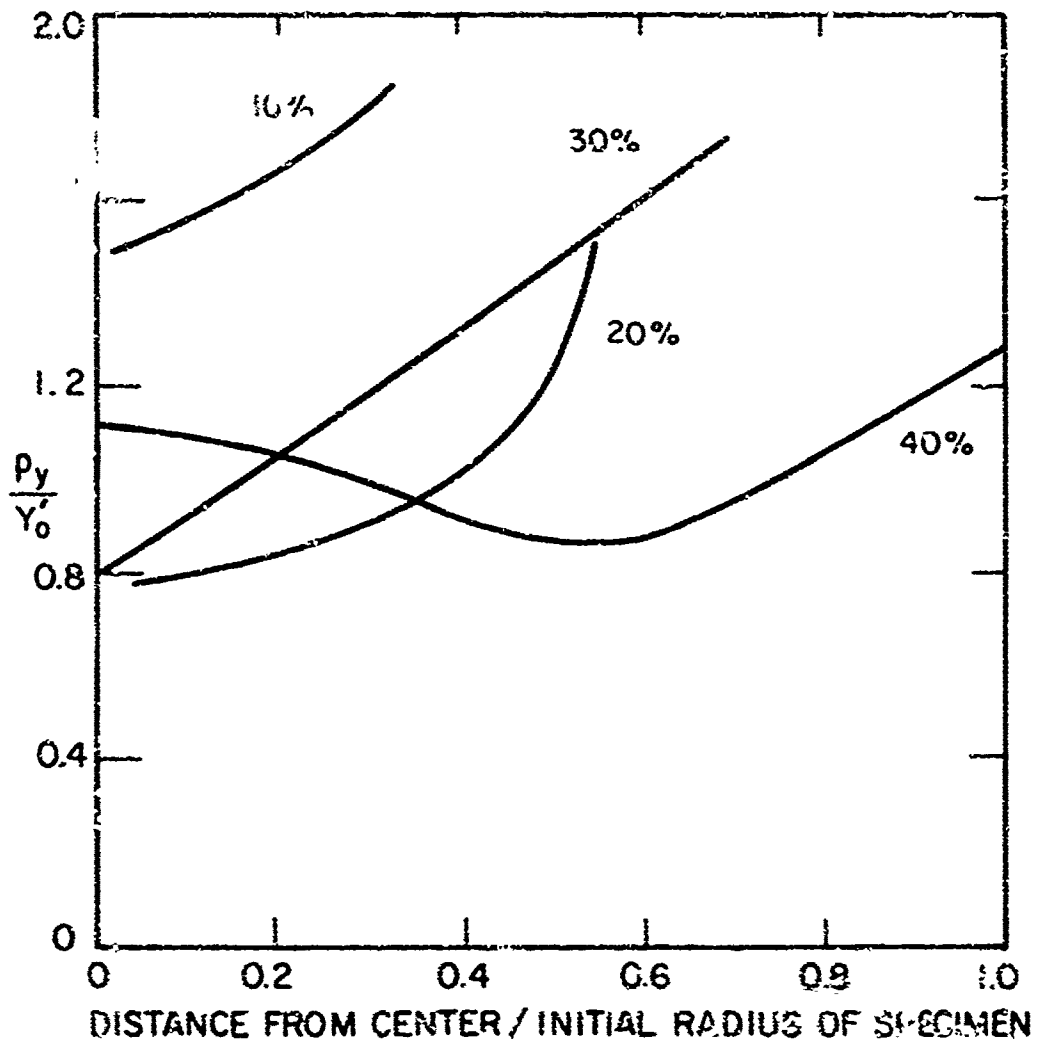


Fig. 17 Contact pressure distributions along the die-workpiece interface.

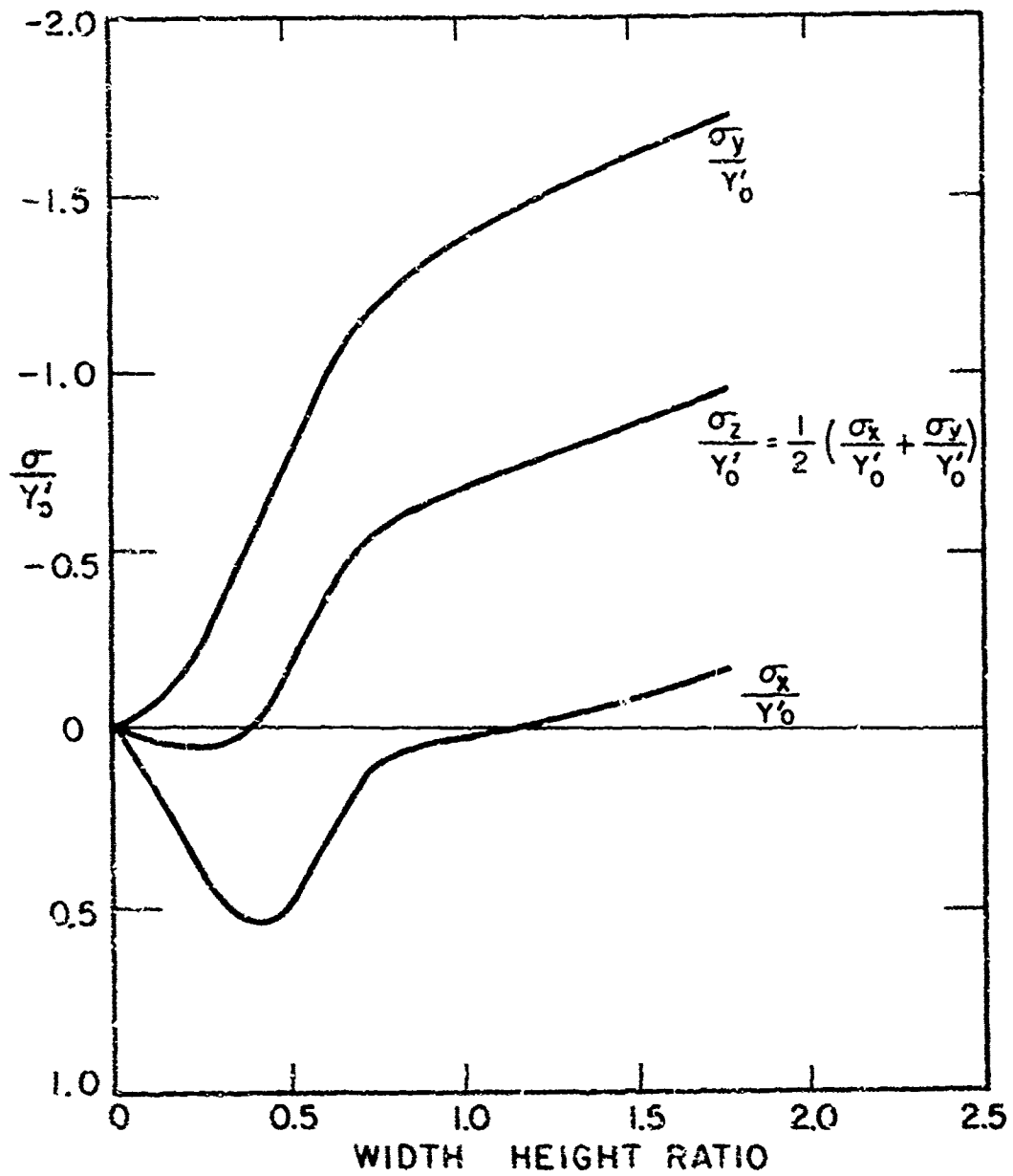
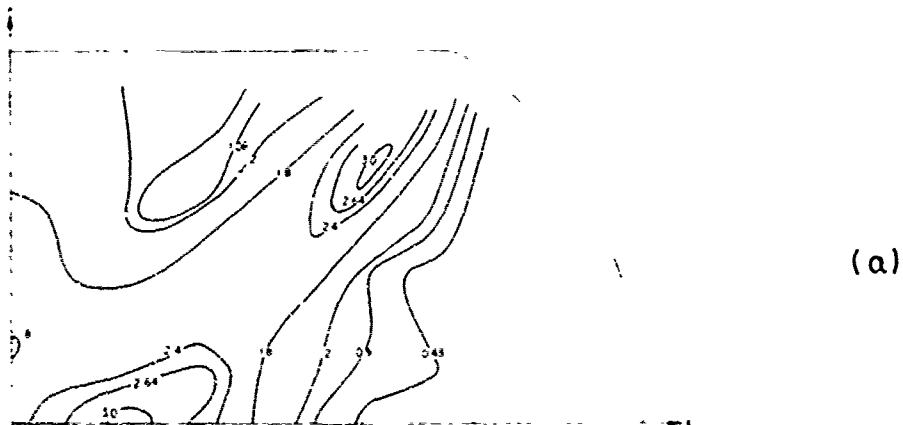
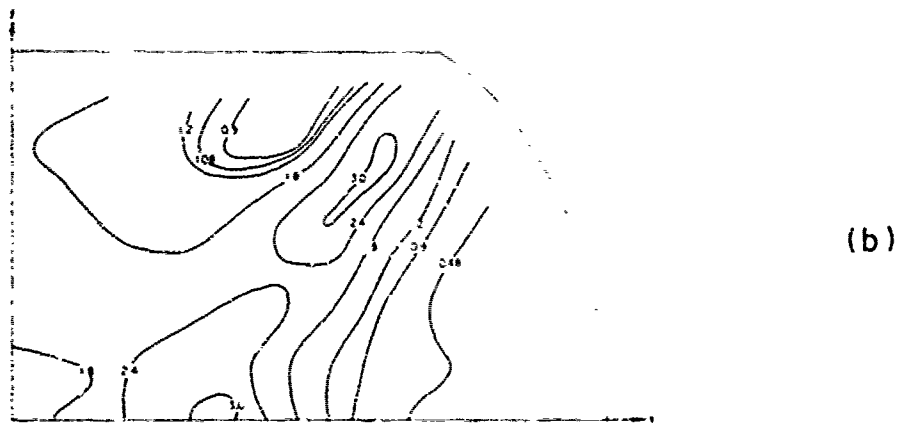


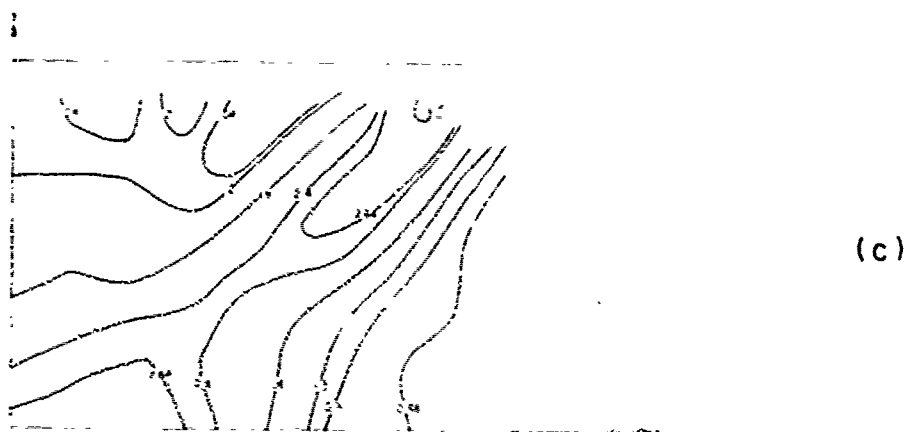
Fig. 28 Variations of stress components at the center of the specimen, as functions of the width-height ratio.



(a)



(b)



(c)

Fig. 19 Constant strain-rate contours at the width-height ratio $w/h = 1.22$ for specimens of various initial f 's.
 (a) $2w_0 = 0.125$ in. ($2\bar{w} = 0.852$ in.), (b) $2w_0 = 0.692$ in.
 ($2\bar{w} = 0.828$ in.), (c) $2w_0 = 0.722$ in. ($2\bar{w} = 0.788$ in.).

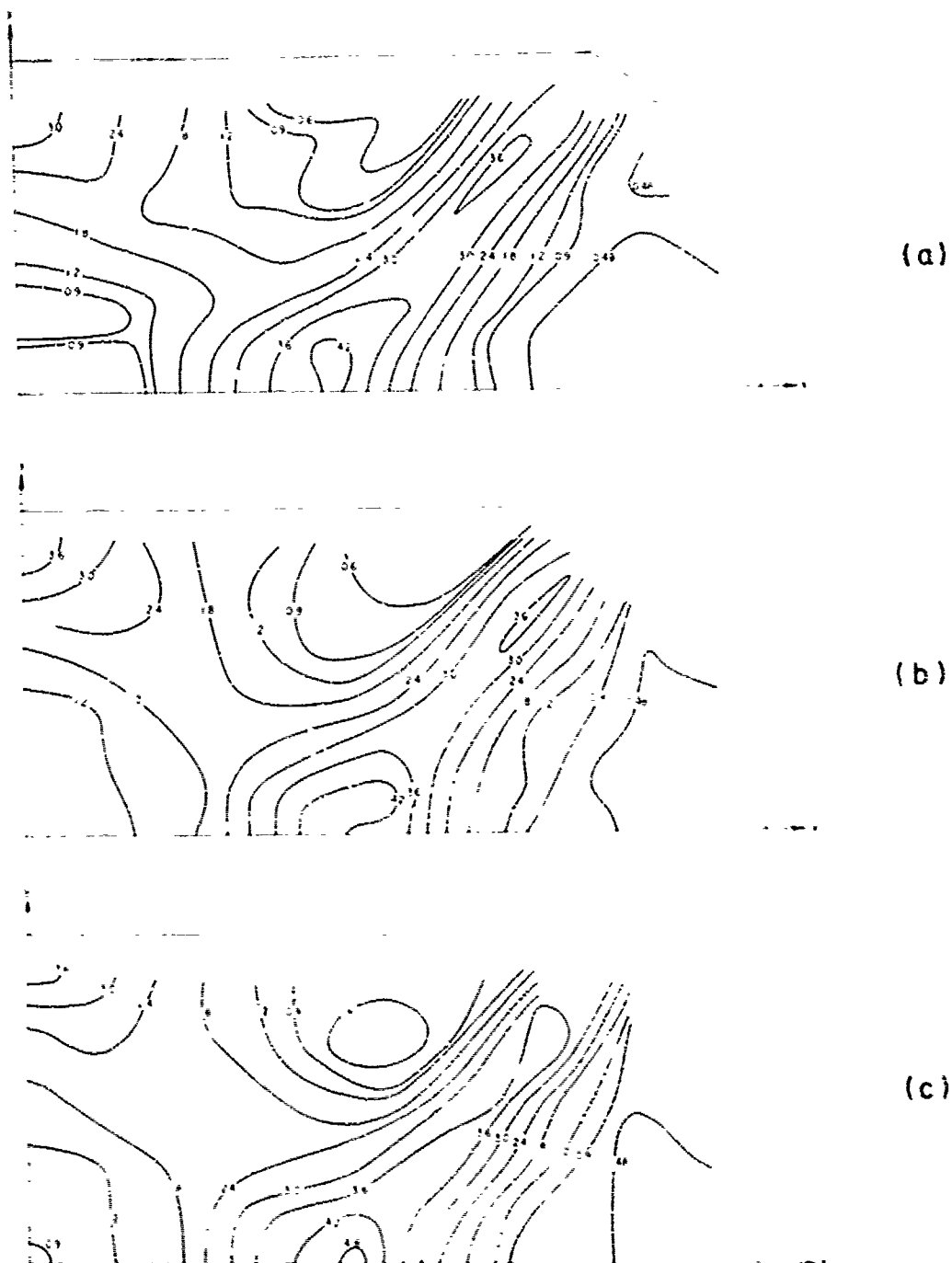


Fig. 20 Constant strain-rate contours at the width-height ratio $w/h = 1.80$ for specimens of various initial flats.
 (a) $2w_0 = 0.125$ in. ($2W = 1.070$ in.), (b) $2w_0 = 0.692$ in. ($2W = 1.039$ in.), (c) $2w_0 = 0.722$ in. ($2W = 1.000$ in.).

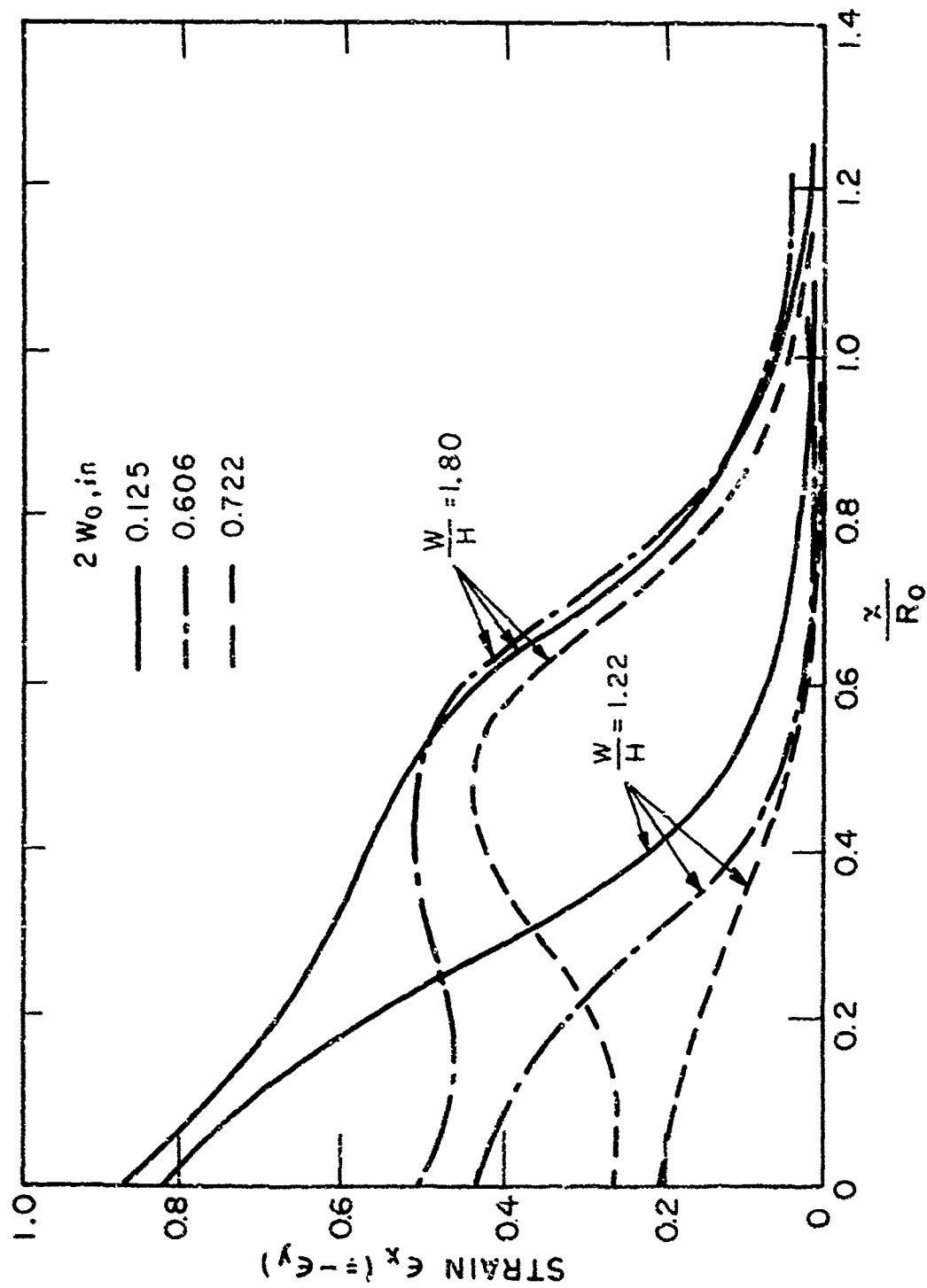


Fig. 21 Strain distributions along the x-axis at the same height-width ratios for three specimens of various initial flats.

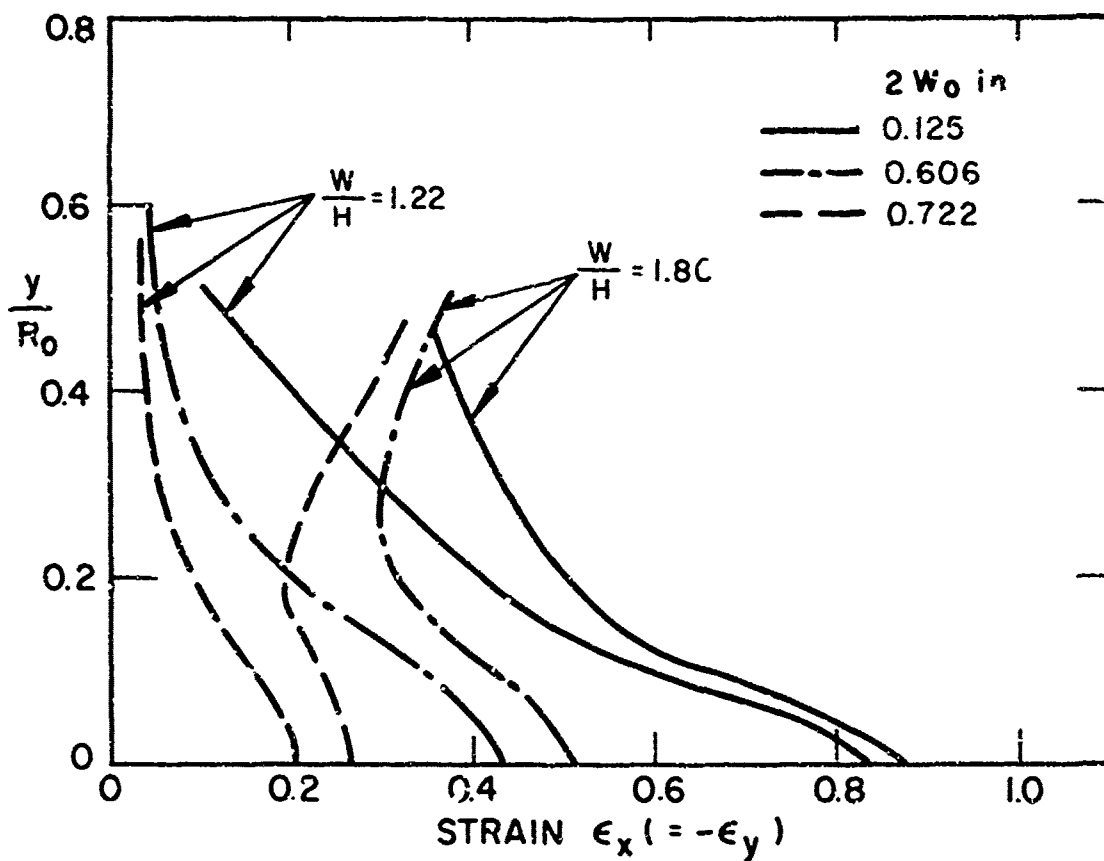


Fig. 22 Strain distributions along the y-axis at the same height-width ratios for three specimens of various initial flats.

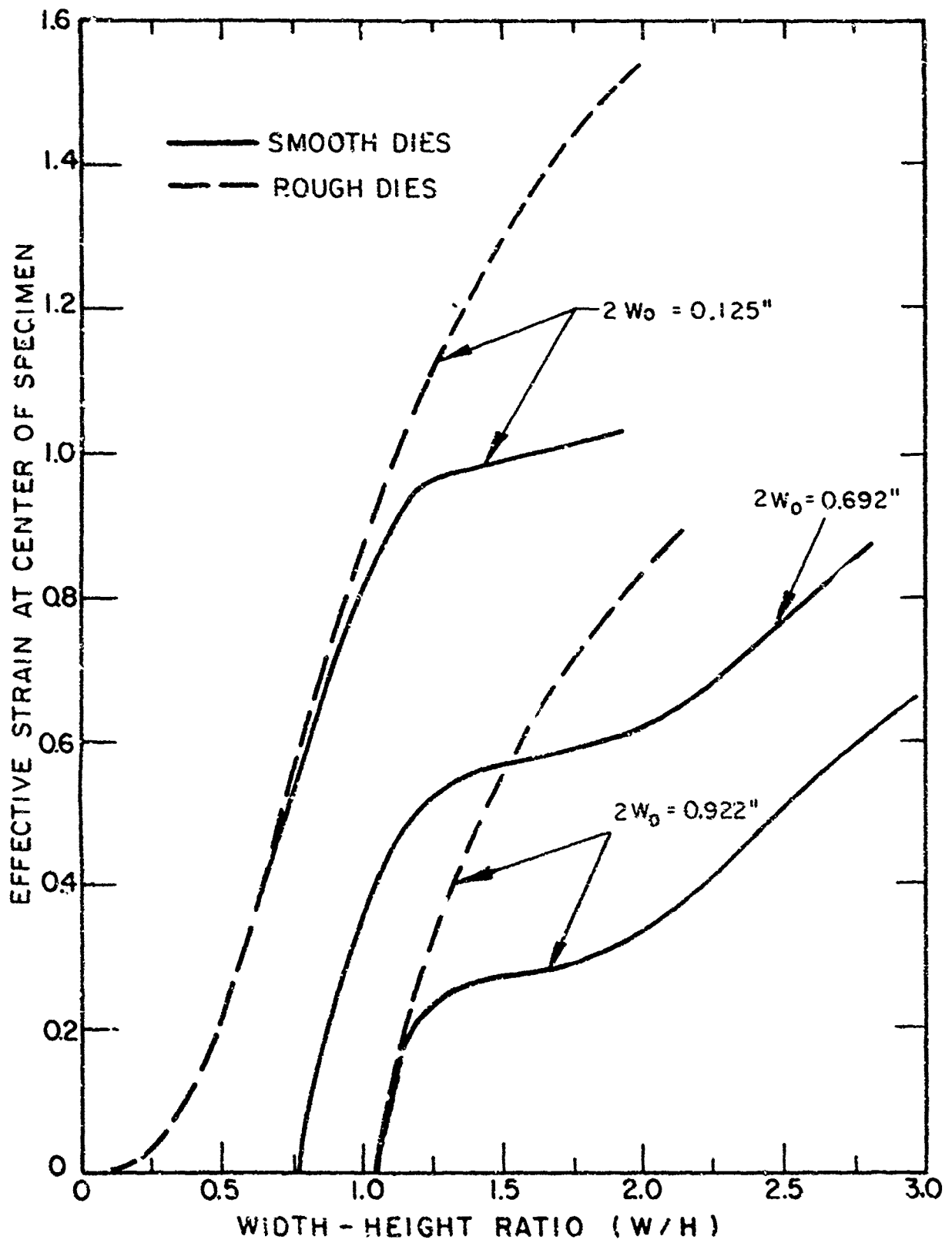


Fig. 23 Effective strain variations at the center of the specimens.

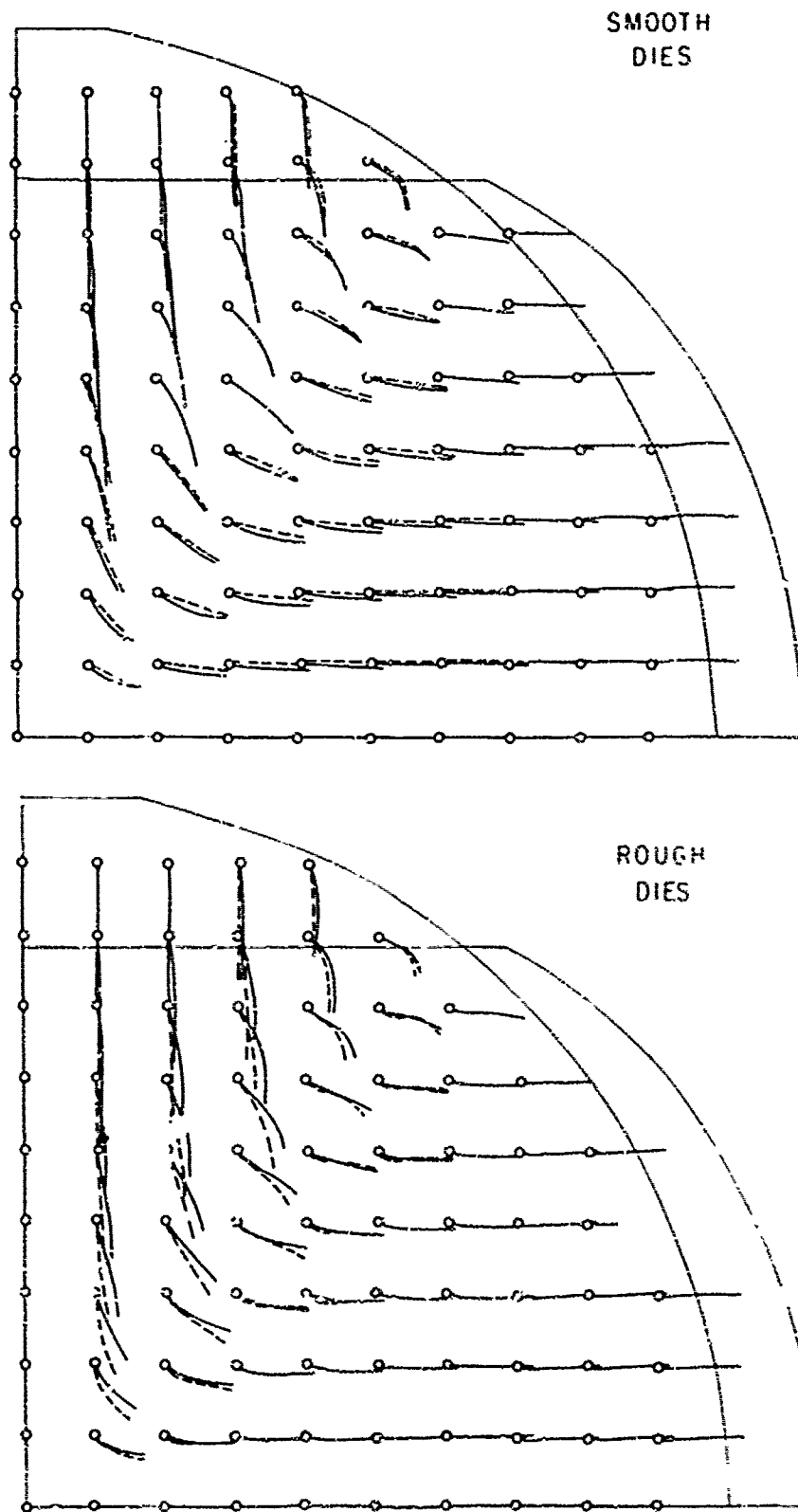


Fig. 24 Comparison of flow lines for aluminum and copper with smooth and rough dies (solid lines, copper; dashed lines, aluminum).

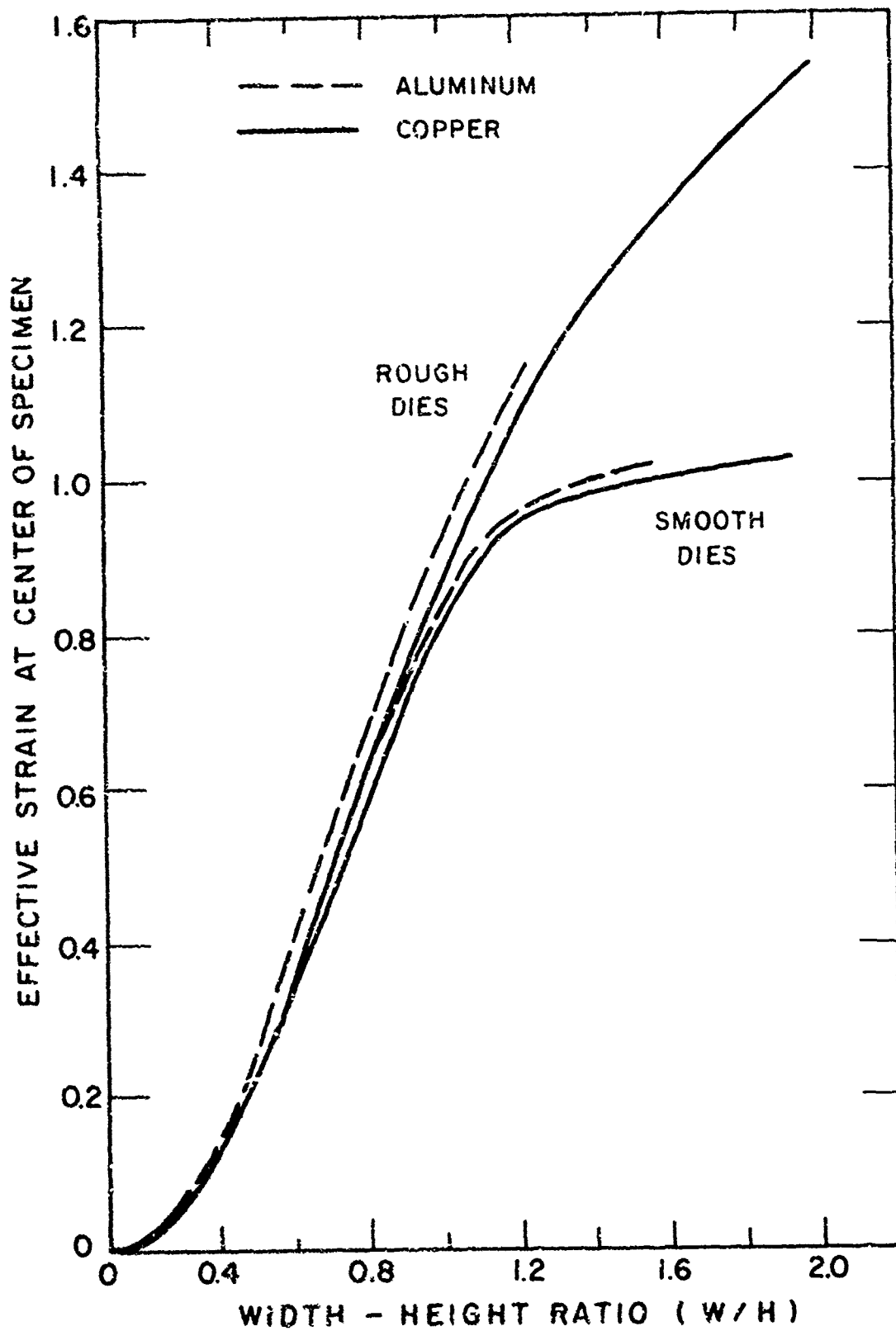


Fig. 25 Effective strain variations at the center of the specimens of aluminum and copper ($2W_0 = 0.125$ in.).